Applications of Metamaterials in Far-field Microwave Wireless Power Transfer at 2.45 GHz

A Thesis

Submitted in Partial Fulfilment of the Requirements
for Award of the Degree of

Doctor of Philosophy

By

Shashank Satish Kulkarni

School of Energy Science & Engineering
Indian Institute of Technology Guwahati
Guwahati, Assam - 781039, India
May 2024

Abstract

Wireless power transfer (WPT) is a technology that enables the transmission of electrical energy from a power source to a receiver without wired electrical connections. This technology has gained significant attention recently due to its potential applications in various industries, including consumer electronics, healthcare, transportation, and aerospace. There are several techniques for wireless power transfer, including inductive coupling, magnetic resonance, laser power, and far-field microwave technologies. Each method has advantages and limitations regarding efficiency, range, and power transfer capacity. The technology can potentially revolutionise how we charge electronic devices, mobile ground and aerial vehicles, power medical implants, and transport energy over long distances. However, there are still challenges associated with the technology, including safety concerns, regulatory issues, and standardisation, which must be addressed to realise the full potential of WPT.

Metamaterials (MMs) are engineered materials with unique properties that can manipulate electromagnetic waves, making it possible to transmit power without wires over long distances. MMs have found various applications in the lens, partial or complete reflectors, transmitters, and absorption media. Far-field microwave WPT using metamaterials is a promising technology that can revolutionise power-beaming methods. In this technology, microwave signals are transmitted from a power source to a receiver through a metamaterial lens, which focuses the energy onto the receiver, enabling efficient and long-distance power transfer. On the receiver side, MM reflector arrays can opt for lightweight mobile vehicle powering scenarios, e.g., robots, aerostats, drones, IoT devices, and sensors in the far field.

This thesis describes applications of MMs in far-field microwave WPT at 2.45 GHz operating frequency. For better comprehension, a WPT system employing microwave frequency is described in detail, along with its components. A literature survey on WPT types, microwave WPT, and its efficiency improvement using MM is studied.

A design, development, and experiment of MM based gradient refractive index (GRIN) lens is carried out. With the inclusion of proposed GRIN lens at an optimum distance from the transmitting antenna, the system efficiency is improved at 1 meter receiver distance. This creates a baseline study of utilising MMs to boost the output at the receiving side. For rover charging application, MM GRIN lens at the transmitting side and MM reflector at the receiving side is adopted. An MM lens concentrates the beam more precisely from the transmitting side, boosting antenna gain and narrowing half-power beam widths. On the receiving side, a planar MM reflector concentrates the incoming beam at its focus, thus improving the reception. The electric field with MM lens at Tx and MM reflector at Rx is enhanced by a factor of two compared to a typical system without MM.

The power in the sidelobes can be adjusted by tuning the focus of the arrangement. Therefore, to power multiple receivers simultaneously, a novel dual-reflector antenna based on a planar metasurface sub-reflector (MSSR) is designed, fabricated, and tested. The main lobe and sidelobe power distribution of the proposed antenna can be changed by adjusting the MSSR position from focus. The proposed antenna with the sidelobes is a suitable choice for simultaneous powering multiple receivers spaced at different angles.

The planar MSSR array is compact and lightweight and hence can be opted for mobile receivers with patch antenna as feed. An innovative machine-learning (ML) technique using random forest regression (RFR) to predict radiation properties in a planar metasurface reflector (PMSR) antenna at 2.45 GHz is studied. The RFR model is trained using power distribution at the near-field, far-field boundary, and in the far-field region. An good agreement between actual and predicted values is observed when compared with the experiment results. This RFR-ML approach is beneficial for assessing antenna radiation properties by elevating and training the dataset for different reflector-feed configuration in the future work.

Dedication

To,

Everyone

who made this journey

happy!

Certificate

This is to certify that the thesis entitled "**Applications of Metamaterials in Far-field Microwave Wireless Power Transfer at 2.45 GHz**", submitted by **Shashank Satish Kulkarni**, a research scholar in the *School of Energy Science and Engineering, Indian Institute of Technology Guwahati*, for the award of the degree of **Doctor of Philosophy**, is a record of an original research work carried out by him under my supervision and guidance. The thesis has fulfilled all requirements per the institute's regulations and reached the submission standard. The results embodied in this thesis have not been submitted to any other University or Institute for the award of any degree or diploma.

Date:

Place:

Prof. Sisir Kumar Nayak
Professor
Dept. of Electronics and Electrical Engg.
Indian Institute of Technology Guwahati
Guwahati, Assam - 781039, India.

Acknowledgements

I am filled with an overwhelming sense of gratitude for the path I've traversed. Each step, every twist and turn, has been enriched by the presence of remarkable individuals who have graced my journey. Their kindness, wisdom, and unwavering support have illuminated the way and filled my heart with profound appreciation. To everyone who has walked along my path, I want to extend my deepest thanks, for your presence has been a cherished gift that has made this journey truly enchanting. The names are many and are not limited to,

Aai
Baba
Niraja
Prof. Sisir Kumar Nayak
Prof. Vinayak N. Kulkarni
Prof. Harshal B. Nemade
Mukund
Abhishek Paikray
Dr. Niharika
D. Senthil Kumar
Vivek Kumar
Deepak Kanumuri
Amarnath
Chayanika
Ambuj
Subhendu
Satyajeet
Dr. Budhadeb Maity
Anurag
Himansu Sahoo
Deepak Sahoo
Abhishek Singh
Rupam Bhaduri
Aquib Jawed
Pushpita
Angshuman
Rishiraj
Dr. Soumya Nanda
Dr. Siddhesh Desai
Dr. Saibal Kanchan Barik
Dr. Anil Rout
Anand Verma
Abhishek Kamal
Dr. Abhijeet Mazumdar
Dr. Aniruddha Mazumdar
Nayanjyoti
Naresh Kaka
Nana Kaka
Krishna Kulkarni
Pravin Sanghai
Rajat Sanghai
Ashish Kulkarni
...
...
...

Contents

2 Feasibility study of far-field WPT using GRIN MM 19

3 Enhancement of electric field in far-field rover charging application using MM GRIN lens and reflector 41

List of Figures

List of Tables


भारतीय प्रौद्योगिकी संस्थान गुवाहाटी
Indian Institute of Technology Guwahati

List of Acronyms

2D	Two-dimensional
3D	Three-dimensional
AC	Alternating Current
CST	Computer Simulation Technology
DC	Direct Current
DRGH	Double-Ridged Guided Horn
EM	Electromagnetic
EMF	Electromotive Force
GRIN	Gradient Refractive Index
HPBW	Half Power Beamwidth
IPT	Inductive Power Transfer
ML	Machine Learning
MM	Metamaterial
MS	Metasurface
MSSR	Metasurface Sub-Reflector
PC	Phase Centre
PCB	Printed Circuit Board
PMSR	Planar Metasurface Reflector
PT	Power Transfer
RF	Radio Frequency
RFR	Random Forest Regression
Rx	Receiver/Receiving

SLL	Sidelobe Level
SWIPT	Simultaneous Wireless Information and Power Transfer
Tx	Transmitter/Transmitting
UAV	Unmanned Aerial Vehicle
VSWR	Voltage Standing Wave Ratio
WEH	Wireless Energy Harvesting
WPT	Wireless Power Transfer

List of Symbols

D	maximum dimension of antenna (in meters)
$\mathbf{E}$	time-varying electric field (V/m)
F	focus of GRIN lens
$\mathbf{H}$	time-varying magnetic field (A/m)
R	distance (in meters)
S_{11}	input port voltage reflection coefficient
S_{21}	forward voltage gain
c	velocity of EM wave in free space ($= 3 \times 10^8$ m/s)
f	focus of MM reflector and MS reflector antenna
f_0	operating frequency (in Hz)
n	refractive index of medium ($\sqrt{\mu\varepsilon}$)
n_0	refractive index of free space ($= 1$)
ε	permittivity of medium ($= \varepsilon_0\varepsilon_r$)
ε_0	permittivity of free space ($10^{-9}/36\pi$ F/m)
μ	permeability of medium ($= \mu_0\mu_r$)
μ_0	permeability of free space ($4\pi \times 10^{-7}$ H/m)
λ	wavelength (in meters)
λ_0	operating wavelength (in meters)

Chapter 1

Introduction

Overview

This chapter introduces wireless power transfer (WPT), its types and applications. A system utilising microwave frequency for WPT is described with its constituent elements for a better understanding of the methodology. An antenna is a key element in microwave WPT for transmitting and receiving power or energy. The transmission and reception are carried out by electromagnetic (EM) waves propagating through free space. A relation between transmitted power, received power, separation distance, gains of the antennas and operating frequency is given by Friis transmission equation. A literature survey on WPT and its improvement using metamaterials (MMs) is presented. A motivation for WPT improvement in the microwave regime is described, followed by a list of objectives to be carried out, and the organisation of the thesis.

1.1 Introduction to WPT

Wireless power transfer (WPT) is a technique of powering devices without wired electrical connections. This provides freedom of movement to the receiver and prevents hazardous electrical shocks due to loose connections and short circuits. Based on their source and distance of separation, broadly, there are two types of WPT systems such as radiative and non-radiative, as depicted in Figure 1.1. Non-radiative WPT uses proximity with the receiver (Rx) and is more efficient. Inductive coupling based on spirals or helix of specific inductance and resonant coupling based on tank circuit are two sub-types of non-radiative WPT. Radiative WPT is based on radiation of electromagnetic waves or light of particular frequency and hence can be used for large distance transmissions. Depending upon the application, laser systems use visible light transmitted by a high-power laser diode received by a photodetector or light-activated diode. Since the conversion of light to electricity depends on photodiode rating, this type of WPT is less efficient. Microwave WPT uses high-power electromagnetic waves transmitted through free space towards the receiver side. The power extraction mainly depends on the receiver antenna aperture and matching circuit, which can be designed correctly to achieve maximum efficiency.

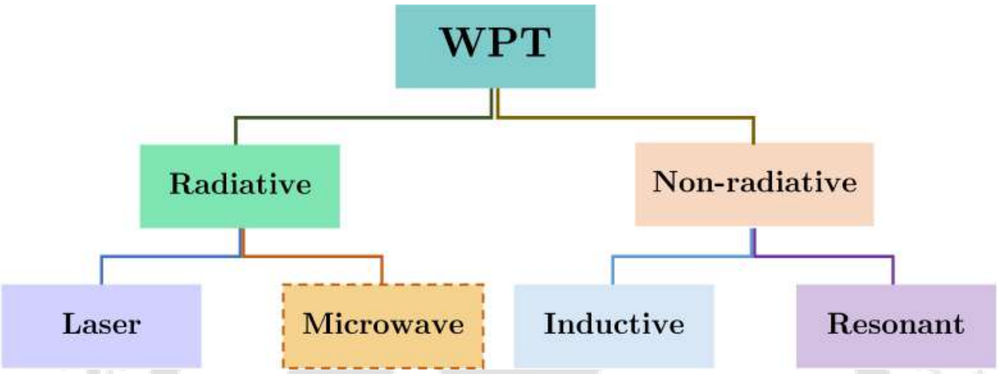

Figure 1.1: Types of WPT.

1.2 Non-radiative WPT

1.2.1 Inductive PT

The inductive PT (IPT) method utilises two inductive coils separated by a distance as depicted in Figure 1.2. The oscillator produces an alternating current (AC) that flows

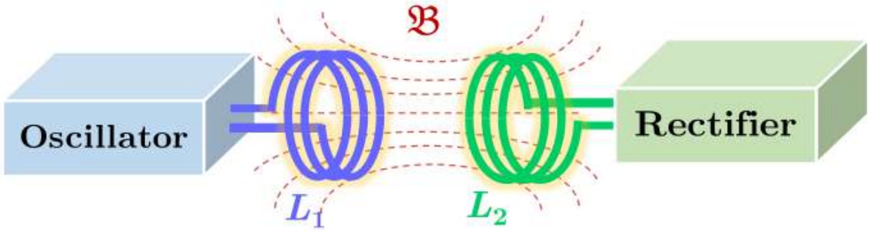

Figure 1.2: Schematic of an inductive WPT system.

through coil L_1, and it establishes magnetic field density $\mathfrak{B}$ in its proximity. When this magnetic field is linked with coil L_2, this magnetic field generates an electromotive force (EMF) at the receiving side by Faraday's law of electromagnetic induction. The induced alternating current can drive the load directly or be rectified to direct current (DC) to power battery-operated devices. Inductive coupling is the oldest and most frequently utilised wireless power transfer method, perhaps the only one used in commercial devices. To avoid the risk of electric shock, IPT is used for charging transport vehicles, cellphones, headphones, mics, etc. and are presented in [1] -[8].

The power transferred increases with mutual inductance M between the coils, which is determined by their geometry and physical distance. The coupling coefficient is a widely used figure of merit and is given as $M = k\sqrt{L_1 L_2}$, where $'k'$ is the coupling coefficient. When the Tx-Rx coils are perfectly aligned on the same axis and near together, all of the magnetic flux from L_1 gets linked with L_2, and $k = 1$ then the transmission efficiency approaches 100%.

1.2.2 Resonant PT

Strongly coupled magnetic resonance or resonant inductive coupling is a sort of inductive coupling wherein resonant tank circuits are used. The Tx coils transfer power by inducing time-varying magnetic field ($\mathfrak{B}$) density at the Rx. Figure 1.3 illustrates a basic resonant PT system, which is based on studies that are presented in [9] -[15]. Each resonant circuit consists of a wire coil coupled to a capacitor, a self-resonant coil, or another resonator with an internal capacitance C. The resonance frequencies for both the resonators are identical. The resonance between the coils can significantly increase the coupling and power transfer. This is similar to a vibrating tuning fork that can produce sympathetic vibration in a distant

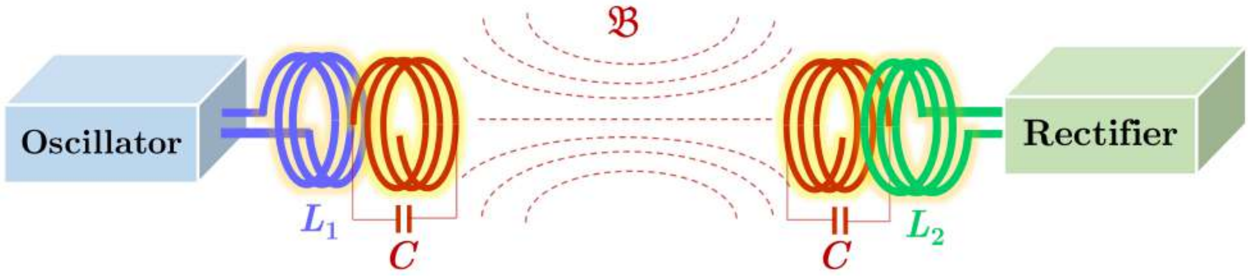

Figure 1.3: Schematic of a resonant WPT system.

division set to the same pitch. Nikola Tesla discovered resonant coupling at the beginning of the 20^{th} century in his WPT research. Still, the prospects of exploiting resonant coupling to extend transmission range have only recently been explored.

Resonators with a high quality (Q) factor are anticipated to transmit energy considerably more efficiently than a typical IPT system. As a result, resonance allows power to be delivered over longer distances with weak magnetic fields. In contrast to "short-range" non-resonant inductive transfer, which can only achieve similar efficiency when the coils are close together, this is referred to as "mid-range" transfer. Since the resonant circuits interact with one another more strongly than non-resonant WPT, power losses due to absorption in neighbouring elements are minimal.

1.3 Radiative WPT

1.3.1 Laser PT

Power can be conveyed by converting energy into a laser beam that is received and focused onto photovoltaic cells. The radiation in this technique is closer to the visible portion of the spectrum (0.2 to 2 micrometres). Since the power is beamed to a receiver that can convert it to electrical energy, this method is known as 'power beaming'. Figure 1.4 shows the basic building blocks of a laser PT system. The power supply unit provides a regulated output that drives the laser assembly. A high-power laser diode emits light in a small volume and travels towards a photodiode or photovoltaic receiver. The receiver diodes in laser power converters are optimised for line-of-sight incident light conversion.

Laser PT offers several advantages over other wireless approaches. A collimated monochromatic wavefront propagation enables a small beam cross-section region and long-distance

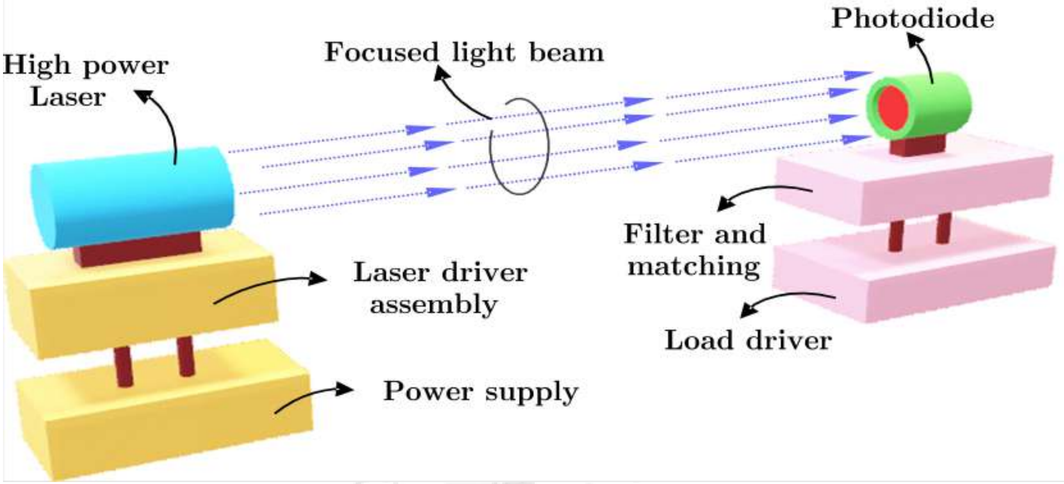

Figure 1.4: Schematic of a laser WPT system.

transmission. As a result, when the distance between the transmitter and the receiver is increased, there is minimal power loss. The solid-state lasers are tiny enough to fit into small goods. This system will not produce radio-frequency interference with radio communication like WiFi or cell phones. Also, only receivers that are struck by the laser will be powered.

However, there are several drawbacks faced during system design. The use of lasers may be dangerous. Low to medium power levels could lead to hazardous situations if an appropriate safety system is not in place. Through localised spot heating, high power levels can be even more penetrating. The amount of electricity that can be converted into light is restricted due to a photodiode's practical power handling capacity and conversion efficiency (or Rx diode). Atmospheric absorption and scattering by clouds, fog, rain, and other factors can increase losses. Also, a direct line of sight to the target is required for power reception.

Furthermore, compared to designing and manufacturing structures for microwave WPT, the size of the systems for improving the light wave WPT is in nm, which is expensive and challenging to produce. In contrast to microwave WPT, line of sight, beam regulating, and splitting are highly challenging in light wave WPT for charging multiple devices simultaneously and dynamically. A lasers PT finds versatile applications in powering robots [16], UAVs [17], and orbiting satellites [18].

According to TABLE II of [19], the highest overall efficiency of light wave WPT is 14%. However, the radio frequency (RF)-DC conversion efficiency can increase to 71 % in the case of microwave WPT [20]. In TABLE III of [19], it is stated that the highest output power of the laser source is currently 25 kW, as compared to higher power microwave sources, which have 100 MW to 1 GW of peak power [21]. Researchers are working on several advancements to improve the effectiveness of power transfer employing lasers [19]. Regarding radiative WPT, microwave WPT is less expensive and simpler to connect with the current infrastructure when compared to light wave WPT.

1.3.2 Microwave PT

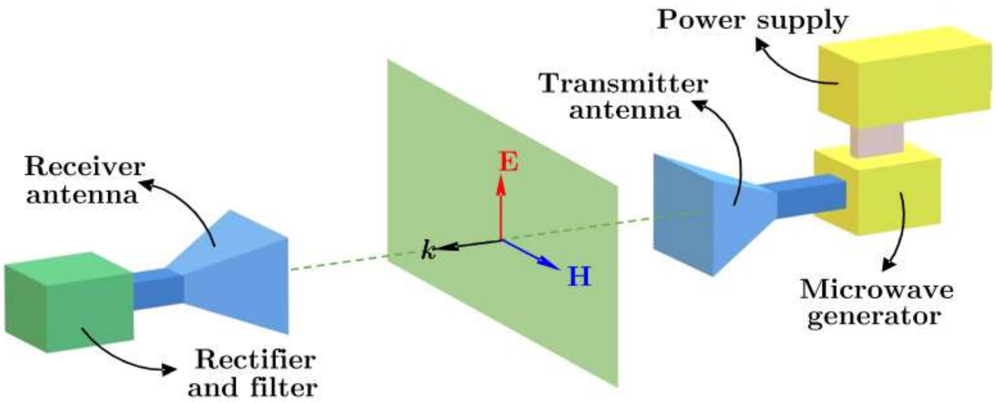

Figure 1.5: Schematic of a microwave WPT system.

Wireless Power Transmission (WPT) is a promising technique for the long-term power supply of wireless applications. Wireless power transfer via electromagnetic radiation is more efficient than IPT. WPT system radiates energy in the microwave regime towards the Rx. This energy is converted to DC using an RF-DC rectifier circuit. Figure 1.5 shows a basic schematic of a microwave power transfer system wherein the electric field (**E**) and magnetic field (**H**) are orthogonal. Studies on WPT are divided into the design of high-power microwave sources (e.g., magnetron), Tx-Rx antenna, EM wave propagation through media, and RF-DC conversion circuitry. Rectenna consists of a reception antenna, impedance matching circuits, filter circuits, and load. The practical antenna and system components' efficiency limits the transmitted power. The received power is attenuated, mainly due to free-space path loss and scattering due to various objects. Power transmission efficiencies depend primarily on the type of antennas, distance to which power is transmitted, operating frequency, and polarisation vector.

Nicola Tesla, a brilliant engineer and inventor, first presented the theory and a working example of WPT in 1897 [22]. To establish contactless power transmission to devices, he constructed the Wanderclyffe Tower, also known as the Tesla Tower (187 ft long). H. Hertz experimented with wireless transmission and detection of radio waves [23]. The studies reported by Tesla and the demonstration by Hertz launched a new age of WPT by successfully transmitting power without any physical connections. W. C. Brown successfully uses the microwave PT method to power a helicopter at 50 feet height [24]. A 5 kW magnetron supplies power to a dish reflector antenna positioned vertically at the source side. Also, space applications are discussed in [25]. The pioneers in microwave WPT have conducted numerous experiments in [26] -[36]. All are, however, restricted by a physical distance determined by Tx antenna aperture dimensions and path loss. In general, the far-field radius (R_{ff}) of an antenna with maximum dimension D and operating wavelength λ is given as $R_{ff} = 2D^2/\lambda$ [37]. However, microwave WPT can be employed for $R \geq R_{ff}$.

Table 1.1 compares various WPT systems based on power transfer effectiveness, distance, and receiver system mobility. According to the table, inductive WPT has a higher WPT efficiency but still only over very short distances. Also, there is no receiver system mobility during charging. Microwave WPT has a lower efficiency but can transfer power over very long distances (in metres or even kilometres). Additionally, as the receiver's position can direct the beam, receiver mobility is also addressed.

Table 1.1: Comparison of various WPT techniques.

WPT method	Efficiency	Distance	mobility
Inductive coupling	Very high	Very short	No
Resonant coupling	High	Short	Difficult
Laser or power beaming	Low	Long	Yes
Microwave transmission	Low	Very long	Yes

1.4 Literature survey

1.4.1 Friis transmission equation

In microwave WPT, an antenna plays a major role in transmitting and receiving EM waves. The antenna efficiency is practically limited by its radiation efficiency, power handling capacity, and other fabrication and position factors. Figure 1.6 presents geometry of the far-field microwave WPT system at $f_0 = 2.45$ GHz ($\lambda = \lambda_0 = 122.45$ mm). Here, P_r is received power (W), P_t is transmitted power (W), G_t and G_r are gains of Tx and Rx antenna respectively.

The antennas are spaced R distance (m) apart and $\hat{\rho}_t \cdot \hat{\rho}_r$ is the polarisation vector.

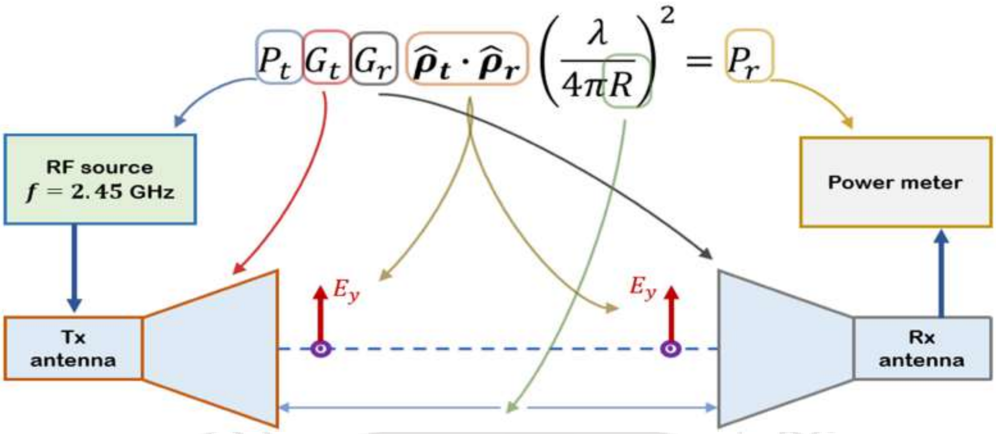

Figure 1.6: Geometry of antennas for Friis transmission equation.

The Friis transmission equation relates the power received to the power transmitted between two antennas separated by a distance $R \geq 2D^2/\lambda$. Let the transmitting antenna be an isotropic radiator with P_t as the input power and e_t as radiation efficiency, then the isotropic power density W_0 at a distance R from the antenna is [37],

$$W_0 = e_t \frac{P_t}{4\pi R^2} \tag{1.1}$$

For a non-isotropic radiator, the power density W_t in the direction θ_t, ϕ_t can be written as,

$$W_t = \frac{P_t G_t(\theta_t, \phi_t)}{4\pi R^2} = e_t \frac{P_t D_t(\theta_t, \phi_t)}{4\pi R^2} \tag{1.2}$$

The ratio of received to the transmitted power for reflection and polarisation matched antennas aligned for maximum directional radiation and reception is given as,

$$\frac{P_r}{P_t} = (\hat{\rho}_t \cdot \hat{\rho}_r) G_t G_r \left(\frac{\lambda}{4\pi R^2}\right)^2 \tag{1.3}$$

From (1.3), it is evident that P_r is the maximum for perfectly aligned antennas with identical polarisation. For a constant P_t at a constant frequency, the P_r measured at R will be maximised by refining the antenna gains.

1.4.2 Microwave WPT

Longer-distance power beaming is made possible by the ability to direct power transmission via radio waves at shorter wavelengths in the microwave region [38]. The NASA research on solar-powered satellites in 1978 suggested a transmitting antenna with a 1 km (0.6 mi) diameter and a receiving antenna with a 10 km (6.2 mi) diameter [39]. Due to the diffraction limiting in antenna directivity, microwave power beaming has the disadvantage of necessitating relatively large aperture diameters. Shorter wavelengths can partially reduce these diameters, although short wavelengths may encounter issues with air absorption and beam degradation by rain or water droplets.

Following World War II, which saw the development of high-power microwave emitters known as cavity magnetrons, the idea of using microwaves to transfer power was researched and widely established. Experiments in the tens of kilowatts were carried out in [32] -[36]. Power over Wi-Fi, developed in [40], allows charging and powering temperature sensors and battery-free cameras over Wi-Fi network transmissions. At distances of up to 20 feet, Wi-Fi signals have been demonstrated to power battery-free temperature and camera sensors.

1.4.3 Antenna shaping

The Friis transmission equation relates the antenna gains of the transmitter and receiver, operating frequency and the separation distance. Improving the antenna gains is a suitable choice for a far-field WPT system. The Tx antenna is crucial in achieving improved power transfer efficiency in WPT. The Rx antenna in the far field receives a directional beam of gain and lower half-power beamwidth (HPBW). Due to their high gain, low voltage standing wave ratio (VSWR), and wide bandwidth, pyramidal horns are employed in the microwave regime. In 1897, an Indian radio scientist, Jagadish Chandra Bose, built the first horn antenna, which used a circular waveguide and operated in the mm range [41]. Following this finding, various horn antennas have been built for different uses.

In the frequency range of 1.4 to 11 GHz, an antenna shape is tuned to match the impedance appropriately with the lower main lobe ripple [42]. Pyramidal horn antennas are developed in a variety of different forms to achieve constant beamwidth behaviour [43], create higher order modes [44] [45], and reduce cross polarisation [46], [47]. An enhanced version of the double-ridged guided horn (DRGH) [48] is developed with superior VSWR performance at higher frequencies. Its dimensions are equal to those of the standard DRGH [49].

The phase centre (PC) stabilisation of DRGH antenna is performed in [50] and for corrugated horn antennas in [51], [52]. The most significant PC deviation in [53] is 360 mm across 4 to 9 GHz. Several methods, such as employing a metal strip or rod inside the pyramidal antenna [54], a soft surface ring in a microstrip yagi array antenna to reduce surface waves [55], and a reconfigurable artificial structure in [56], have been proposed to increase the front-to-back ratio (FBR).

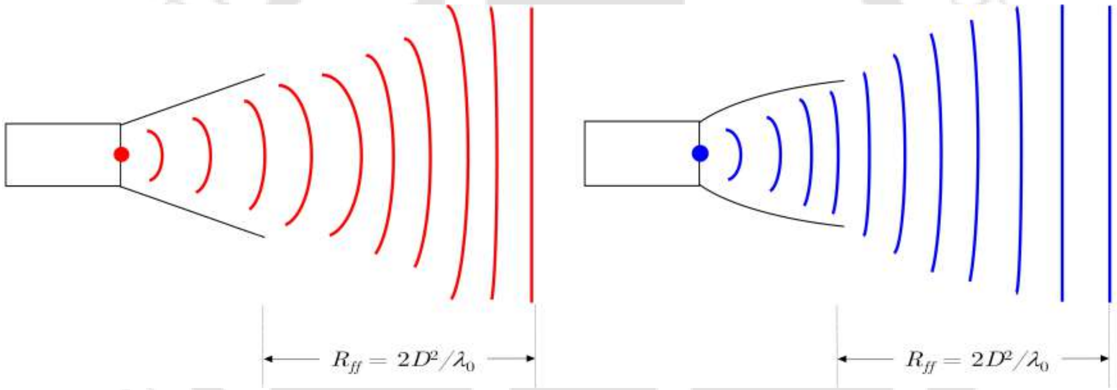

Figure 1.7: Schematic of basic antenna shaping and radiated field.

Figure 1.7 illustrates the radiation by an antenna wherein the red lines are illuminated from the phase centre of a Typical Pyramidal Horn Antenna (TPHA) and blue lines are illuminated from the phase centre of a Parabolic Pyramidal Horn Antenna (PPHA) [57] and aperture matched PPHA (APPHA) [58]. The parabolic shaping offers a gradual impedance match with the free space impedance ($\eta_0 = 120\pi = 377\Omega$). Therefore, the wave illuminated from the phase centre undergoes effective radiation of quasi-plane wave at the aperture. This results in the formation of plane waves early from the far-field radius ($R_{ff} = 2D^2/\lambda$). When used in practical application, a profiled antenna of equal aperture area shall radiate effectively within the given physical dimensions compared to TPHA. Hence, the antenna shaping method demonstrates conversion to a quasi-plane wave at the aperture.

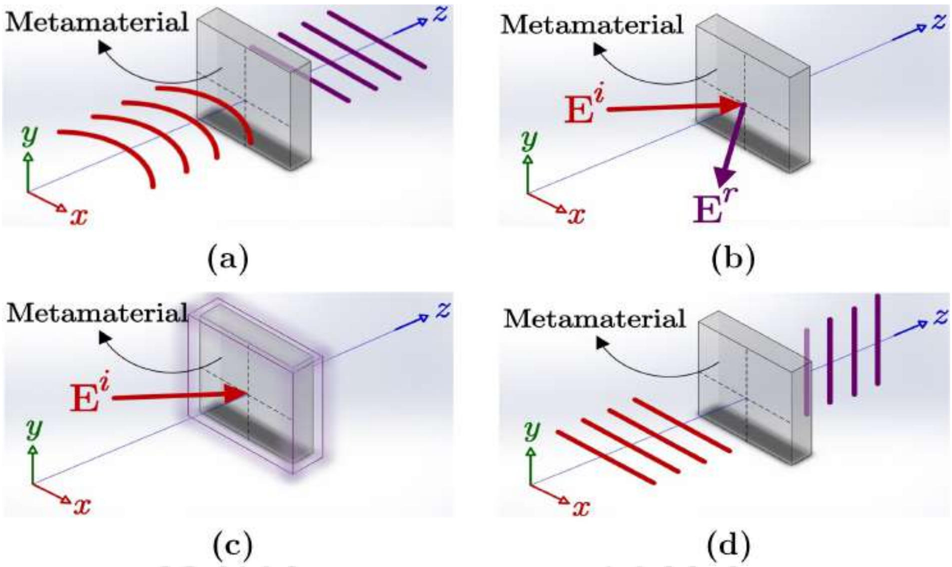

Figure 1.8: Illustration of different MM applications. (a) MM lens, (b) MM reflector, (c) MM absorber and (d) MM polarisation converter.

1.4.4 Microwave WPT using metamaterial

Metamaterial (MM) word combines 'meta' means beyond and material. It's a material whose properties are beyond a typical naturally available material. The properties such as negative index of refraction, absorption, transmittance, and reflectance are achieved by designing the metamaterial for the required application. Metamaterials are found to be used in narrowband and wideband applications as they can be tuned to achieve desired performance. MM's operating or resonant frequency is a function of constructional physical parameters such as dielectric constant, substrate thickness, conductor type, conductivity, metal area and gaps, etc. Figure 1.8 shows potential MM applications for (a) focusing, (b) reflection, (c) absorption, and (d) polarisation conversion for designed frequency.

The structural characteristics of an electromagnetic metamaterial, which are smaller than the wavelength, are affected by electromagnetic waves that interact or impinge on them. Its features must be significantly smaller than the wavelength to behave as a homogeneous material correctly represented by an effective refractive index. The wavelengths for microwave radiation are in the order of mm. Microwave frequency MMs are often built as arrays of electrically conductive components with the appropriate inductive and capacitive properties, such as wire loops, and split-ring resonators [59]. According to their characteristics, MM lenses fall into categories: negative index MM lenses [60] -[62], zero index MM lenses [63]-[64], and gradient refractive index (GRIN) lenses [65] -[69].

WPT's capability of delivering power without wires is certainly making it a necessity in today's society. By doing so, the dense network of cables may be eliminated, and one or more devices can be charged simultaneously. Both long- and short-range WPT have been shown and documented in the literature [26] -[31]. With the spiral super conducting MM, it is seen that WPT efficiency rises from 3.36% to 13.58%. A solenoid loaded with ferrite works as a unit cell for operating at lower frequencies [41]. At a distance of 4.5 cm and an operating frequency of 5.57 MHz, WPT shows a 10% improvement. Because all studies focus on non-radiative or near-field radiative WPT using MM, study for far-field radiative WPT has become a hot research field for exploration. The WPT employs the MM to boost the gain of the horn antenna and aperture effectiveness [60] -[69]. Figure 1.9 shows effective conversion to plane phase-fronts when EM wave incidences onto MM GRIN lens placed in front of the horn.

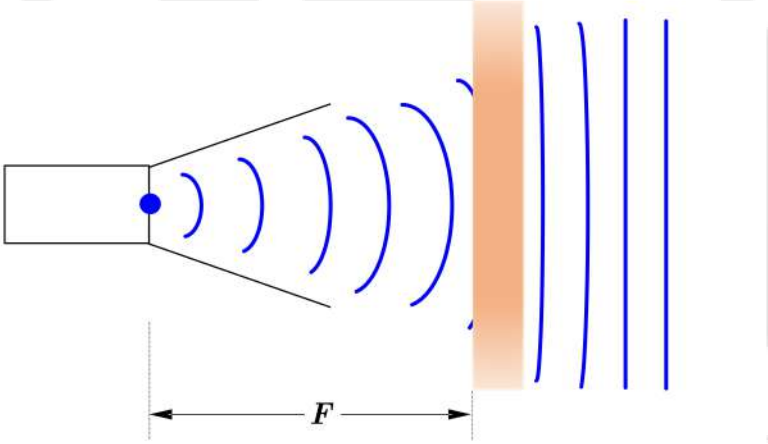

Figure 1.9: Schematic of an MM array and radiated field.

As the name implies, the refractive index of GRIN MM varies spatially and perpendicular to the transmission direction [70]. The highest refractive index is at the centre, and the minimum is at the corner of the lens. The variation of refractive index (n) exists for MM lens with radius r as $n(r) = n_0 - (\sqrt{r^2 + F^2 - F})/T$, where n_0 is the maximum refractive index along lens center, F is the optimum focal distance and T is the lens thickness [71]. The zero indexes MM, which has demonstrated an improvement in the directivity of the antenna, is designed to get the broadband property of MM [68]. The far-field WPT will be greatly enhanced by having a directional antenna and then employing MM at focus (F) to make it more concentrated.

1.4.5 Receiver side

After discussing several strategies for boosting and improving the gain of the Tx antenna, we now discuss improvement in the gain of the Rx antenna to increase the effectiveness of the WPT system. Due to its low cost and simplicity of production, a microstrip patch antenna is frequently employed in RF harvesting. Different low-gain microstrip patch antennas have been developed. It has been demonstrated that a cross dielectric resonator on a microstrip patch antenna provides gain better than 9 dBi across the band [72].

The inclusion of shortening wire in a Yagi wire-patch antenna results in resonance frequencies that are closer to the fundamental mode frequency and a gain of 14.8 dBi at 5.6 GHz [73].The antenna operating in Ku-band exhibits a continuous broadband gain of 10–10.5 dBi. The 10 dB impedance bandwidth and 3 dB gain bandwidth in [74] are 44% and 45%, respectively, due to the dual-layer metasurface.

The conical beam is produced by a circularly polarised monopole patch antenna with parasitic shorted patches. The patch has the vertically polarised electric field $E_{\theta 1}$, while the annular ring and parasitic shorted patches produce the horizontally polarised electric field $E_{\phi 1}$ [75]. In [76], the sequential phase feeding for the truncated patch antenna that is sandwiched between the metasurface and ground plane helps to increase the axial 3 dB ratio. It also enhances peak antenna gain to 12.08 dBi and exhibits a 10 dB impedance bandwidth of 58.06%. However, the radiation intensity on the aperture of the high-gain, low-performance microstrip patch antenna should be increased to convert the radiation into usable power for far-field WPT applications.

The power density at the Rx side (in this context, the position of the sensors, drone, or robot) should be higher to catch more radiation. This shall extract more power at the reception side. The feasible way to achieve this is to convert the plane wave into a spherical wave and position the low-gain patch antenna in the area of higher power density. By concentrating the plane wave at the focal, the parabolic dish reflector antenna aids in achieving the same. Research is being carried out to create a reflector antenna that is low-profile, lightweight, and flexible enough to be employed with sensors and Rx antennas of drones. Studies in [77] -[83] shows effective use of MM as a reflector for boosting the efficiency and is conceptually illustrated in Figure 1.8b.

1.5 Motivation

The modern wireless world demands the receiver's freedom from wired power requirements, thus offering ease of movement. This can be achieved with the WPT method. Using only the transmitter and receiver antenna would not achieve the desired efficiency. Hence, passive structures, i.e. metamaterials designed at the operating frequency, are used to focus the beam. The MM lens with low operation loss results in improved efficiency or distance. Design of such requires knowledge of various mathematical techniques, electromagnetic modelling tools and instruments used to analyse them. Simulation software such as Ansys HFSS, CST Studio Suite, Antenna Magus, COMSOL Multiphysics, Advanced Design System, Matlab, etc., are widely used to study and optimise the antenna dimensions and structures. The real-world experiments use a vector network analyser, electric field probe, spectrum analyser, power meter, and various passive microwave devices. Also, a high-power pulsed or continuous magnetron is generally used for practical measurements in an anechoic chamber.

Metamaterials (MMs) have found numerous applications in almost all devices operating between MHz and THz bands. The applications include aerospace, biological, chemical, electrical, electronics, and instrumentation. A wide range of applications and reduced fabrication complexity with modern PCB printing technology motivate us to explore the field of microwave WPT using MMs. The motivation is summarised below:

- The current literature portrays microwave WPT in the antenna's near-field, which under-utilizes the Tx antenna component. It is necessary to research how the antenna results in system efficiency in the far field.

- The current literature demonstrates MM-based plane-wave creation close to the antenna aperture. However, transforming the spherical wave into a plane wave with the additional improvement to the antenna radiation parameter using MM has yet to be investigated. Therefore, it is necessary to include MM for effective beaming with enhanced radiation characteristics.

- In WPT, it is imperative to increase the power density received at the receiver antenna. To achieve this, it becomes essential to design and test a compact, lightweight reflector antenna instead of a typical microstrip patch antenna. This combined setup is crucial for efficiently capturing electromagnetic waves at the focus. Such an arrangement serves as a fundamental foundation for supplying power to ground vehicles like robots, as well as aerial vehicles such as UAVs and aerostats.

- In simultaneous powering scenarios, it is required to direct the beam at distinct angles. The MM-based Tx or Rx reflector antenna can focus effectively to enhance efficiency in multi-directional beaming and SWIPT applications.

1.6 Objective of the thesis

The important objectives of this thesis are as follows:

- The MM structures described in the literature have applications at higher frequencies and are not designed for WPT frequencies, i.e. 2.45 GHz and 5.8 GHz. A MM structure for a 2.45 GHz operating frequency will be designed.
- The reported structures are complex structures and electrically large in size. An array with a smaller size and easier fabrication will be designed.
- A typical microwave WPT system in free space generally exhibits a very low overall system efficiency. A feasibility study of efficiency improvement in 2.45 GHz far-field microwave WPT using MM GRIN lens for a 1-meter distance will be carried out.
- Methodology will be developed for electric field improvement in far-field automated mobile vehicle charging applications. This can be accomplished with a high-power magnetron and MM GRIN lens at Tx to focus the beam. The Rx side can be lightweight and compact using a planar MM reflector and a patch antenna.
- In the current scenario, SWIPT applications are required to utilise power in sidelobes to charge small IoT devices. Therefore, an MS-based reflector antenna to simultaneously focus the beam in distinct angles will be studied.

1.7 Contribution of the thesis

The major contributions of the thesis are as follows,

- A WPT system using microwave frequency is detailed with its components for better understanding. An antenna is a key element in microwave WPT, used for transmitting and receiving power at a distance more significant than the antenna. Friis transmission equation relates transmitted power, received power, distance, antenna gains, and operating frequency. A literature review on WPT and WPT efficiency enhancement employing metamaterials is presented. A motive for far-field microwave WPT using MM is outlined, followed by a set of objectives.

- A MM unit cell is designed and optimised for 2.45 GHz operating frequency. The suggested MM unit cell enhances the transmission efficiency and has a positive refractive index. This lens efficiently concentrates the incident wave when placed at the focus of the transmitting horn antenna. When the strips are set at a spacing of $0.008\lambda_0$ apart, the array gain of 10.79 dBi with reduced half-power beam widths is achieved. This study established a baseline for future discussions on the charging applications of mobile vehicles such as robots, drones, aerostats, and other similar devices.

- The enhancement in the received electric field for rover charging at 3 m with a high-power magnetron (800W) is presented. On the transmitting side, an MM array focuses the beam more effectively, increasing antenna gain and reducing the half-power beam widths. Since the rover is mobile, it can handle lightweight and tiny receiving antennas like the patch. Therefore, a compact planar MM reflector array with a patch positioned at focus is used for better reception. By using the novel MM reflector, it is possible to reduce the time required for the battery to charge. Compared to a conventional system without MM, the electric field with MM lens at Tx and MM reflector at Rx is increased by a factor of two.

- A unique metasurface sub-reflector-based dual reflector antenna inspired by the Cassegrain antenna for simultaneously beaming electricity in distinct angles is presented. Changing the focal distance of the MSSR array, the power distribution in the main lobe and sidelobe can be adjusted. Additionally, the gain in the primary direction and the HPBW may be altered. The proposed antenna found applications when several miniature targets spaced at sidelobes are to be charged simultaneously. Experiments are carried out by constructing a prototype of an MSSR-based Cassegrain antenna, and the performance of the proposed antenna at 2.45 GHz is evaluated by designing a perfectly reflecting MS unit cell. The electric field is tested, and the results displayed greater values at three different angles, including the primary direction, demonstrating a remarkable capability of simultaneous beaming.

- An innovative machine-learning (ML) technique using random forest regression (RFR) to predict radiation properties in planar metasurface reflector (PMSR) antennas at 2.45 GHz is presented. The RFR model is trained using PMSR parameters, and results closely align with experimental and CST data. This approach is beneficial for assessing antenna radiation in non-line-of-sight or misaligned receiver scenarios, offering a foundational study and design reference for lightweight, planar mobile reception reflector antennas. Chapter 6 presents the future scope and applications of microwave WPT technology using MM.

1.8 Organisation of the thesis

From the discussions of various aspects of microwave WPT in the literature, it is apparent that the free space propagation of EM waves suffers from path loss, and the field is reduced by the square of the distance. Also, the antenna aperture and physical dimensions must be occupied in the current system physique. Therefore, it is necessary to assess the performance of included MM at every stage of system design. The objectives are divided into four chapters, and the future work is summarised in the final chapter.

Chapter 2 uses MM as a GRIN lens that focuses the beam towards Rx placed at 1 m. This study creates a basic formulation for high-power charging applications. Chapter 3 describes a methodology of Rx field improvement in a rover charging case study. The sidelobe power can also be used to charge tiny IoT devices that possess very low power consumption. Therefore, simultaneous beaming in multiple directions is achieved with a planar MSSR Cassegrain antenna in Chapter 4. Due to its compact size and lightweight structure, the planar MS reflector offered an ease in placement. In the Chapter 5, for the prediction of power distributions and gain in the principal plane of this reflector-feed arrangement, a random forest regression machine learning technique is adopted. A good agreement between the actual and predicted results are observed. The conclusions of the work are given in Chapter 6, wherein MMs' versatile capability allows them to be used in far-field charging and space-based solar power.

Chapter 2

Feasibility study of far-field WPT using GRIN MM

Overview

This chapter presents a feasibility study of metamaterial incorporated far-field microwave WPT at 2.45 GHz. The proposed MM unit cell exhibits a positive refractive index and is used as an array with graded-refractive index property that focuses the incident wave effectively. The array placed at an optimum distance ($= 2.5\lambda_0$) from the transmitter horn achieves a 10.79 dBi gain when the strips are spaced $0.008\lambda_0$ apart. This study creates a baseline for the charging of robots, drones, aerostats, etc., and charging applications discussed further.

2.1 Introduction

2.1.1 Far-field WPT/WEH system

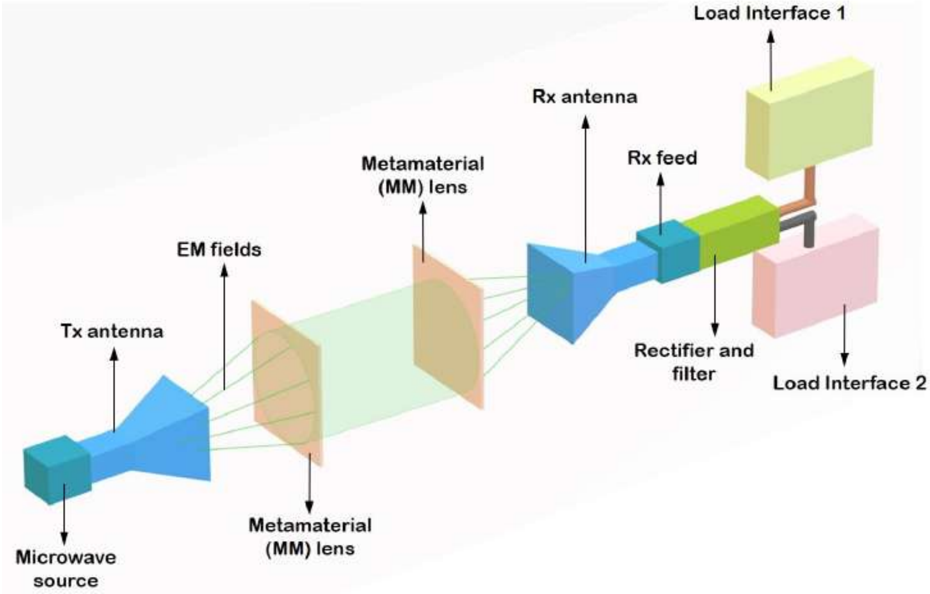

Figure 2.1: Schematic of a far-field microwave WPT system employing metamaterial (MM) as a lens.

Wireless Power Transfer is the latest trend to make the system independent of physical connections from the source. Wireless Power Transfer (WPT)/Wireless Energy Harvesting (WEH) was first introduced by Nicola Tesla. Since then, pioneers in this field have been doing research continuously to make it easy and efficient. Continuous research in this combined field of microwave beaming, reception, and conversion has been carried out since this successful demonstration by Hertz. Nowadays, advanced material science has brought resonating structures to start an era of artificial or man-engineered materials that result in efficient and reliable WPT/WEH systems. Metamaterial exhibits refractive index properties that alter, modify, improve, and couple incident fields when tuned to the desired operating frequency. This makes it useful in various applications, including partial, complete or zero reflection, absorption, and transmission. The use of metamaterials and tuning them to the required frequency is becoming efficient and easy to install due to the availability of microwave components and dielectric sheet fabrication facilities in the market.

The present study relates to transferring/harvesting power through electromagnetic waves to/at a system without physical electrical wires or cables. The system uses a transmitting horn antenna operating in S-band (2.2-3.3 GHz) fed by a microwave source. The receiving

D-dot sensor is placed at a far-field line of sight in the RF absorber environment. The MM strips supported by PVC pipes and thermocole sheets enhance the gain and system efficiency by concentrating the beam in the propagation direction. This arrangement transmits the power from the horn antenna to the D-dot sensor connected virtually by electromagnetic waves*.

2.1.2 Microwave WPT using MM

H. Hertz [23] performed the first experiment that launched a new age of wireless power transmission by successfully transmitting power without any physical connections. This microwave technology was utilised to power a helicopter at the height of 50 feet [24] and for space purposes [25]. A far-field WPT approach uses a high-power generator at the transmitting (Tx) end and an RF-DC rectifier, or a rectenna, at the receiving (Rx) end to give the receiver freedom of movement [27]. For increasing the received power, such a rectenna array is shown in [26], [28], [34]. Improved received power is provided by a receiving antenna array that is employed in [26] with 2304 elements and in [34] with 8 elements respectively. The approach of boosting overall system efficiency is still a subject of continuing study.

An approach to maximise near-field efficiency using duty cycle optimisation is presented in [84]. However, structuring the receiver with a ferrite-based structure enhances Tx-Rx coupling [85] while adding bulk to the system. Inserting MM after the transmitter antenna can be used to focus or steer the beam towards the receiver. Metamaterials are employed as a lens in [30], [86] -[91] to concentrate the transmitted power toward the Rx while maintaining the present system's physical characteristics, including the size, positioning, and arrangement of the Tx and Rx. By functioning as a concentrating element, MM is vital for higher efficiency. However, compared to three-dimensional refractive index material [92], uniform refractive index material—such as the planar lenses employed in [30], [86] -[91] cannot increase the radiation efficiency of antennas. To focus the power, MM with graded refractive index (GRIN) property [70] is adopted after Tx, where the refractive index is a function of

---

*[*] **Shashank S. Kulkarni**, Amit Kumar Baghel, Sisir Kumar Nayak, and D. Senthil Kumar, "Far-field Wireless Power/Energy Transfer/Harvesting to/for Manned and/or Unmanned Systems using Metamaterial," Indian patent no.: 201931023905, published on 12/07/2019.

space [91], [93], [94].

Quasi-spherical waves are transformed into plane waves by a 3D half Maxwell Fish-eye GRIN lens with a trapezoid-shaped monopole antenna developed in [67]. A GRIN MM that transforms cylindrical waves into plane waves was introduced by Hui Feng Ma et al. in [68]. Additionally, with a 1 GHz bandwidth between 7.5 and 8.5 GHz, it demonstrates beam deflection capabilities. A mechanism for creating high refractive index artificial dielectric was introduced in [95], producing a focused beam at higher refractive index values. For frequencies from 60 to 380 GHz, a metallic metamaterial with regular slits was presented in [96]. With an extra phase shift correction factor, the observed effective refractive index is nearly 5.5. With a 44% increase in bandwidth between 0.39 and 0.65 THz, the refractive index in [97] can obtain a high value of 27.

A metamaterial-based three-dimensional high directivity broadband lens antenna was developed in [98]. The antenna gain increases to 19.8 dB at 8.2 GHz and 23 dB at 12.2 GHz with the addition of MM. With four beam antenna, a 3D GRIN lens MM for 3 to 7.5 GHz published in [99] has greater sidelobes. It offers improved directional capabilities to steer and shape the antenna's beam. Antenna efficiency is increased by a wideband transmitarray with a three-layered air-gaped unit cell presented in [100]. In this study, WPT is used in the industrial, scientific, and medical (ISM) band at a frequency of 2.45 GHz. The planar and GRIN lens MM frequencies listed in the literature are other than S-band frequencies.

The WPT with GRIN MM for 2.45 GHz given in [71] only displays the real portions of the effective parameters; imaginary values are left unaddressed. Additionally, the system is bulkier and larger due to the positioning distance of the MM array from the Tx aperture, which is $4.93\lambda_0$. However, a zero resonating order wire-based mm inspired antenna in [101] is suitable for near field applications due to its small gain, i.e. 2 dBi.

Therefore, in this chapter, an MM GRIN lens that exhibits the magnetic dipole and the GRIN lens property at 2.45 GHz was designed and demonstrated experimentally. It increases η_{sys} to 32.6% and reduces the half-power beamwidth compared to a system without MM when positioned at $R_{opt} = 2.5\lambda_0$ from the Tx antenna. The relative permittivity (ε_r) and relative permeability (μ_r), which have real positive values and imaginary values that are close to zero, provide an overall positive refractive index (n) by focusing incident EM waves.

2.2 The gradient refractive index (GRIN) lens

A lens is a transmission optical device that employs refraction to concentrate or scatter a light beam. A simple lens comprises a single transparent component, whereas a compound lens comprises numerous simple lenses (elements) generally aligned along a common axis. Ground and polished or moulded to a specific form, lenses are created from materials such as glass or plastic. Unlike a prism, which refracts light without concentrating, a lens can focus light to produce an image. Microwave, electron, and acoustic lenses similarly concentrate or disperse waves and radiation other than visible light. Various image equipment utilises lenses, such as telescopes, binoculars, and cameras. They're also employed as visual aids in glasses to help correct vision problems.

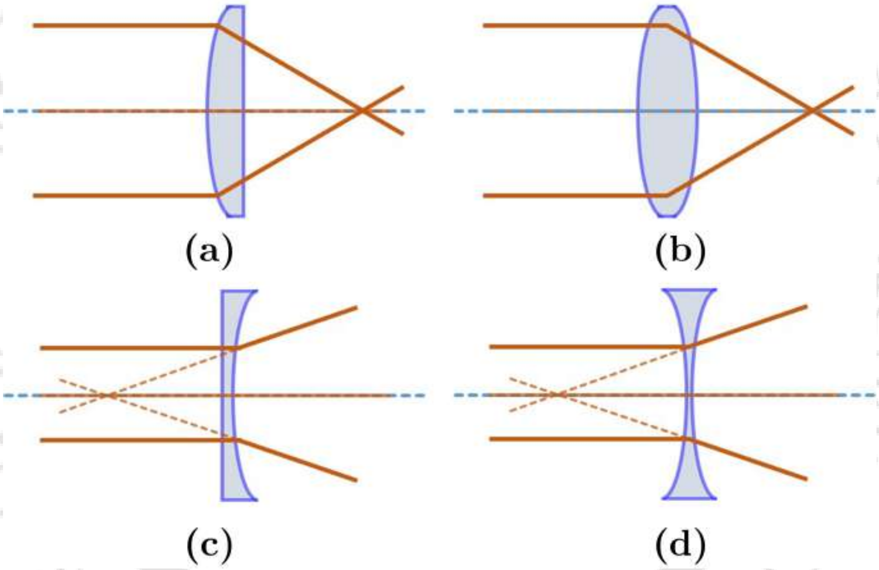

Figure 2.2: Various types of lenses. (a) Plano-convex, (b) double-convex, (c) plano-concave, and (d) double-convex.

Figure 2.2 illustrates different lens types and ray trajectories passing through them. The curvature of the two optical surfaces is used to classify lenses. If both lens surfaces are convex, it is called biconvex (or double convex, or simply convex). The lens is equiconvex if both surfaces have the same radius of curvature. Biconcave refers to a lens having two concave sides (or concave). The lens is plano-concave depending on the curvature of the other surface if one of the surfaces is flat.

A collimated beam of light flowing through the lens converges to a point (a focus) behind the lens if the lens is biconvex or plano-convex. The lens is known as a positive or converging lens in this scenario. The focal length of a narrow lens in air is the distance between the lens and the spot, often represented as f. A collimated beam of light travelling through the lens is divergent (spread) if the lens is biconcave or plano-concave; the lens is then called a negative or diverging lens. The beam propagates through the lens and emanates from a particular point on the lens axis. A gradient refractive index lens wherein the RI is a function of space is presented in Figure 2.3. A ray converges at the focus after passing through rectangular geometry. It is observed that the GRIN lens offers effective convergence with flat boundaries compared to double-convex and plano-convex lenses. This makes a practical fit for GRIN distribution in lens applications.

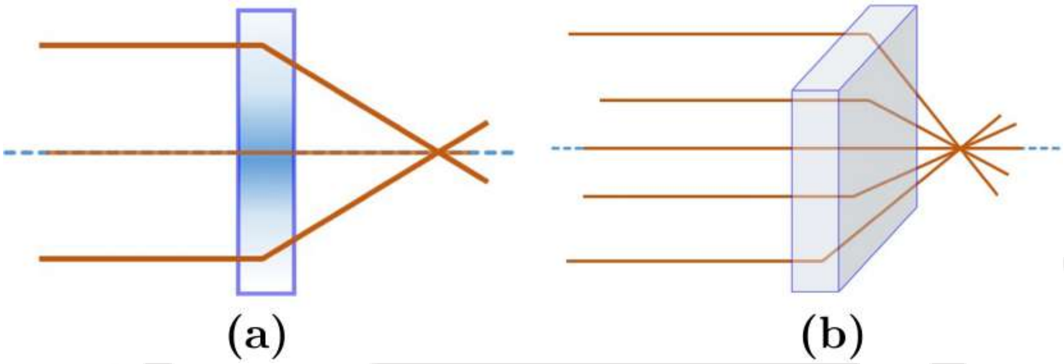

Figure 2.3: Illustrations of a Graded Refractive Index lens. (a) Cross-sectional and (b) perspective view.

2.3 Theory

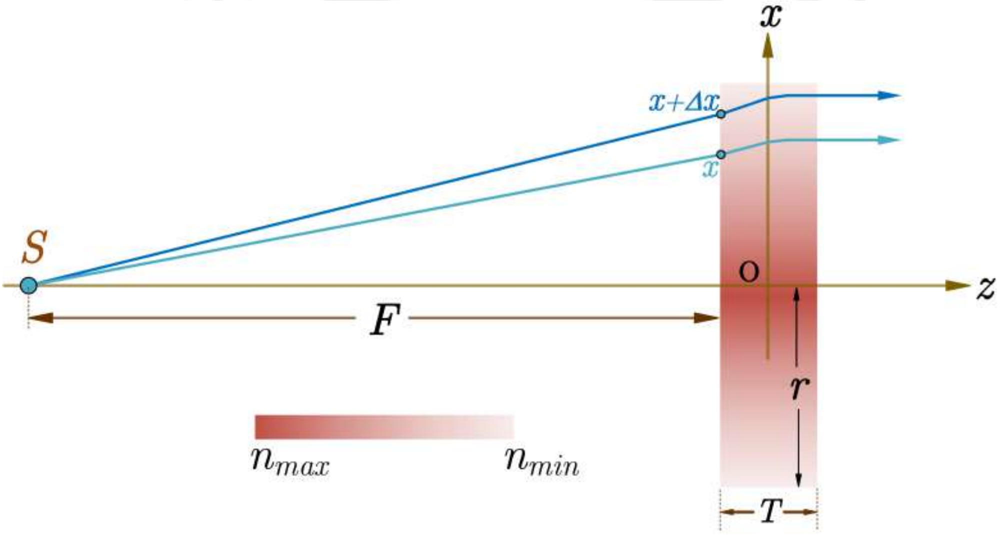

Figure 2.4: Cross section view of a GRIN lens with ray path inside the GRIN medium.

The cross-section of a gradual variation of refractive index along the radius r and finite thickness T is illustrated in Figure 2.4. The GRIN distribution transforms the spherical wavefront emitted by source S located at spatial focus F to planar wavefront at the exit plane $z = +T/2$ of an MM GRIN lens. To simplify the construction of the GRIN lens, we assume that waves travel along straight lines normal to the lens interface. The coordinate origin is positioned at the lens' geometric centre. Considering that two rays enter the slab at different positions along the thin slab's surface, the optical pathways from the source (S) to the wavefront of the exit wave should be identical; hence, we have

$$n_1\sqrt{x^2+F^2} + \int_{-T/2}^{+T/2} n(x,z)dz = n_1\sqrt{(x+\Delta x)^2+F^2} + \int_{-T/2}^{+T/2} n(x+\Delta x,z)dz \tag{2.1}$$

We suppose the lens' refraction index varies in both the x- and y-directions. The relative refraction index is unity ($n_1 = 1.003$) since free space functions as the underlying material. The optical path length equation will be

$$\int_{-T/2}^{+T/2} \frac{n(x+\Delta x,z)-n(x,z)}{\Delta x}dz = \frac{\sqrt{x^2+F^2}-\sqrt{(x+\Delta x)^2+F^2}}{\Delta x} \tag{2.2}$$

When $\Delta x \rightarrow 0$, the right hand side of (2.2) is written as

$$\lim_{\Delta x\rightarrow 0} \frac{\sqrt{x^2+F^2}-\sqrt{(x+\Delta x)^2+F^2}}{\Delta x} \tag{2.3}$$

The solution can be found using Taylor's expansion series. The Taylor series of a function is the infinite sum of terms represented in terms of the function's derivatives at a single point. The function and the sum of its Taylor series are equal for most common functions. The Taylor series of an infinitely differentiable function $f(x)$ with real or complex values at real or complex number a is the power series and, in sigma notation, is given by

$$f(a) + \frac{f'(a)}{1!}(x-a) + \frac{f''(a)}{2!}(x-a)^2 + \cdots = \sum_{n=0}^{\infty} \frac{f^n(a)}{n!}(x-a)^n \tag{2.4}$$

where $n!$ denotes the factorial of n and where $f^n(a)$ denotes the n^{th} derivative of f evaluated at the point a. Here, f itself is defined as the derivative of order zero, and the values of

$(x-a)^0$ and 0! are specified as 1. Therefore, (2.3) becomes

$$\lim_{\Delta x\to 0}\frac{\sqrt{x^2+F^2}-\sqrt{(x+\Delta x)^2+F^2}}{\Delta x} = -\frac{x}{(x^2+F^2)^{1/2}}-\frac{F^2\Delta x}{2(x^2+F^2)^{3/2}} \\ +\frac{xF^2\Delta x^2}{2(x^2+F^2)^{5/2}}+\frac{F^2\Delta x^3(F^2-4x^2)}{8(x^2+F^2)^{7/2}}+\cdots \tag{2.5}$$

As $\Delta x \to 0$, (2.5) reduces to

$$\lim_{\Delta x\to 0}\frac{\sqrt{x^2+F^2}-\sqrt{(x+\Delta x)^2+F^2}}{\Delta x} = -\frac{x}{\sqrt{x^2+F^2}} \tag{2.6}$$

Putting (2.6) in (2.2) and letting $\Delta x \to 0$ in the left hand side, (2.2) is written as

$$\int_{-T/2}^{+T/2}\frac{dn(x,z)}{dx}dz = -\frac{x}{\sqrt{x^2+F^2}} \tag{2.7}$$

Integrating (2.7) with respect to x results

$$\int_{-T/2}^{+T/2} n(x,z)dz = n_{max}T-\sqrt{x^2+F^2}-F \tag{2.8}$$

The curved path length inside an inhomogeneous lens, when discretized in small sections, follows a linear variation, and $n(x,z)$ must satisfy the following equation:

$$n(x)T = \int_{-T/2}^{+T/2} n(x,z)dz \tag{2.9}$$

and the variation along the radius $x=r$ and can be expressed as

$$n(r) = n_{max}-\frac{\sqrt{r^2+F^2}-F}{T} \tag{2.10}$$

where n_{max} is the maximum refractive index along the center and $n_1 = 1.003$ is the refractive index of free space. As seen from (2.10), a larger variation in refractive index range would reduce lens thickness [65] and results in effective beam conversion [71]. Also, it can be noted that both the small values of F and n_{max} produce large T [102]. However, this work considers a gradual and smooth refractive index reduction from the centre to the lens thickness for directional antenna design aimed at optimum power delivery in microwave WPT.

2.4 Design and analysis

2.4.1 MM unit cell

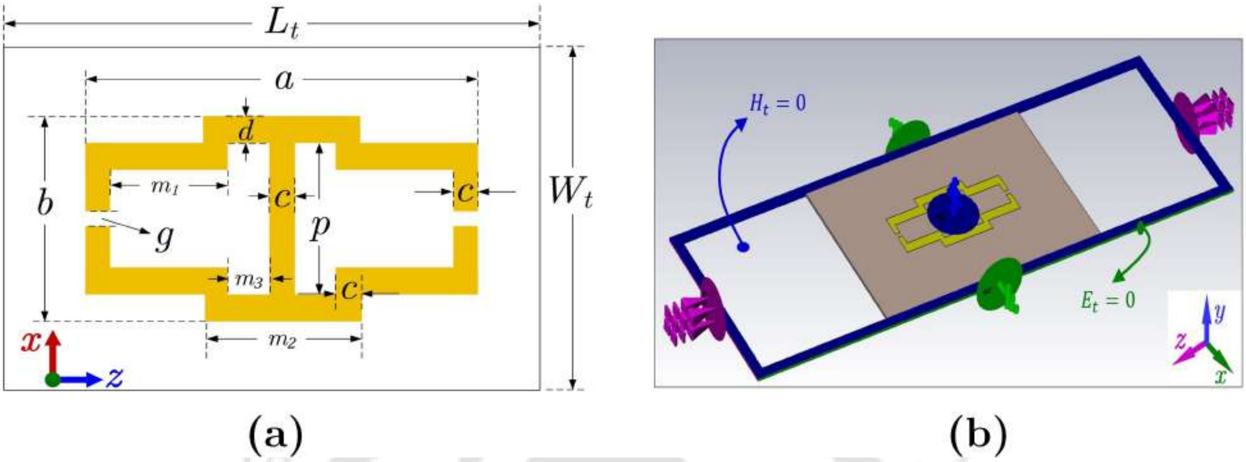

Figure 2.5: (a) Geometry of the proposed MM unit cell. (b) Simulation boundary conditions for proposed MM unit cell in CST.

The design of a unit cell is a fundamental aspect of lens design refining, which results in the desired value of a refractive index. Hence, this section analyses and presents the modelling unit cell by an equivalent electrical model with impedance and reflection coefficient. Figure 2.5a illustrates the geometry of the proposed MM unit cell designed on Rogers RT5880 duroid substrate. A 35 μm thick copper layer is utilised on a base substrate with relative dielectric constant $\varepsilon_r = 2.2$.

Table 2.1: Unit Cell parameters optimised for $f_0 = 2.45$ GHz

parameter	value (λ_0)	value (mm)	parameter	value (λ_0)	value (mm)
a	0.212	26.96	m_1	0.061	7.47
b	0.102	12.49	m_2	0.090	11.02
c	0.008	1	m_3	0.033	4.04
d	0.012	1.47	L_t	0.4	48.98
g	0.004	0.5	W_t	0.305	37.35
p	0.069	8.45	h	0.004	0.5

In the upper half, a rectangular strip of length m_2 along the $z-$axis and width d along the $x-$axis is made at first. Two strips each of length m_1 and width d in the $x-$axis are attached at the ends keeping the width c along $z-$axis. An identical structure is created in the lower half of the substrate. A closed ring structure is formed by adding two vertical strips at the outer edges. The vertical strip has length $p - 2d$ along $x-$ and width c along

$z-$axis. Subtracting a strip of width g along $x-$ at the centre of the geometry creates a gap. The effects on reflection due to variation in the gap g are discussed later. Finally, a strip of length p along $x-$ and width c along $z-$axis joins the upper and lower half-strips at the centre of the middle strip. The designed MM cell exhibits symmetry along both the design axes, i.e. xoz plane. The optimised dimensions for $f_0 = 2.45$ GHz and hence $\lambda_0 = 122.45$ mm as an operating wavelength are tabulated in Table 2.1.

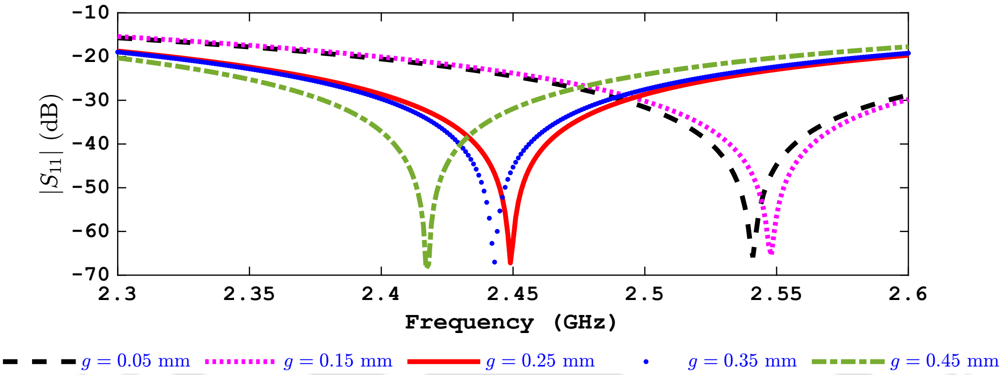

Figure 2.6: Simulation variation of $|S_{11}|$ with frequency for $0.05 \leq g \leq 0.45$ mm.

The cubic dimensions of the unit cell are $48.98 \times 37.35 \times 0.5$ mm^3 designed in commercial electromagnetic modeller CST studio suite. A linearly polarised excitation along the $y-$axis is provided, defining electric and magnetic boundary conditions as depicted in Figure 2.5b. The solver computes two-port network parameters for defined excitation in time domain solver mode. The constructional parameters affect the responses as time-varying electromagnetic fields interact with the unit cell. Therefore, variation of complex S_{11} with for different strip gap values ($0.05 \leq g \leq 0.45$ mm) is plotted in Figure 2.6. The resonant notch is lowered when g increases from 0.05 mm to 0.45 mm in steps of 0.1 mm. An increment in the conductor spacing distance changes the effective capacitance experienced by the unit cell.

Figure 2.7 illustrates the formation of capacitance ($C = \varepsilon Area/g$) and inductance ($L = \mu N^2 Area/\ell$) between two conductor strips spaced g apart. The practical limits of fabrication include tolerances for uniform, thick, evenly spread copper layers. The obtained EM responses are a function of the constructional parameters of the unit cell. When the effective length ($= \ell$) of conducting strips is increased, the inductance is decreased and capacitance is increased. Similarly, for higher values of g, the capacitance is decreased, and inductance is increased for a constant cross-section area ($= Area$) of the conductor. Due to the inverse proportionality, the obtained EM responses exhibit a frequency shift for the optimum transmission in the simulation band. The reflection coefficient shows a perfect transmission to incident wave for all values of g and is evident from Figure 2.6 that $|S_{11}| \leq -15$ dB between $2.3 - 2.6$ GHz. A simultaneous change in inductance and capacitance with variation in cell gap offers fine-tuning of the proposed MM aimed for the desired application in an entire simulation frequency range.

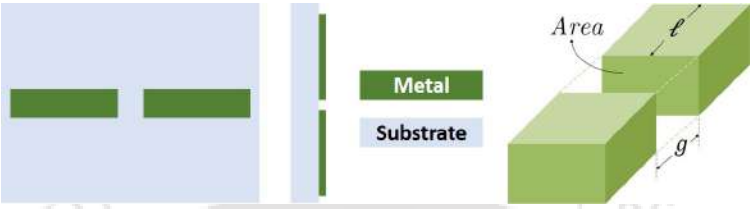

Figure 2.7: Illustration of capacitance formation and inductance between two conducting strips.

The transmission, reflection, and absorption offered to an impinging electromagnetic wave are based on the constituent medium properties used in electromagnetic modelling. The effective medium parameters viz. electric permittivity ($\varepsilon_e = \varepsilon^{'} \pm \varepsilon^{''}$), magnetic permeability ($\mu_e = \mu^{'} \pm \mu^{''}$), and refractive index ($n_e = n^{'} \pm n^{''}$) define the propagation velocity, complex dissipation factor, and wave impedance. Therefore, determining effective medium parameters is a fundamental aspect of lens design. The complex scattering parameters (S_{11} and S_{21}) are utilized to extract ε_e, μ_e, and n_e of unit cell. The complex medium parameters for normal incidence on a homogeneous slab of thickness h are related to $S-$parameters as [103]:

$$S_{11} = \frac{Z_e(1 - e^{2jn_e\kappa_0 h})}{1 - Z_e^2[e^{2jn_e\kappa_0 h}]} \tag{2.11}$$

$$S_{21} = \frac{(1 - Z_e^2)e^{jn_e\kappa_0 h}}{1 - Z_e^2[e^{2jn_e\kappa_0 h}]} \tag{2.12}$$

$$\eta_e = \pm\sqrt{\frac{(1 + S_{11})^2 - S_{21}^2}{(1 - S_{11})^2 - S_{21}^2}} \tag{2.13}$$

$$e^{jn_e\kappa_0 h} = \frac{S_{21}}{1 - S_{11}Z_e} \tag{2.14}$$

where $Z_e = (\eta_e - 1)/(\eta_e + 1)$, η_e is the wave impedance and $\kappa_0 = 2\pi/\lambda_0$ is a phase constant.

Figure 2.8 illustrates the variation of extracted complex effective medium parameters with the frequency. Variation of complex reflection coefficient $[\Re(S_{11}) \pm \Im(S_{11})]$ for 2-2.9

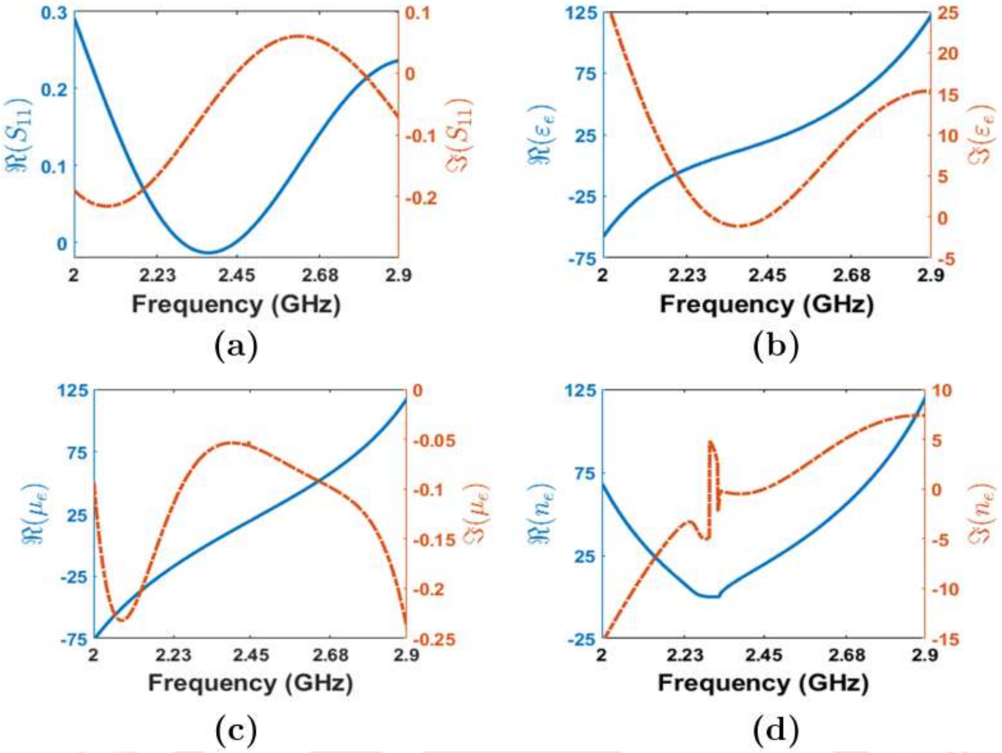

Figure 2.8: Extracted effective medium parameters of MM unit cell. (a) Electric permittivity (ε_e), (b) magnetic permeability (μ_e), and (c) refractive index (n_e).

GHz is presented in Figure 2.8a. A stable response is observed between 2.32-2.47 GHz for the real part (indicated in blue). The imaginary part shows a maximum of 0.06 at 2.64 GHz and a minimum of -0.206 at 2.1 GHz. A positive value for 2-2.8 GHz and a negative value for 2-2.45 GHz is observed. At the operating frequency, $S_{11} = 0.001 + j0$ is obtained, which results in perfect transmission to the incident wave. At $f_0 = 2.45$ GHz, the obtained values are $\varepsilon_e = 19.45 - j0.004$, $\mu_e = 19.47 - j0.057$, and $n_e = 19.46 - j0.031$.

It is observed that the unit cell exhibits approximately equal and positive real parts at 2.45 GHz. The imaginary parts of ε_e and μ_e, however, are negative and also close to zero, resulting in an overall positive value of n_e. A low-loss operation due to near-zero values of effective medium parameters is concluded. Also, a higher positive real part at the operating frequency would effectively focus the incident beam [71]. The interaction between the incident electromagnetic field and a unit cell comprising finite inductance and capacitance gives rise to impedance losses. The eddy currents induced at the conductor surface cause heat dissipation, resulting in reactive losses represented by an imaginary part. The real part represents ohmic losses and is incorporated in an external resistance R_{ext} in an equivalent electric model.

2.4.2 Equivalent electrical modelling

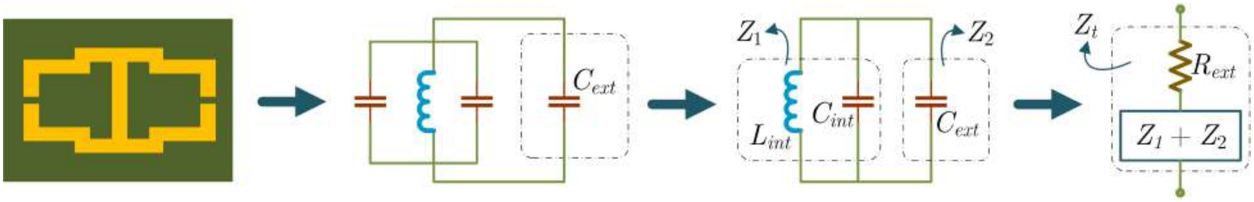

Figure 2.9: Equivalent electrical model of MM unit cell.

Figure 2.9 presents an electric equivalent unit cell model. The finite length and width conducting strips represent an equivalent internal inductance L_{int} in parallel with the internal capacitance C_{int}. A gap g between the two complementary conducting plates is responsible for capacitance formation. An external capacitance C_{ext} experienced is due to the dielectric constant (ε_r) of the substrate. Two individual impedances $Z_1 = j(\omega L_{int} \parallel -1/\omega C_{int})$ and $Z_2 = -j/\omega C_{ext}$ are in series with an external resistance R_{ext} representing ohmic losses. The total impedance is an algebraic sum of R_{ext}, Z_1, and Z_2 obtained as:

$$Z_t = R_{ext} - j\left[\frac{\omega^2 L_{int}(C_{int} + C_{ext}) - 1}{\omega C_{ext}(\omega^2 L_{int} C_{int} - 1)}\right] \tag{2.15}$$

Equating imaginary part of (2.15) to 0 gives an operating frequency $\omega_0 = 1/\sqrt{L_{int}C}$ where $C = C_{int} + C_{ext}$ is the total capacitance. The capacitance of a coplanar capacitor is expressed as [104]:

$$C_{int} = \frac{2\varepsilon_0}{\pi} ln\left[\frac{2\alpha G_C}{g}\right] D_C \tag{2.16}$$

$$C_{ext} = \frac{\varepsilon_0(\varepsilon_r - 1)D_C}{\left[\frac{g}{h} + \frac{4ln(\alpha)}{\pi}\right]} \tag{2.17}$$

where G_C is the gap measured by considering the width (c) of the conducting strips, D_C is the total width of the conducting strips between which capacitance is formed, and $\alpha = n\omega/c$ is a constant. In the above case, gap $G_C = 2$ mm, $D_C = 1$ mm, and $g = 0.5$ mm that results $C_{int} = 0.0506$ pF, $C_{ext} = 0.001$ pF, and $C = 0.0517$ pF.

The self-inductance of a thin film conducting strip is approximated as [104]:

$$L_{int} = \frac{\mu_0 \ell}{2\pi}\left[ln\left(\frac{2\ell}{D_L}\right) + \frac{1}{2} + \left(\frac{D_L}{3\ell}\right) - \left(\frac{D_L^2}{24\ell^2}\right)\right] \tag{2.18}$$

where ℓ is the length and D_L is the width of a conducting strip respectively. From the optimised geometrical dimensions, $\ell = 68.71$ mm and $D_L = 0.6$ mm. Thus, the inductance of a unit cell is $L_{int} = 81.583$ nH. From circuit analysis, an operating frequency of the unit cell extracted from (2.15) is $f_0 = 1/2\pi\sqrt{L_{int}C} = 2.449$ GHz.

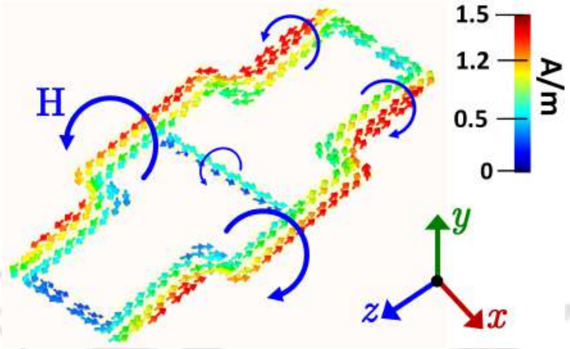

Figure 2.10: Simulation distribution of surface current at 2.45 GHz.

Figure 2.10 depicts the simulation distribution of surface currents and induced magnetic field intensity ($\mathbf{H}$) on the unit cell at 2.45 GHz. A circulating loop current is observed in the xoz plane, resulting in net magnetic dipole moment as,

$$\mathbf{m} = I\mathbf{S} = IS\mathbf{a}_n \tag{2.19}$$

As the surface area (S) is constant, higher values of $\mathbf{m}$ correspond to increments in I. This also increases magnetisation,

$$\mathbf{M} = \frac{\mathbf{m}}{V} = \chi_m \mathbf{H} \tag{2.20}$$

where V is the volume. The magnetic field of a magnetic dipole is proportional to its magnetic dipole moment, and hence, we may write the magnetic flux density as,

$$\mathbf{B} = \mu_0(1 + \chi_m)\mathbf{H} = \mu_0\mu_r\mathbf{H} \tag{2.21}$$

The formation of a magnetic dipole moment results in a positive μ_e and higher flux density ($\mathbf{B}$) due to current (I) circulation in a closed loop. A capacitive coupling between conducting strips fabricated on a dielectric substrate leads to positive ε_e, resulting in positive n_e. An effective beam conversion can be achieved for higher positive values of n, making this cell structure suitable for beam-focusing applications.

2.5 Results and discussion

2.5.1 Simulation

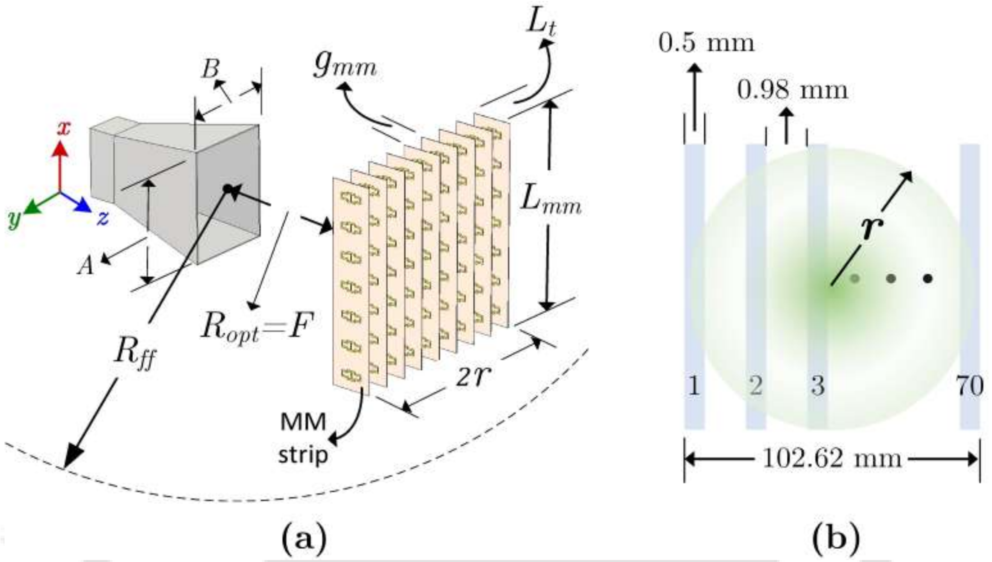

Figure 2.11: (a) Schematic for placement of MM array at an optimum distance from Tx horn and (b) schematic of proposed MM array as a GRIN lens.

The use of the proposed MM unit cell to improve the Tx antenna gain is studied and presented with field plots at the operating frequency. The array design method is described in [71], which shows a stack of fabricated strips that cover the horn aperture. The strip array's dimensions, gap, and placement are optimised to obtain focus. Figure 2.11 illustrates the arrangement of MM strips that form a GRIN lens of finite volume. An S-band horn antenna (Model: SL-5041/2568) is a transmitter exhibiting 9.43 dBi gain at 2.45 GHz. The dimensions A and B of the antenna are 142 mm and 105 mm, respectively, and thus the far-field of the antenna starts from $4.17\lambda_0 = 510$ mm.

Each MM strip contains 7 unit cells in the $x-$axis. The thickness of the strip is the same as the dielectric sheet, i.e. $h = 0.5$ mm. There are 70 strips stacked with a gap g_{mm} in $y-$axis. The distance between the MM array and antenna aperture R varies inside the far-field radius R_{ff} to obtain the maximum gain. The GRIN lens has cubic dimensions $L_{mm} \times 2r \times L_t$ of which $2r$ is a function of gap g_{mm}. With a reduction or increase in the gap, the array dimensions in $y-$axis get altered.

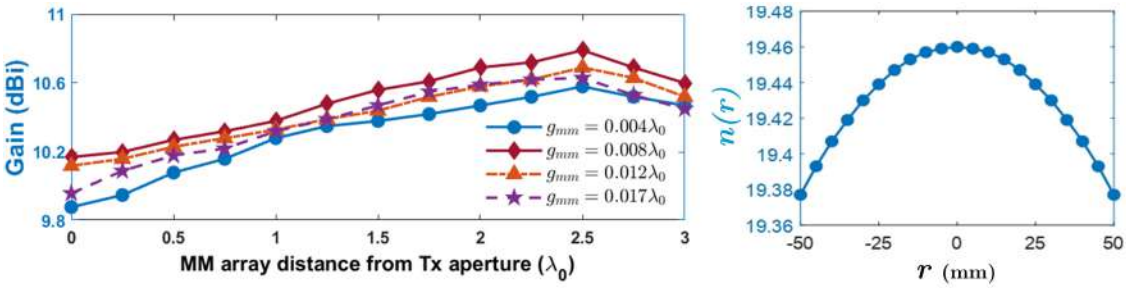

(a) (b)

Figure 2.12: Simulation variation of (a) gain with MM array placement distance from Tx aperture, (b) refractive index with radial distance r.

The arrangement shown in Figure 2.11a is electromagnetically modelled in CST. In the first step, $g_{mm} = 0.004\lambda_0$ is set and gain is calculated at every $0.25\lambda_0$ lens placement step from the Tx horn aperture. Figure 2.12a presents variation of gain with different array placements and four distinct g_{mm} values, namely $0.004\lambda_0$, $0.008\lambda_0$, $0.012\lambda_0$, and $0.017\lambda_0$ respectively. It is evident from Figure 2.12a that the gain approaches optimum when the array is placed at $R_{opt} = 2.5\lambda_0$. This stage produces maximum gain among all four values of the gap. At $g_{mm} = 0.008\lambda_0$, 10.79 dBi gain is observed and is higher than horn gain by 1.36 dBi at the same frequency.

Figure 2.11b show the physical array dimensions considering $h = 0.5$ mm and $g_{mm} = 0.98$ mm as concluded from 2.12a for $R_{opt} = 2.5\lambda_0$. A total of 70 strips measure 102.62 mm in $y-$axis. The array structure exhibits a radial distribution r with the centre at the lens mid-point, assuming planar geometry. For $r = 0$, the lens shows the highest n_e, reducing gradually as r extends towards the lens boundary. The GRIN distribution calculated from (2.3) is plotted in Figure 2.12b. Here, $n_{max} = 19.46$, $F = 2.5\lambda_0$, and $L_t = 48.98$ mm is considered. The array's diameter is 102.62 mm (as shown in Figure 2.11b); therefore, r varies between ± 50 mm. For $r = 0$, $n(r) = n_e = 19.46$ is obtained. This radial dense region offers low velocity to EM wave when propagating through the axis ($v = c/n$). At the corners, with $r = \pm 50$, $n(r) = 19.377$ is calculated. This parabolic gradual reduction offers effective beam focusing aimed at far-field WPT.

To check the polarisation property of the proposed GRIN MM lens, two types of simulation conditions have been set as depicted in Figure 2.13 and 2.14. An incident electric field orthogonal to the xoz plane makes yoz the principal E-plane. The 2D cross-section of the lens is shown in Figure 2.4 wherein the ray propagates through the slab. When subjected

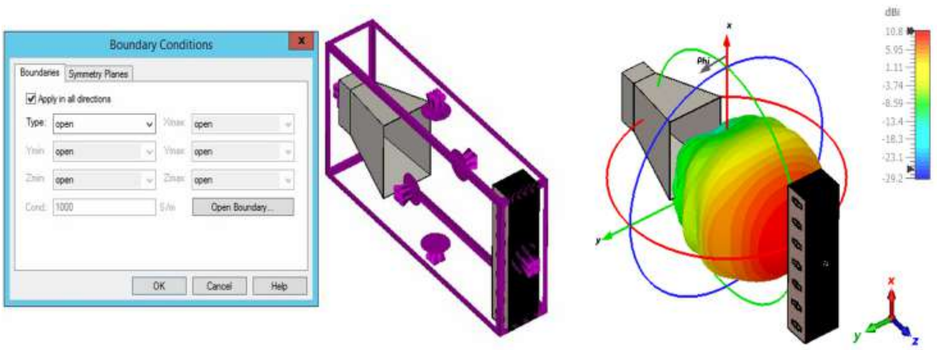

☑ Apply in all directions
Type: open
Xmax: open
Ymin: open
Ymax: open
Zmin: open
Zmax: open
Cond: 1000 S/m

Figure 2.13: Simulation boundary condition for MM array positioned vertically at $R_{opt} = 2.5\lambda_0$ and gain at 2.45 GHz.

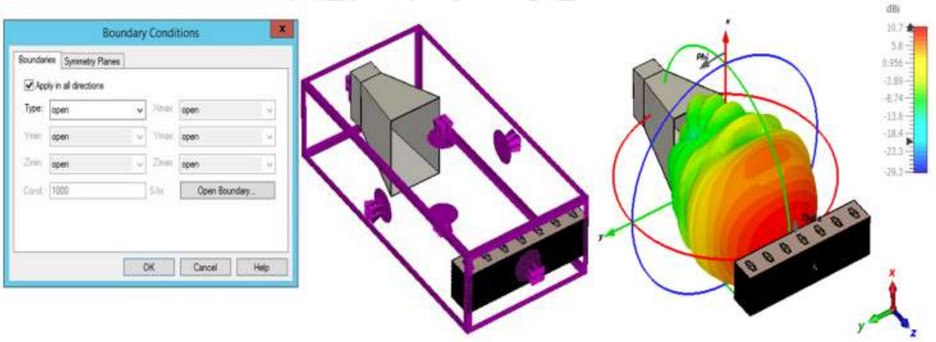

☑ Apply in all directions
Type: open
Xmax: open
Ymin: open
Ymax: open
Zmin: open
Zmax: open
Cond: 1000 S/m

Figure 2.14: Simulation boundary condition for MM array positioned horizontally at $R_{opt} = 2.5\lambda_0$ and gain at 2.45 GHz.

to the boundary condition as shown in Figure 2.13, the lens results in 10.79 dBi gain and is higher than typical horn for $1.25\lambda_0 \leq F \leq 2.75\lambda_0$. In the second case, the GRIN MM lens is aligned to the incident electric field as provided in Figure 2.5b. A Similar boundary condition for this case shows a 10.68 dBi gain and is approximately equal to the first case. Figure 2.13 and 2.14 depict the distribution of gain obtained from simulation at 2.45 GHz for both cases.

An array in the proposed work is a combination of MM strip length (L_{mm}), MM strip width ($W_{mm} = 2r$), and gap (g_{mm}) between each of them. The MM array structure acts as a lens by focusing the EM waves with cubic dimensions equal to $L_{mm} \times 2r \times L_t$ mm^3. An intuition for this can be made as a linearly polarised EM wave when propagating through the gap between MM strips; reflections from the conducting strips may result in non-zero values of other field components. The induced fields are in directions that satisfy unit cell boundary conditions as the cell's thickness is very small ($h \ll \lambda_0$). This shows a unique polarisation-independent property of the proposed GRIN MM lens that improves gain by focusing incident co- and cross-polarised field towards the Rx. The GRIN lens property maximises WPT efficiency when placed at the focus of the Tx antenna.

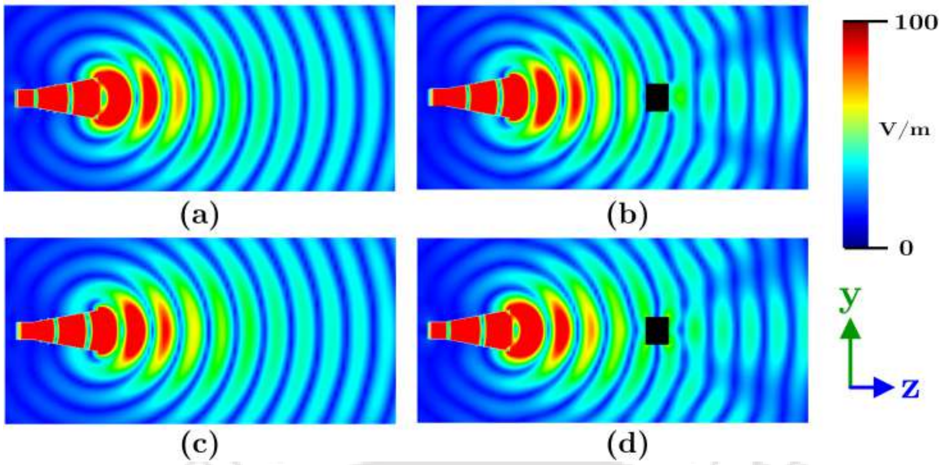

Figure 2.15: Electric field distribution in yoz plane at 2.45 GHz. (a) $\Re(\mathbf{E})$ without MM, (b) $\Re(\mathbf{E})$ with MM at R_{opt}, (c) $\Im(\mathbf{E})$ without MM, (b) $\Im(\mathbf{E})$ with MM at R_{opt}.

The distribution of simulated electric field (yoz) at 2.45 GHz is displayed in Figure 2.15. The real and imaginary parts are analysed to study the EM wave propagation. It shows with the inclusion of the GRIN lens at $R_{opt} = 2.5\lambda_0$, and the electric field follows the formation of a quasi-plane wave at its exit. Similarly, the magnetic field converges into a quasi-plane wave after passing through the lens. The power flow in E- and H-plane is depicted in Figure 2.16 shows pencil beam formation compared to a typical horn antenna of equal aperture.

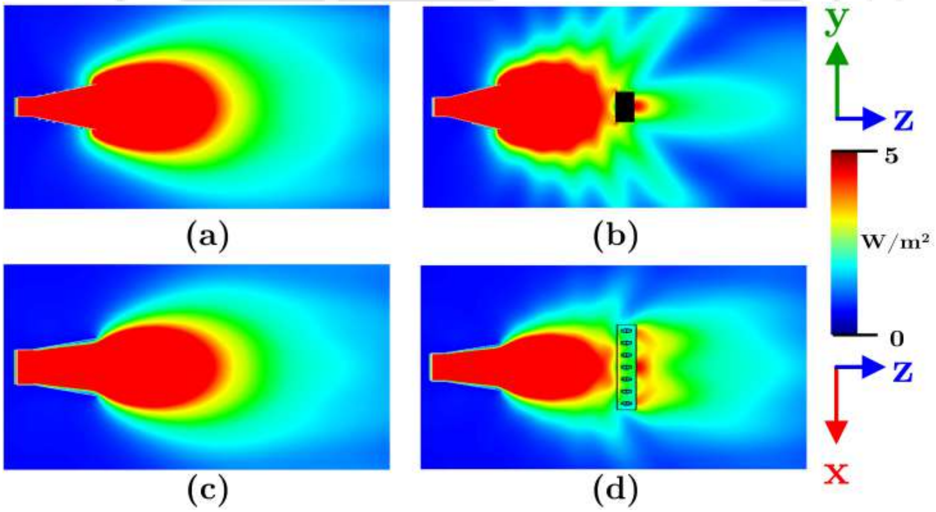

Figure 2.16: Distribution of power flow at 2.45 GHz. (a) Horn without MM, (b) horn with MM at R_{opt} in yoz plane. (c) Horn without MM, (d) horn with MM at R_{opt} in xoz plane.

2.5.2 Measurement

The proposed MM array strips are fabricated on a 0.5 mm thick Rogers RT5880 duroid substrate. The lens array is formed by attaching strips using double-sided adhesive tape. The tape is 1±0.15 mm thick and sticks appropriately on both sides. The radiation pattern is measured in an anechoic chamber by placing the lens at $2.5\lambda_0$ distance from the Tx aperture. The test antenna with MM lens is placed in far-field, and rotation is applied in distinct steps of 1.8°. The measurements use an Anritsu-made vector network analyzer (VNA) (Model: MS46122B).

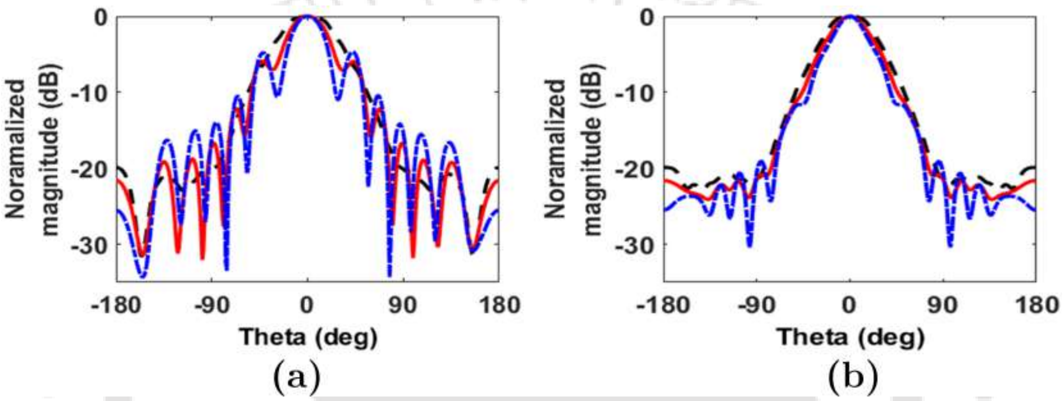

Figure 2.17: Simulated and measured radiation pattern at 2.45 GHz with proposed MM array at $R_{opt} = 2.5\lambda_0$ in (a) E- and (b) H-plane (dash: horn measurement, solid: horn+lens simulation, dash-dot: horn+lens measurement).

Figure 2.17 presents the radiation plots at 2.45 GHz in principle E- and H-plane. The horn has a wider beam spread between ±85° in the E-plane and ±65° in the H-plane, respectively. With the inclusion of an MM lens, the beam area is reduced significantly. This shows an increment in gain with power concentrated within a compact volume compared to horn only. The fabrication tolerances, positioning and alignment disturbances and connector losses give rise to side lobes in measurement plots. The power in sidelobe is used to charge the low-power devices [105], [106] simultaneously. The measured gain is 10.22 dBi, less than 0.57 dBi compared to the simulation. However, it exceeds the typical horn gain of 9.43 dBi at 2.45 GHz. This improved gain shall focus on optimum EM wave impinging on the array, thereby increasing the overall system efficiency. The half power beamwidth (HPBW) in E- is reduced to 43.6° from 60° on a measurement basis. Also, a reduction of 42° in the H-plane from 58° is observed, which shows that the MM GRIN lens concentrates the beam in a smaller area. Besides all the losses, the measurement results match well with the simulation.

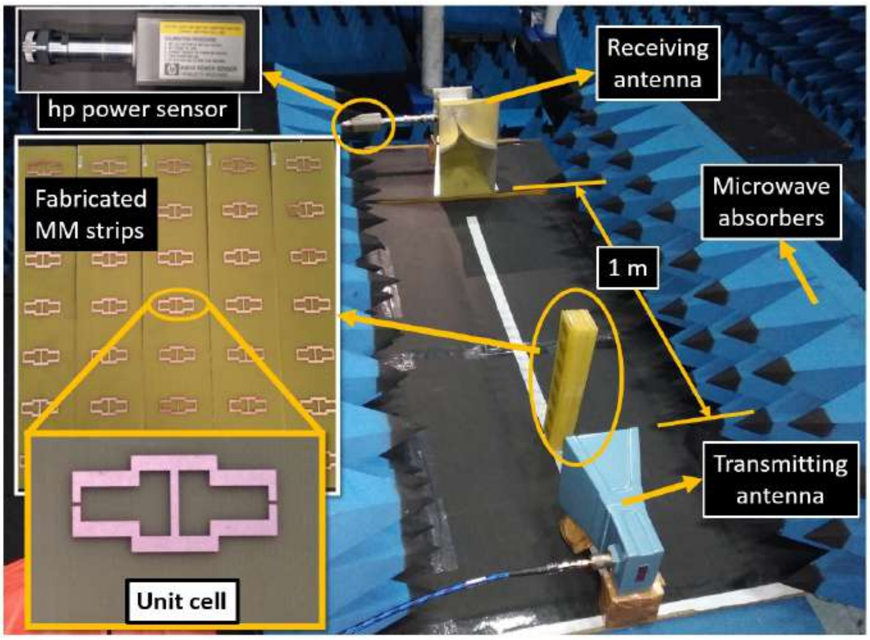

Figure 2.18: Experimental setup to measure far-field microwave WPT system efficiency at 1 m using proposed MM GRIN lens.

The feasibility study of WPT using MM is carried out in an anechoic chamber. Figure 2.18 shows the experimental setup for measuring Tx and Rx signals. At the Tx side, the horn antenna (SL-5041/2568) radiates the EM waves at 2.45 GHz. An RF signal generator (Make: Rhode & Schwarz, Model: SMB 100B) fed 30 dBm power to the horn. The Rx antenna placed at 1 m receives the power that incident in line-of-sight on its aperture. Here, a wideband ridged antenna (DRH-118) with 9.76 dBi gain at 2.45 GHz provides RF power to the hp 8481H (Make: Hewlett Packard) power sensor. The Agilent E4418B EPM series power meter displays the sensed power. The Tx-Rx assembly is placed onto a black wooden board to stay standstill, as depicted in Figure 2.18.

This arrangement provides the best line-of-sight alignment for optimum power transfer. Furthermore, microwave absorbers are kept on both sides to ensure best-suited experiment conditions. The antennas are kept at equal feed-point height, and a white line is drawn that guides the placement points of the MM GRIN lens. The inset of Figure 2.18 displays fabricated MM strips and a close view of a unit cell. The lens is placed in front of the Tx horn, and its placement distance is advanced in 13 steps. The points marked in the line are spaced $0.25\lambda_0$ and the starting edge of the MM lens is kept aligned at every point between $0 \leq R_{opt} \leq 3\lambda_0$. At each step, the signal generator supplies a 30 dBm RF signal ($f_0 = 2.45$ GHz), and power at 1 m is recorded on the power meter.

The relation between antenna gain, operating frequency, distance, and power is formulated in the Friis transmission equation in (1.3) for co-polarised Tx-Rx antenna reduces to,

$$P_r = P_t G_t G_r \left(\frac{\lambda}{4\pi R} \right)^2 \tag{2.22}$$

where $P_t = 30$ dBm, $G_t = 9.43$ dBi, $G_r = 9.76$ dBi, $R = 1$ m, and $\lambda = \lambda_0 = 122.45$ mm. In the absence of MM GRIN lens, (2.22) gives 8.97 dBm theoretically, and the power meter shows 8.1 dBm. This gives $\eta_{sys} = 26.91\%$ on a measurement basis when P_t is supplied. Figure 2.19 presents the variation of system efficiency η_{sys} with MM GRIN lens placement position from Tx aperture. The plot describes increment in η_{sys} for $0 \leq R_{opt} \leq 2.5\lambda_0$ and is maximum at $2.5\lambda_0$. As predicted in electromagnetic modelling, this behaviour suggests an application of MM as a lens for increasing the RF power.

For 30 dBm of input, this step results in 10.32 dBm and 9.78 dBm power on a theoretical and measurement basis. The discrepancy in the results is attributed to the connector, cable and other losses, including instrument noise, if any. A maximum value for $\eta_{sys} = 32.6\%$ is obtained and is higher than no MM case by 5.69%. It is also observed that for any placement value of R_{opt}, the measured power with MM lens is always greater compared to $\eta_{sys} = 26.91\%$. This demonstrates higher power delivery with an MM grin lens that can be scaled up for high-power transfer applications.

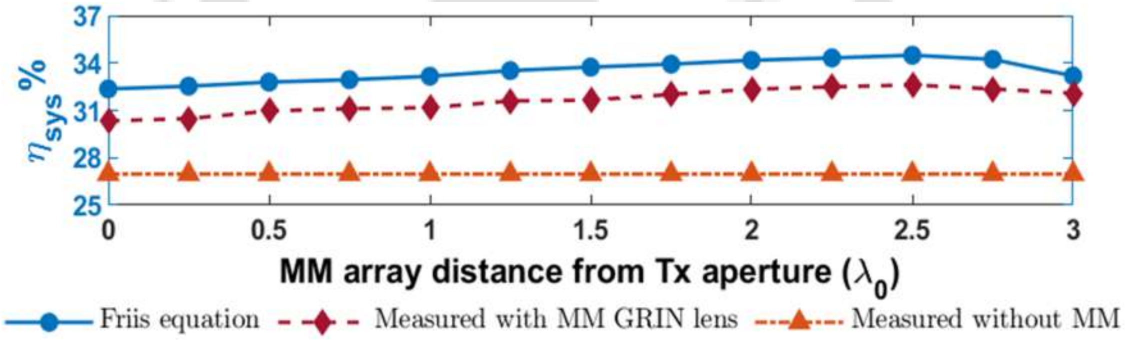

Figure 2.19: Variation of theoretical and measured η_{sys} with MM lens placement distance from Tx aperture.

Table 2.2 compares the proposed MM with earlier works based on size and system efficiency. Due to its geometrical simplicity, the suggested MM is shown to have the maximum efficiency and be the easiest to fabricate. The proposed MM unit cell has smaller dimensions than the described structures, even at higher frequencies and greater distances. It is a good choice for long WPT applications since the system efficiency (measured at 1 m) is superior to any previously published studies showing greater efficiency. Received power may be increased even more when used with the suggested MM and a high-power microwave source. Increased Rx distance, or the range for charging equipment like drones, aerostats, and robots, can be maximised.

Table 2.2: Comparison of the present study with other MM-based systems.

Ref	f_0	MM unit cell dimensions (mm^3)	Rx distance (mm)	η_{sys} with MM (%)
[30]	4 MHz	100×100×1	100	22
[88]	58.8 MHz	50×50×0.5	200	13.58
[89]	1.3 MHz	100×100×1.6	80	9
[90]	5.77 MHz	60×60×1	25	7
This work	2.45 GHz	48.98×37.35×0.5	1000	32.6

2.6 Summary

The 2.45 GHz far-field WPT system employing GRIN MM with an induced magnetic dipole is designed and experimentally proven for a 1 m distance. When the MM is positioned at $2.5\lambda_0$ from the Tx aperture, the power received is 9.78 dBm, yielding a system efficiency of 32.6%. The half-power beam widths are likewise decreased by 16 degrees on average in the principal planes to confine the beam efficiently. The suggested technique is most suited for long-range WPT applications with a high power source since system efficiency η_{sys} is always greater with the addition of MM than the system without MM.

This study creates a base formulation for efficiency-enhanced far-field WPT using Metamaterial as a GRIN lens *. The focusing property of the lens is utilised to improve the electric field in a rover charging application in the next chapter.

***Shashank. S. Kulkarni**, A. K. Baghel, and Sisir Kumar Nayak, "Graded Refractive Index Metamaterial for Enhanced Far-field Wireless Power Transfer Efficiency in S-band," AEU-Int. J. Electron. Comm., Volume 138, 2021, 153859, ISSN 1434-8411, https://doi.org/10.1016/j.aeue.2021.153859.

Chapter 3

Enhancement of electric field in far-field rover charging application using MM GRIN lens and reflector

---

Overview

This chapter presents enhancement in the electric field at the receiver side. Feasibility study of metamaterial incorporated far-field microwave WPT at 2.45 GHz. A schematic of the problem formulation for far-field rover charging is illustrated below. An MM array is used on the transmitting side for effective beam focusing. The rover has a payload and can accommodate lightweight and compact receiving antennas such as patches. An MM reflector array at the Rx side will improve the received power. A reduction in battery charging time can be achieved by including lightweight MM reflectors. The electric field measured with MM lens at Tx and MM reflector at Rx is doubled compared to a typical system without MM.

3.1 Introduction

A study to improve efficiency using the GRIN MM lens is presented in the previous chapter. The inclusion of the GRIN lens enhances the received power. The proposed methodology is used as a base formulation in this chapter, indicating the significance of MMs in microwave WPT applications, especially in high-power regimes. Wang *et al.* demonstrated beam focusing using Metamaterial (MM), which shows the capability of the MMs to be used in microwave WPT for optimum reception [107]. Microwaves are superior over large distances, offering optimal transfer to the receiver (Rx) side.

A far-field WPT technique allows the receiver to manoeuvre flexibly [27] as presented in [26], [34], [108] for maximising the received power using an array. A distributed microwave PT system with $P_t = 4.8$ W is presented in [109]. This system utilises 16 identical Tx antennas that are separated spatially. Besides the flexibility of movement, the antenna array is connected by physical wires, and supplying equal power to each element is crucial in practical realisation. The way of boosting overall system efficiency remains an unexplored research topic.

The logical choice for addressing the WPT to the rover is an MM lens and a reflector antenna constructed in this study. Metamaterials are employed as lenses and reflectors that concentrate the field at focus, preserving the present system's physique. Three-dimensional gradient refractive index (GRIN) MMs offer better beam shaping capabilities than planar lenses [92] and are presented in [65], [110] - [113].

The refractive index of a three-layer MM unit cell constructed for $f_0 = 10$ GHz described in [65] varies from 1.5 to 6.26. The core layer sandwiched between the two impedance match layers results in 66% impedance bandwidth between 7.2 and 13.4 GHz. In[110], a planar wavefront transformation lens based on isotropic and inhomogeneous MMs is described with a 57 mm thick 19-layer lens that operates between $8-12$ GHz. For $f_0 = 13.4$ GHz, a strategy to create a single element lens described in [111] provides two configurations with equal lens diameters of 112 mm. The lens is 210 mm thick for operational and 40 mm thick for collapsed arrangement. The multi-layer GRIN lens in [112] is 17 mm thick and attains beam steering when the feed horn location is mechanically modified. This demonstrates MM's ability to manipulate EM waves to achieve the desired pattern.

The literature shows the advantages of MM-based WPT for versatile applications with significant bandwidth capabilities. Nevertheless, this study attempts to enhance the electric field in far-field microwave WPT at a constant frequency ($f_0 = 2.45$ GHz) for rover charging applications. The MM GRIN lens presented in [71], improves WPT overall system efficiency for 6 meters and 1-meter far-field separation distance, respectively. The MM unit cell exhibits a magnetic dipole at the operating frequency and offers the least input reflection to the Tx horn antenna when placed at the focus. The GRIN array shows parabolic refractive index (RI) distribution, resulting in a focused field in the main direction.

Maximum power extraction is crucial as EM waves radiated by Tx antenna face various disturbances that include free space path loss, absorption and reflections from undesired directions and also non-ideal Tx-Rx apertures and field distributions [114]. A higher electric field concentrated at focus improves received power since $S_z = \mathbf{E}_x \cdot \mathbf{H}_y = |\mathbf{E}_x|^2/\eta$ where η is the intrinsic impedance of the medium. Therefore, for increasing the power reception at the Rx side, MM reflectors [79]- [81] that focus incident waves are a natural choice.

This chapter presents a methodology of utilising the MM GRIN lens at the Tx and MM reflector array for electric field enhancement aimed at far-field WPT in the microwave regime. The next section presents the problem formulation for far-field rover charging at 3 meters. The Tx design section explains the proposed MM GRIN lens's design, fabrication, and testing. The Rx design section presents MM reflector design, simulation, and testing. The results of experimental case studies are discussed in the results section, followed by conclusions in the final section.

3.2 Problem formulation

This chapter examines the performance improvement of a far-field WPT system for powering a battery-operated rover. Figure 3.1 illustrates the schematic for problem formulation wherein a rover is being charged via a 2.45 GHz microwave signal captured by a reflector antenna mounted on its top. Various sensors, viz. temperature, humidity, etc., are mounted on its chassis for accurate and responsive measurements. The rover also has a camera that captures real-time pictures and videos. The rover has a self-guiding system, and the data collected by the sensors while performing the task is relayed back to the control station.

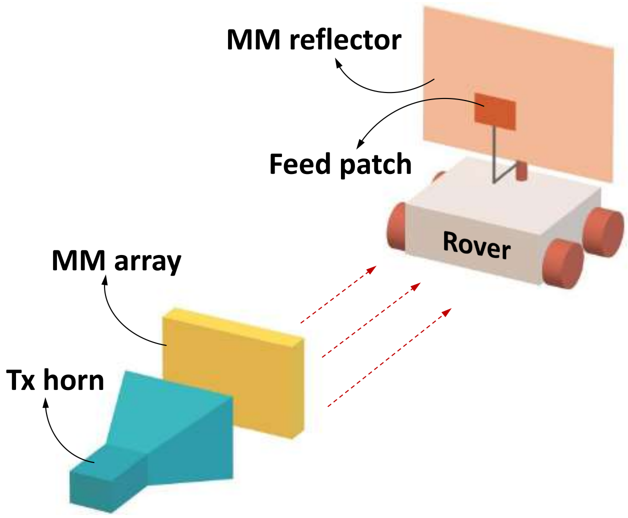

Figure 3.1: Illustration of the problem formulation for WPT to rover using GRIN MM lens and MM reflector.

The battery provides enough backup for a fixed time to carry out the tasks/missions. This reduces the area covered, and the mission path is limited for practically big expeditions. Recharging the battery would be inconvenient as the rover has to return and be charged. WPT is perfectly suitable to supply charge when the rover runs out of battery. The location of the Tx antenna (power station) is established so that the rover can communicate with the power station autonomously when it needs to charge. It's anticipated that dedicated antennas mounted on the rover chassis handle communication and power receiving independently. For simplicity, only the power reception (Rx) patch is shown in the schematic. An MM GRIN lens on the Tx side focuses the EM field effectively towards the MM reflector installed onto an Rx rover at $R = 3$ meters. In future, the MM reflector array and feed patch system can be extended for simultaneous wireless information and power transfer (SWIPT) applications [105].

3.3 Transmitter design

The horn used in the base study is best suited for low-power applications and standard radiation properties measurements in S-band. A high power microwave source in [71] use Tx horn of aperture $A(= 4.13\lambda_0) \times B(= 3.33\lambda_0)$ mm^2 where $\lambda_0 = 122.45$ mm. This large physical size makes the system bulky and difficult to be carried over a mobile platform. As a result, for high-power analyses, a pyramidal horn antenna with an aperture size of

$A = 1.33\lambda_0$, $B = 1\lambda_0$, and a feed waveguide size of 86.36×43.18 mm^2 at the transmitting side is adopted. The waveguide port horn is justified to carry out the high power studies when attached to a magnetron to the waveguide launcher. The waveguide components exhibit a large power handling capacity perfectly suitable for WPT applications.

3.3.1 Design and analysis

MM GRIN lens unit cell

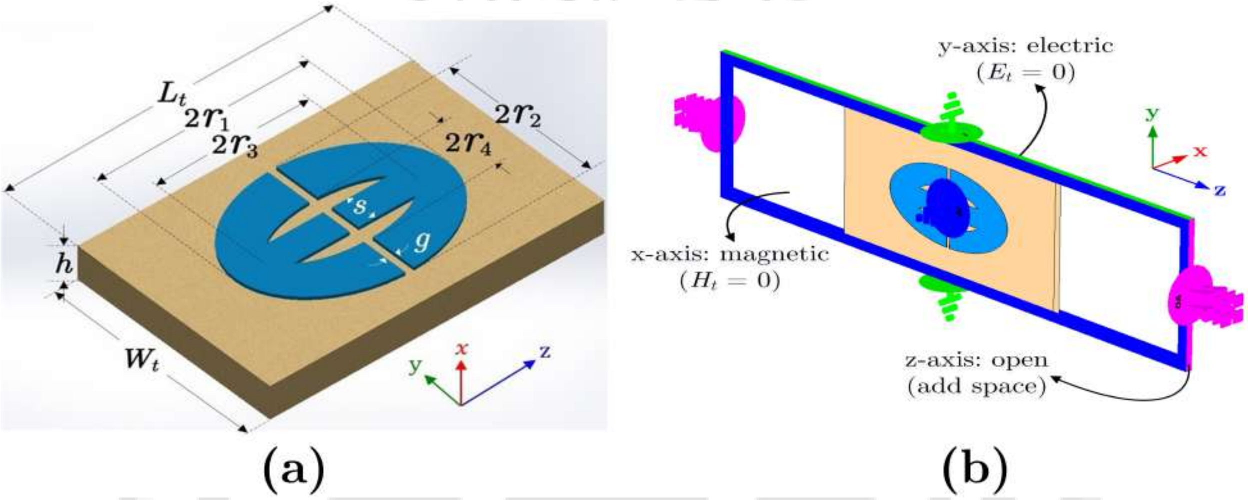

Figure 3.2: (a) Geometry of the proposed MM unit cell designed on $h = 0.01\lambda_0$ thick FR4 substrate. (b) Simulation boundary conditions in CST.

Figure 3.2a illustrates the geometry of the proposed MM unit cell. It is designed on FR4 substrate with $\varepsilon_r = 4.3$ and copper thickness $t = 35$ μm. The dielectric substrate used in the previous study requires a large cost for fabrication. Therefore, a cheaper FR4 substrate is considered in this chapter. The GRIN MM lens at the Tx side and the MM reflector at the Rx side are designed on the FR4 sheet. This reduced the system fabrication cost and showed considerable improvement over Rogers substrate. The cubic dimensions of the unit cell are $L_t \times W_t \times h$ mm^3 that is optimised for the operating frequency $f_0 = 2.45$ GHz.

An elliptical ring is designed by subtracting minor ellipse ($r_1 : r_2 = 1 : 1.93$) from a major ellipse ($r_3 : r_4 = 1 : 2.24$) centred at the substrate centre. A rectangular strip of width s along $z-$ and length $2r_1$ along $y-$axis is added to the elliptical ring that forms a closed structure. Etching a rectangular strip of length $2r_2$ and width g creates a gap, and the structure forms a complementary ϵ spaced g apart. The major radii are considered along the direction of propagation, i.e. $z-$axis. Table 3.1 shows dimensions of cell parameters in mm and respective λ_0.

Table 3.1: Unit cell parameters optimised for $f_0 = 2.45$ GHz

parameter	value (λ_0)	value (mm)	parameter	value (λ_0)	value (mm)
r_1	0.114	13.95	g	0.005	0.6
r_2	0.059	7.22	s	0.029	3.55
r_3	0.065	7.96	L_t	0.408	50
r_4	0.029	3.55	W_t	0.22	27

The unit cell is electromagnetically modelled by providing a y-polarised excitation in commercial electromagnetic solver CST Studio suite for the frequency range 2−2.9 GHz. Figure 3.2b depicts boundary conditions in the simulation environment. The performance at the operating frequency is optimised by refining its physical parameters. The transmission (T), reflection (R), and absorbance (A) are computed using S-parameters by $T = |S_{21}|^2$, $R = |S_{11}|^2$, and $A = 1 - T - R$. The T, R, and A responses within the simulation bandwidth are plotted in Figure 3.3a. It shows resonance with the highest $T = 0.839$, lowest $R = 0.001$, and $A = 0.16$ at 2.45 GHz. The absorption occurs due to non-ideal conductance and impurities in practical conductors. Also, the inductance of thin strips exhibits an internal resistance representing ohmic and thermal losses at the resonance. The presence of non-ideal material properties results in $A = 0.16$.

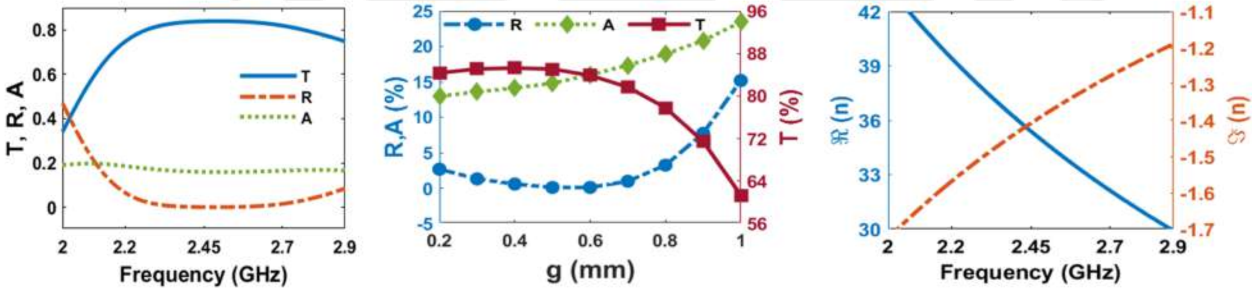

(a) (b) (c)

Figure 3.3: (a) Simulation variation of T, R, A for unit cell optimum dimensions with frequency. (b) Variation of T, R, A for different values of g. (c) Extracted complex refractive index with frequency.

The fundamental goals of these unit cell designs are to produce a precisely matched transmission coefficient and minimum phase fluctuations at constant f_{op}. The variation of T, R, A for $0.2 \leq g \leq 1$ mm are displayed in Figure 3.3b. It is noted that the gap $g = 0.6$ mm results in 83.89%, 0.11% of T, and A, respectively. The medium parameters are affected by a small change or deviation in conducting strips' physical length and width. A smaller (or larger) gap value would reduce (or increase) the effectiveness. The resized metallic area and the gap between the strips constitute inductance and capacitance and thus modify the resonant frequency as the surface area and length of the conductor are changed, as illustrated in Figure 2.7.

The complex scattering parameters are used in the retrieval method for n [103] and hence produce complex values for n in relation to the unit cell thickness [111]. Figure 3.3c shows the variation of n in the simulation band, and $n = 35.398 - j1.435$ is obtained at 2.45 GHz, with a reduction in T above 2.45 GHz, n exhibits lower values of real and imaginary parts. MMs are demonstrated as a wideband GRIN lens [65], [69], [111], wherein the refractive index shows resonating behaviour with the maximum $\Re(n)$ and minimum $\Im(n)$ within the simulation band. A higher value of n helps in effective beam conversion; therefore, an array with the proposed MM unit cell is considered for studying electric field advancement.

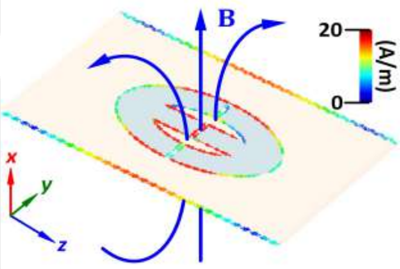

Figure 3.4: Simulation distribution of surface currents on MM unit cell at 2.45 GHz.

The currents are concentrated in the outer part of the metal area, as seen in the surface current distribution in Figure 3.4. It is evident from Figure 3.3b that a change in constructional dimensions alters the transmission response. The dominant values of rectangular strip width s and gap g between them correlate to the surface current forming a loop on the inner and outer walls of the cell. This results in a magnetic dipole with induced field $\mathbf{B}$ as shown in Figure 3.4. The magnetic field by a magnetic dipole moment is $\chi_m \mathbf{H} = \mathbf{M} = \mathbf{m}/V = IS\mathbf{a}_n/V$. The increment in magnetisation ($\mathbf{M}$) is the result of an increment in current (I) as the S/V ratio is constant. This leads to higher values of induced flux density $\mathbf{B}$ due to the circulating loop current I in the MM unit cell. The capacitance between the metal strips and the dielectric substrate gives an overall positive value of n used for GRIN lens design.

MM GRIN lens array

The GRIN lens array is formed by joining the MM strips and spacing the optimum gap apart, as discussed in Section 2.5.1. The focus estimation is carried out by performing simulations to position the lens in front of the Tx horn accurately. An identical approach is examined wherein the schematic for obtaining maximum gain is shown in Figure 3.5a. In electromagnetic modelling, the Tx horn has 11.3 dBi gain at 2.45 GHz when excited using waveguide port input. Given the Tx horn's aperture size, a strip containing 11 unit cells in the $y-$axis with physical dimensions of $297 \times 50 \times 1.2$ mm^3 is made. A single strip has a length almost 2.5 times the antenna flaring length in an E-plane.

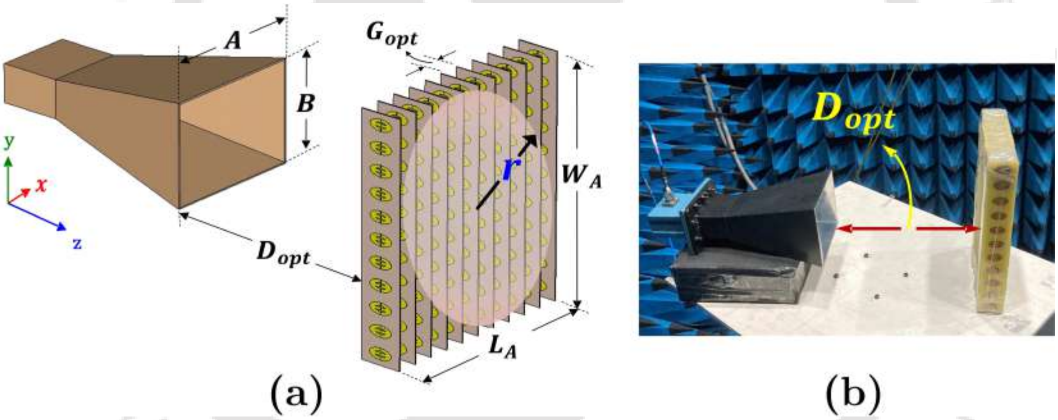

Figure 3.5: (a) Schematic for obtaining optimum MM array placement distance from Tx horn aperture and (b) fabricated GRIN MM array placed at D_{opt} from Tx horn antenna.

The beam area of an EM wave radiated by the point source, i.e. phase centre of the horn, depends on flaring angle, flare length and aperture size [57]. A unit strip of length $W_A = 2.425\lambda_0$ achieves a maximum incidence of the electric field. Lowering the strip length will reduce field interaction, and increasing it shall make the system bulkier and more complex for arrangement. Aperture length in the H-plane is covered by 91 strips in the $x-$axis with the gap G_{opt} between them. This MM array forms a GRIN lens that focuses power towards Rx. These strips cover the entire horn aperture for $0.01\lambda_0 \leq G_{opt} \leq 0.04\lambda_0$ and are practically realisable for fabrication. In the inset of Figure 3.5b, a fabricated array spaced at D_{opt} from the Tx horn antenna is shown.

Simulation variation of gain for distinct MM array placement distance values from Tx horn aperture is shown in Figure 3.6a. The gap G_{opt} is refined to achieve maximum gain by performing simulation at $0.125\lambda_0$ step for array placement between $1.75\lambda_0$ and $2.5\lambda_0$. A optimum value of 14.8 dBi gain is observed at $D_{opt} = 2.25\lambda_0$ and $G_{opt} = 0.02\lambda_0$. The gain observed is 3.5 dBi greater than a typical horn at the same frequency. The array dimensions $L_A \times W_A \times L_t (= T)$ constitute the GRIN medium with $n = n_{max}$ at the centre and gradual reduction towards lens boundaries when r is increased as formulated in (2.6). The variation of n for the MM GRIN medium between $-150 \leq r \leq 150$ is plotted in Figure 3.6b. Here, $F = 2.25\lambda_0$, $T = 0.408\lambda_0$ and $r = \pm 1.22\lambda_0$ are used which shows a gradual reduction. The variation of $n(r)$ results $n(0) = 35.398$ and $n(\pm 1.22\lambda_0) = 33.057$ at the center and lens boundary respectively.

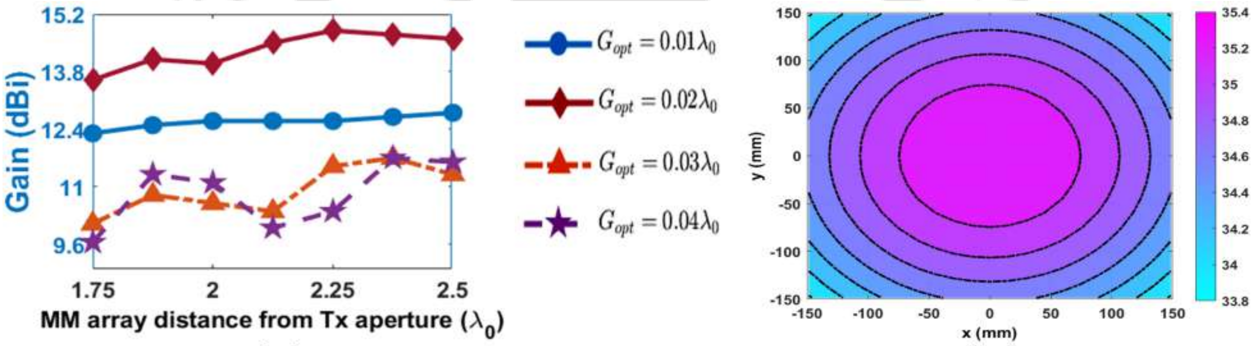

(a) (b)

Figure 3.6: Simulation variation of gain at 2.45 GHz with MM array placement distance from horn aperture for different values of strip gap G_{opt}.

The antenna-radiated fields undergo reflections at the near-field boundary, defined by the physical dimensions of the antenna. Therefore, positioning the MM GRIN lens with a surface area approximately twice the aperture area is a point of study. A 3D simulation gain distribution of a typical horn antenna at 2.45 GHz is displayed in Figure 3.7a. In general, the antenna gain is a function of frequency and physical aperture, related as $G = 4\pi A_e/\lambda^2$, where A_e is the electrical aperture. It shows that increasing the aperture area at a constant frequency results in high gain values. To do so, the flaring angle can be increased, but it results in an open-ended waveguide when it approaches 90°. Also, the flaring length increment in the E- and H-plane shall result in a very large antenna aperture, which is difficult for practical realisation.

Therefore, when positioned in proper alignment with respect to the incident field, the

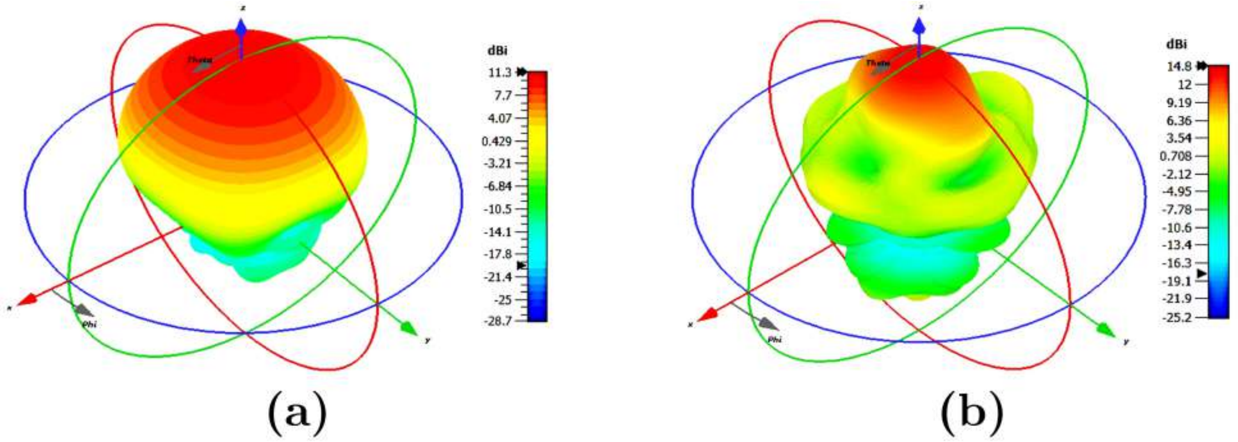

Figure 3.7: 3D Simulation gain distribution at 2.45 GHz. (a) Horn antenna without MM and (b) horn antenna with MM at $D_{opt} = 2.5\lambda_0$.

MM array will result in higher values. The physical aperture size of the horn is constant, and with the inclusion of the GRIN MM lens, the equivalent electrical aperture is increased. A 3D simulation distribution of gain at 2.45 GHz for GRIN MM lens positioned at D_{opt} is depicted in Figure 3.7b. It is observed that the distribution shows sidelobes in both planes. In practical applications, the field in sidelobes can also be used to charge batteries of small systems such as sensors or ultra-low power element-based IoT [105], [106]. When located at a sidelobe angle, these systems will receive power and are very useful in simultaneously powering multiple devices.

Figure 3.8 displays the radiation in principal directions and the simulated gain plots for four distinct D_{opt} values with $G_{opt} = 0.02\lambda_0$. It illustrates dominant power concentration in the main lobe for all cases. The MM GRIN lens separates the beam and has low HPBW values in corresponding planes for $D_{opt} = 2.25\lambda_0$, producing symmetrical power distribution. As the gap increases or decreases, the gain reduces with a considerable rise in sidelobe levels (SLLs). However, these focal points also produce a balanced radiation distribution in the E- and H- planes. It should be noted that all focus values may also apply in cases when the SLLs need a substantial amount of power for simultaneous reception.

Fields radiated by the antenna are three-dimensional in space and are concluded from gain distribution as shown in Figure 3.7. For analyses, the field in principal E- and H-plane at 2.45 GHz is depicted in Figure 3.9. The field propagates continuously as the phase is varied between 0 and 2π. An effective beam focusing and conversion to quasi-plane wave is observed from Figure 3.9b and 3.9d. A typical horn antenna radiates spherical waves in the

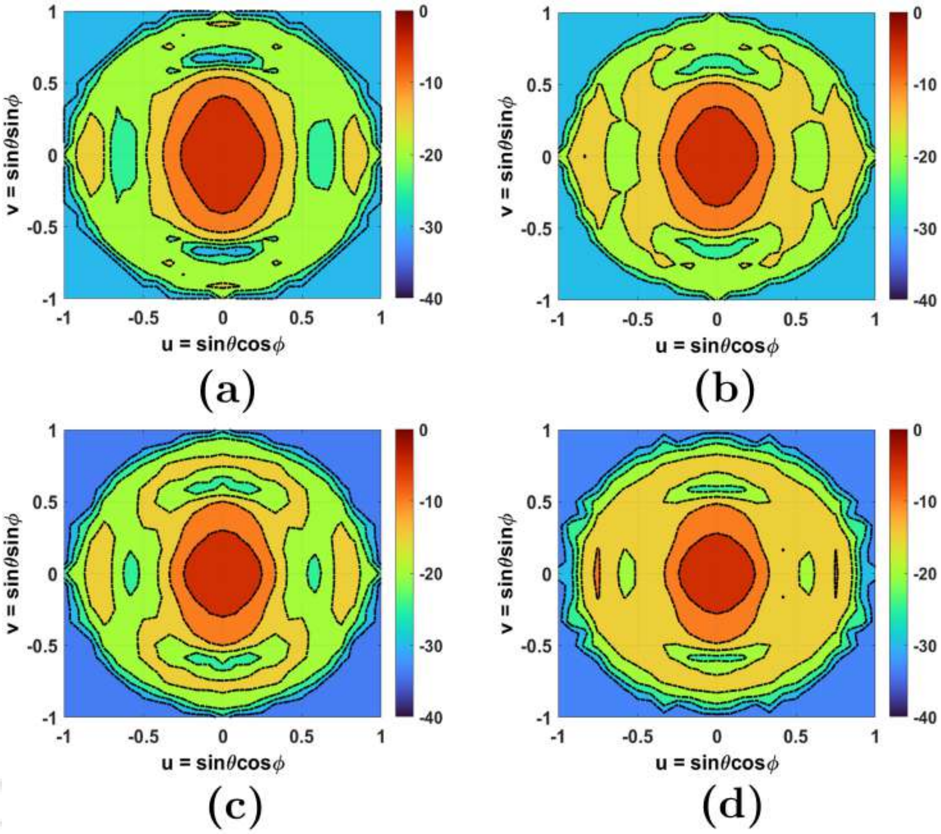

Figure 3.8: Distribution of gain for $0 \leq \phi \leq 2\pi$, $0 \leq \theta \leq \pi/2$ with MM GRIN lens at D_{opt}. (a) $D_{opt} = 1.75\lambda_0$, (b) $D_{opt} = 2\lambda_0$, (c) $D_{opt} = 2.25\lambda_0$, and (d) $D_{opt} = 2.5\lambda_0$.

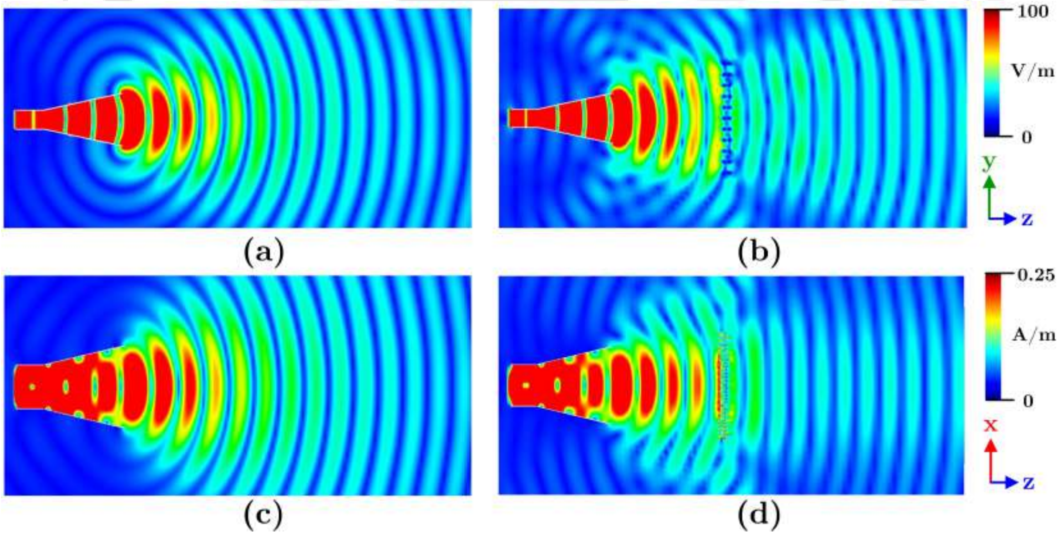

Figure 3.9: Field distribution (a) electric field without and (b) with MM at D_{opt} in *yoz* plane, (c) magnetic field without and (d) with MM at D_{opt} in *xoz* plane at 2.45 GHz.

yoz plane and is merely converted to plane waves. The field distribution shows a considerable increment in beam conversion ideally suited for far-field power transfer. It is also noted that the magnetic field in the *xoz* plane has a confined area in the direction of propagation as shown in Figure 3.9b,d. The beam width is significantly reduced as EM waves propagate through an array. Figure 3.10 illustrates the simulation distribution of power flow principal planes. The beam focusing along the $z-$axis is considerably achieved compared to a typical horn as it advances through the GRIN lens positioned at focus.

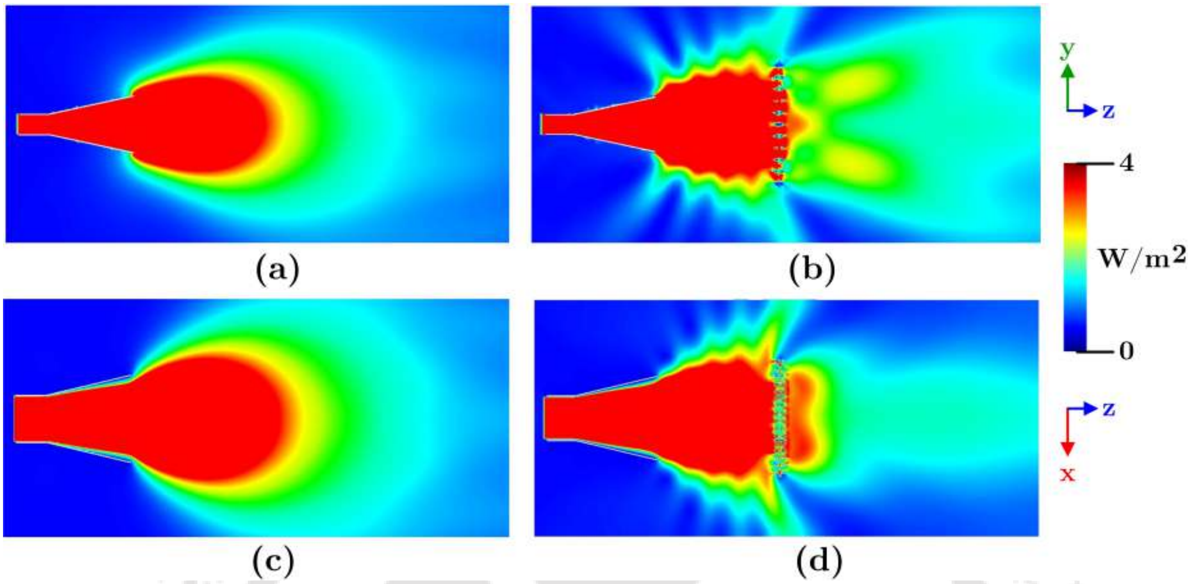

Figure 3.10: Distribution of power flow at 2.45 GHz. (a) a horn without MM, (b) Horn with MM at D_{opt} in yoz plane. (c) A horn without MM, and (d) horn with MM at D_{opt} in xoz plane.

When the EM field impinges on the MM GRIN array, it undergoes reflections due to non-ideal substrate and conductor properties. Also, the practical volume of the inhomogeneous MM GRIN lens gives rise to reflections in multiple directions at the edges. The electric field distribution in xoy plane cut at the lens middle is plotted in Figure 3.11. It is noted that the field is concentrated at the middle part and distributes radially as phase increases from 30°. The gradient of n as shown in Figure 3.6b offers a sufficient difference in RI of centre and edge that leads to conversion to planar wave.

Figure 3.12 presents the forward propagation of the EM wave in the xoz plane. A part of the beam deflected from edges emerges as sidelobes at equal angles. The wave impinging on the array changes velocity inside the finite thickness. At the center, velocity is $v = c/n_{max}$ that increases gradually to $v = c/n_{(\pm 1.22\lambda_0)}$ where c is the velocity of light. Notably, the spherical wavefront at 0° emerged as planar at 150°, indicating a focused beam for long-range effective WPT. In future, in simultaneous wireless information and power transfer (SWIPT) applications, the field at the sidelobe angle can simultaneously provide power to secondary IoT systems.

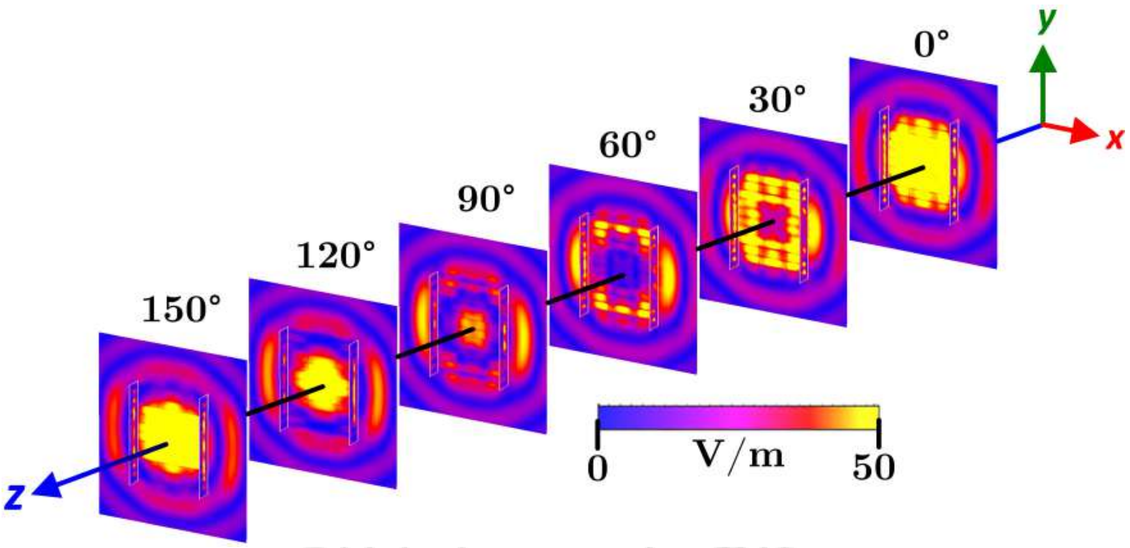

Figure 3.11: Simulation distribution of electric field on the MM GRIN lens cross-sectional plane when placed at $D_{opt} = 2.25\lambda_0$ at 2.45 GHz.

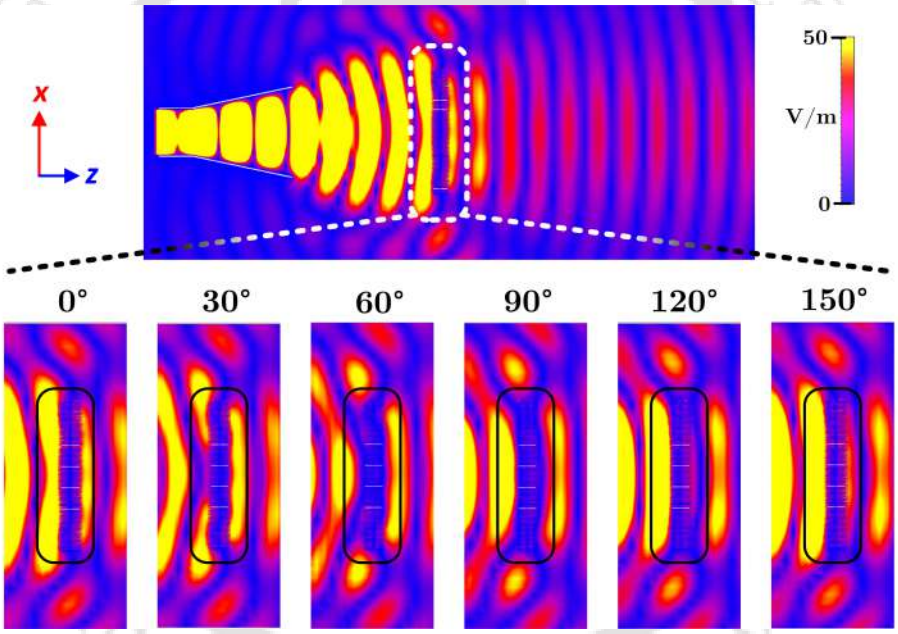

Figure 3.12: Propagation of EM wave through proposed MM GRIN lens positioned at D_{opt} in xoz plane.

3.3.2 Fabrication and measurement

91 MM strips were fabricated on a 1.2 mm thick dielectric sheet. Figure 3.13a,b illustrates strips and close view, respectively. The designed MM strips were secured using double-sided tape of 2.4 mm thickness. The tape is affixed to both ends' outer edges to create an air gap of G_{opt} between array strips. A transparent tape is applied at the top and bottom, ensuring the array stays in place. As shown in the inset of Figure 3.13c, the MM array is positioned at D_{opt} from the horn aperture, and a laser pointer is used to ensure that the array

is appropriately positioned to cover the horn aperture equally. The radiation characteristics are measured in an anechoic chamber using Anritsu-made VNA (Model: MS46122B).

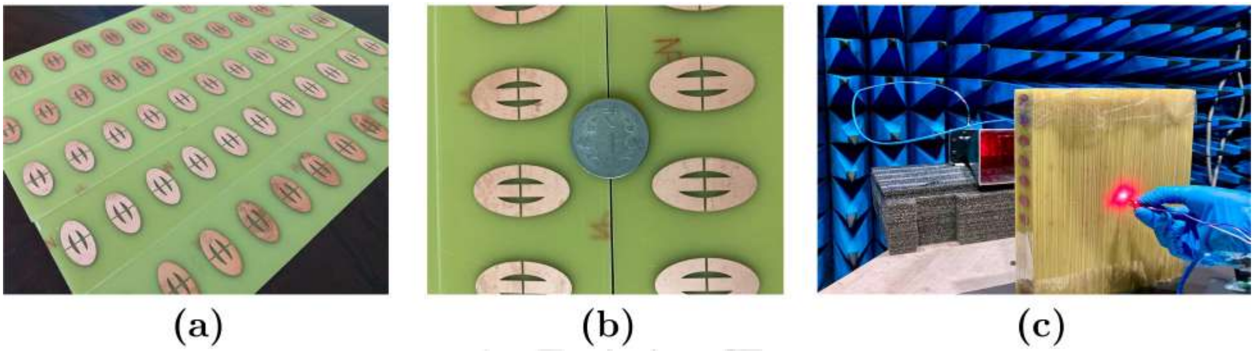
(a) (b) (c)

Figure 3.13: (a) Fabricated MM strips, (b) a close view of the unit cell, and (c) MM lens alignment at R_{opt}.

The arrangement of Tx horn and MM GRIN lens inside an anechoic chamber for measurement of the radiation pattern in E- and H-plane is presented in Figure 3.14a and b respectively. The test antenna has a 9.43 dBi gain of 2.45 GHz and is the same as used in Chapter 2. Both the antennas are placed at a far-field distance with respect to their physical dimensions, and a rotation of 360° is applied in each arranged measurement.

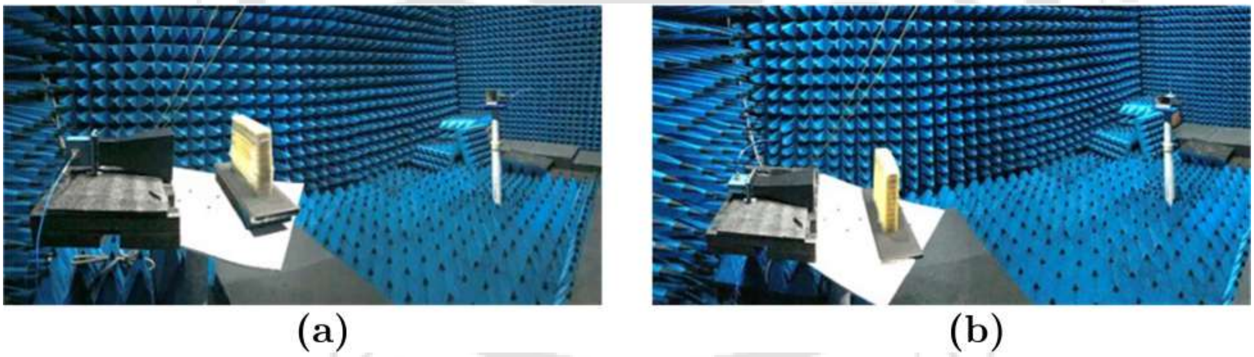
(a) (b)

Figure 3.14: Experimental arrangement for radiation pattern measurement in an anechoic chamber. (a) E- and (b) H-plane.

Figure 3.15 describes the variation of magnitude for various values of theta in E- and H-plane, respectively, at 2.45 GHz. It is evident from the figure that the measured results match well with the simulated. Radiation in the main lobe and other consecutive lobes follows a similar pattern as simulation. The slight shift and increased lobe magnitude are attributed to the placement tolerances of the MM array in front of the horn. Although rays reach the lens at oblique angles and with multiple polarisations, the conventional electromagnetic parameter retrieval approach for unit cell and array design examines only regularly incident waves. The measured radiation pattern is close to the simulation results despite the simplifications.

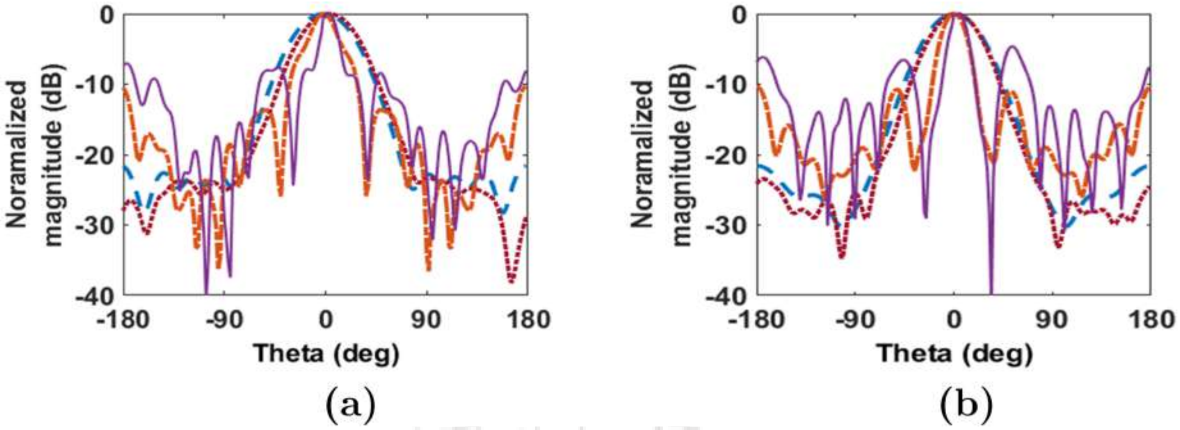

Figure 3.15: Simulated and measured radiation pattern at 2.45 GHz for horn and horn with proposed MM array in (a) E- and (b) H-plane (solid, violet: MM GRIN lens simulation; dash-dot, orange: MM GRIN lens measurement; dot, brown: horn sim; dash, blue: horn mes).

3.4 Receiver design

This section presents the design of the MM reflector at the receiver side. A typical patch antenna with 3.16 dBi simulation gain at 2.45 GHz is used as feed for the reflector. The choice of the patch antenna is justified as the receiver side circuitry possesses low weight to be installed on a mobile rover. Also, the patch antenna exhibits simple geometry, low cost, and ease of fabrication, thus being most suitable for the reflector feed. This section investigates the design and analysis of the MM reflector unit cell and fabricated array based on electromagnetic modelling and measuring the radiation properties at the operating frequency.

3.4.1 Design and analysis

MM reflector unit cell

The geometry of the proposed unit cell is shown in Figure 3.16a. The side length is assigned as L_r along $y-$ and width W_r along $x-$ axis at the centre working frequency $f_o = 2.45$ GHz, and the total thickness h is set to 0.8 mm. An FR4 sheet with $\varepsilon_r = 4.3$ and 35μm copper thickness is used as a base. At first, a rectangular ring of length m_a along $x-$ and width m_b along $y-$axis is made with strip width m_s. A gap of width m_g is etched at both ends, and

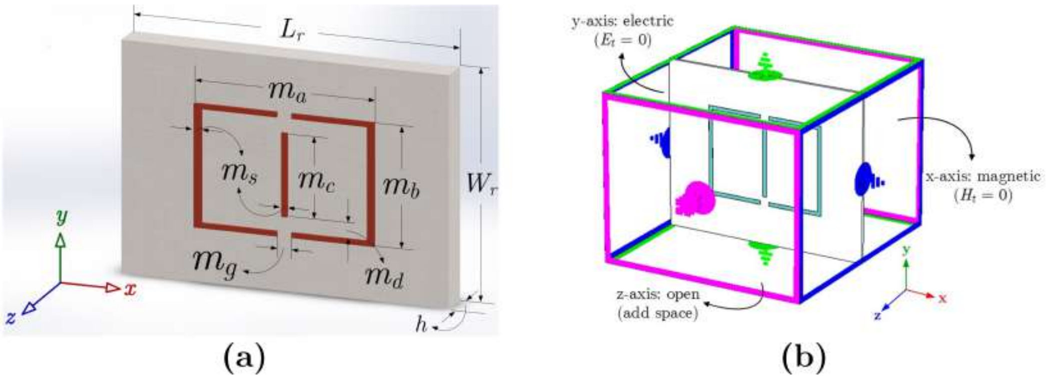

Figure 3.16: (a) Geometry of the proposed MM reflector unit cell designed on $h = 0.006\lambda_0$ thick FR4 substrate. (b) Simulation boundary condition in CST.

a rectangular strip of length m_c and width m_s is created at the centre of the unit cell. The optimised dimensions for $f_0 = 2.45$ GHz are tabulated in Table 3.2.

Table 3.2: Unit cell parameters optimised for $f_0 = 2.45$ GHz

parameter	value (λ_0)	value (mm)	parameter	value (λ_0)	value (mm)
m_a	0.114	13.95	m_g	0.005	0.6
m_b	0.059	7.22	m_s	0.029	3.55
m_c	0.065	7.96	L_r	0.408	50
m_d	0.029	3.55	W_r	0.22	27

The unit cell is electromagnetically modelled in CST, and the electric field parallel to $y-$axis is assumed as depicted in Figure 3.16b. The direction of the electric and magnetic fields are assumed to be identical to MM lens excitation, i.e. electric field along $y-$ and magnetic field along $x-$axis, respectively. Variation of T, R, and A with frequency is depicted in Figure 3.17a. The parameters $T = 0.004$, $R = 0.879$, and $A = 0.117$ are observed to show near-perfect reflection at the operating frequency. To optimise the performance, the strip width m_s is tuned between $0.6 \leq m_S \leq 1.4$ mm. The variations of T, R, and A for the same are shown in Figure 3.17b. The observed reflection is 87.93% and shows clear resonance at 2.45 GHz, where the transmission is almost zero and absorbance is close to 11.6%.

The exotic reflection capability of MM are extensively studied in [79]- [83]. The geometrical complexity in [80] and tedious fabrication and alignment processes [82], [83] are crucial benchmarks, especially for mobile applications. As evident from plots in Figure 3.17b, small variations in constructional parameters significantly change the phase response. Therefore, symmetry in the xoy plane simplifies fabrication using conventional PCB fabrication techniques. The manufacturing of conventional phase-changing MM reflector arrays reported

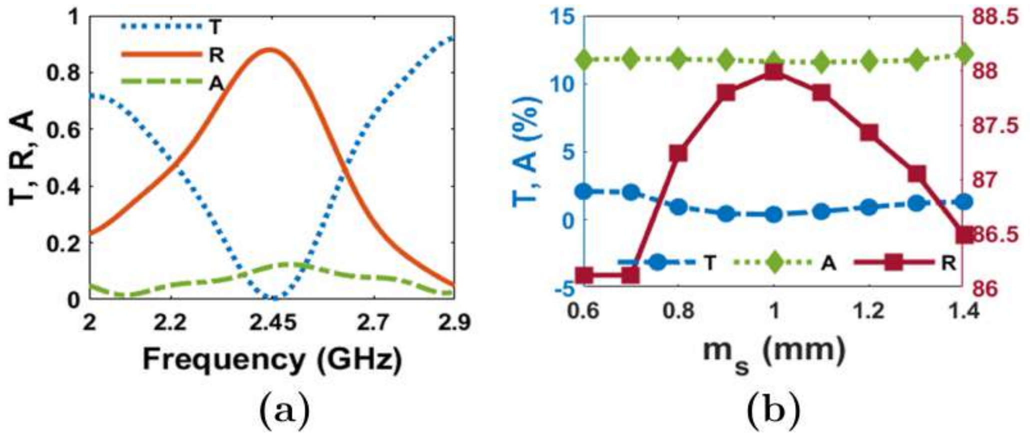

Figure 3.17: Simulation variation of T, R, and A with (a) frequency, and (b) with strip width m_s.

in [81], [82] requires increased machine timing to etch the smallest gap between thin conducting strips. Also, the MM reflector in [82] has conducting strips on both sides together, constituting the resonating behaviour in the operational band. Dual-side structures require proper positioning of strips above or below the dielectric layer to constitute a unit cell.

A small deviation in the symmetrical arrangement could result in resonances and a dominant imaginary part, raising losses. Therefore, the proposed single-sided MM unit cell, when used in an array, shall provide a good and considerable improvement in the reception compared to a patch [83]. An MM with reduced conducting area (1) reduces fabrication complexity by reducing the machining work; (2) reduces ohmic losses that conventionally occur in metal; (3) will be suitable for flexible substrates in wearable electronics applications.

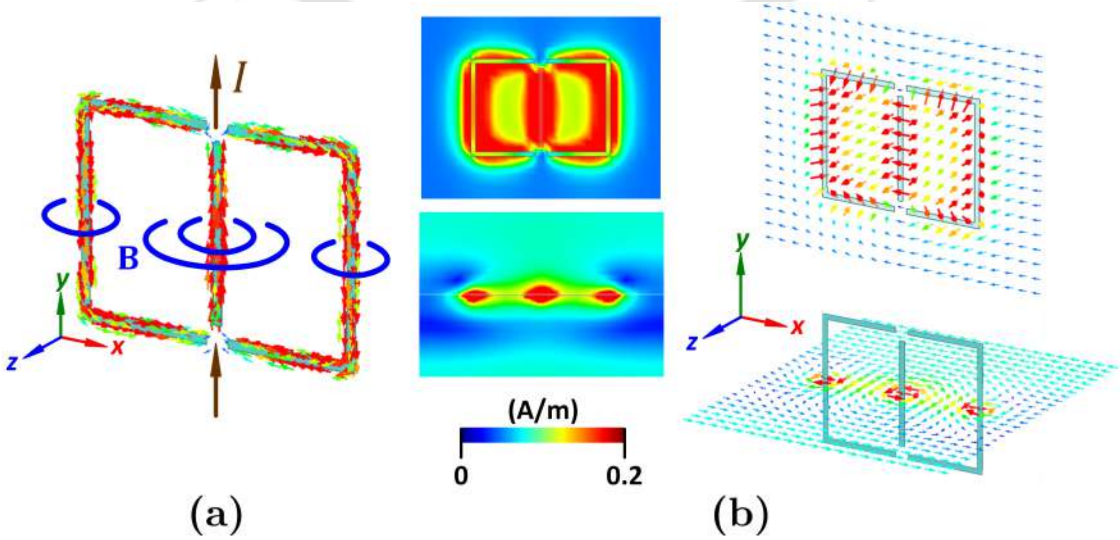

Figure 3.18: Simulation distribution of (a) surface currents and (b) magnetic field on MM unit cell at 2.45 GHz.

The surface current distribution at 2.45 GHz on the reflector unit cell is plotted in Figure 3.18a, which shows a circulating loop current in the xoy plane. The incident electric field is along the $y-$ axis, and the resultant induced magnetic field loops are indicated. The magnetic field plotted in Figure 3.18b shows the current induced on the outer walls is in the opposite direction of the current induced in the inner wall. This results in a dominant field in the inner wall. Also, the current exhibits identical distribution on both outer walls and follows the same direction, completing a loop. By looking at the surface electric currents, the response of the unit cell can be qualitatively assessed. The magnetic vector potential $\mathbf{A}$ due to the induced surface current at point r from the unit cell is expressed as follows,

$$\mathbf{A}(\mathbf{r}) = \frac{\mu_0}{4\pi}\int_V \frac{\mathbf{J}(\mathbf{r'})}{|\mathbf{r}-\mathbf{r'}|}dV \tag{3.1}$$

It follows that the condition $\nabla \cdot \mathbf{A} - \frac{1}{c^2}\frac{\partial \Phi_B}{\partial t} = 0$ is satisfied, where Φ_B is magnetic flux. The radiation fields of the structure can be derived from

$$\mathbf{H} = \frac{1}{\mu_0}(\nabla \times \mathbf{A}), \mathbf{E} = \frac{j\eta_0}{k}(\nabla \times \mathbf{H}) \tag{3.2}$$

where where $\eta_0 = \mu_0/\varepsilon_0$ is the impedance of free space and k is a wavenumber. In the far field, $|\mathbf{r}-\mathbf{r}'| = r - \hat{\mathbf{n}}\cdot\mathbf{r}'$ where $\hat{\mathbf{n}}$ is the unit vector in the direction of $\mathbf{r}'$, and r is the amplitude of $\mathbf{r}$.

MM reflector array

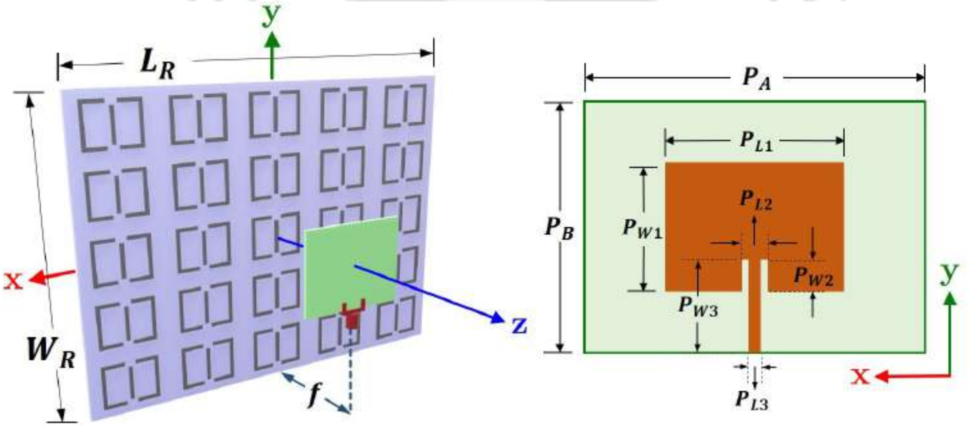

Figure 3.19: Schematic for obtaining optimum f for placement of feed patch.

Considering the maximum dimensions to be fitted on a rover as depicted in Figure 3.19, a maximum of 300×300 mm^2 size for reflector has been chosen. Therefore, two arrays, i.e. 3×3 and 5×5, arrays with length along $x-$ and width along $y-$axis, respectively, were constructed. The feed (or collector) patch realised on a 1.6 mm thick FR4 sheet as depicted in Figure 3.19 and its optimised dimensions are presented in Table 3.3.

Table 3.3: Patch antenna dimensions optimised for $f_0 = 2.45$ GHz

parameter	value (λ_0)	value (mm)	parameter	value (λ_0)	value (mm)
P_{L1}	0.31	37.95	P_{W1}	0.233	28.53
P_{L2}	0.0498	6.098	P_{W2}	0.061	7.469
P_{L3}	0.025	3.061	P_{W3}	0.181	22.163
P_A	0.612	74.939	P_B	0.474	58.041

The field radiated by the patch is aligned to the MM reflector unit cell excitation. For practical fit and space considerations, the optimum placement of the patch is estimated by EM modelling in CST for $0.5 \leq f/\lambda_0 \leq 0.9$. The gain variation with f is plotted in Figure 3.20a. It is evident that 5×5 array achieves a maximum of 6.71 dBi and is greater than 1 dBi, gain of 3×3 array at $f/\lambda_0 = 0.6$. The volumetric dimension of array is $L_R(= 2.245\lambda_0) \times W_R(= 1.835\lambda_0) \times f(= 0.6\lambda_0)$ mm^3 and is practically realisable to install on a rover. For a clear view, a rover prototype with MM reflector array installed on the top is shown in Figure 3.20b with the feed patch at $f = 0.6\lambda_0$.

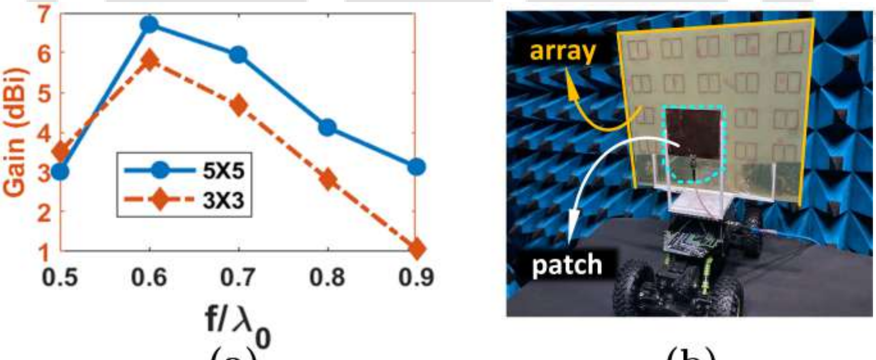

(a) (b)

Figure 3.20: (a) Simulation variation of gain for 3×3 and 5×5 MM reflector array with f/λ_0. (b) A rover prototype equipped with a 5×5 MM reflector and feed patch at $f/\lambda_0 = 0.6$.

A power flow distribution in E- and H-plane is given in Figure 3.21. The beam-focusing behaviour is illustrated in the xoz plane, wherein the magnetic field exhibits reflections in sidelobes. This MM reflector is ideally suited for powering from multiple dimensions in practical experiments. Also, when used on mobile rovers, the misalignment of the reflector or rotation towards a specific direction results in power loss. This reflector can effectively

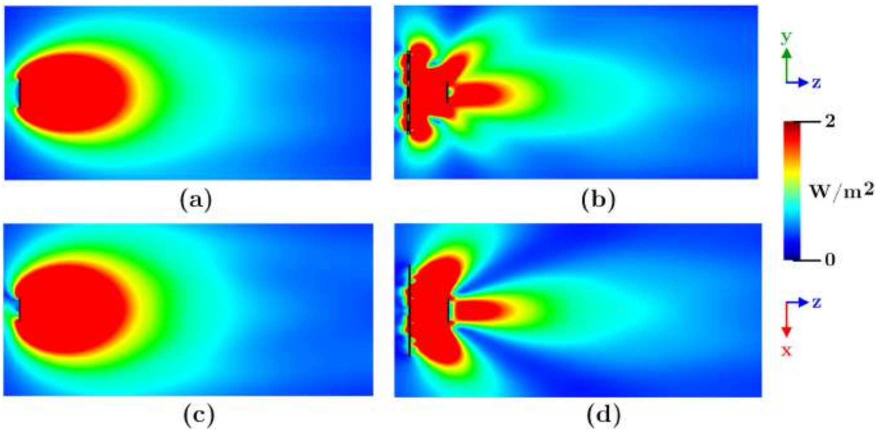

Figure 3.21: Simulation distribution of power flow at 2.45 GHz. (a) Patch without MM, (b) patch with MM at $f/d = 0.6$ in yoz plane. (c) Patch without MM, and (d) patch with MM at $f/d = 0.6$ in xoz plane.

receive or direct beams at three different angles simultaneously. The plot Figure 3.23 shows power reception from multiple dimensions required to compensate for the received power lost during misalignment of an unmatched line of sight angle. This makes the array useful in rover charging applications due to its lightweight and compact size.

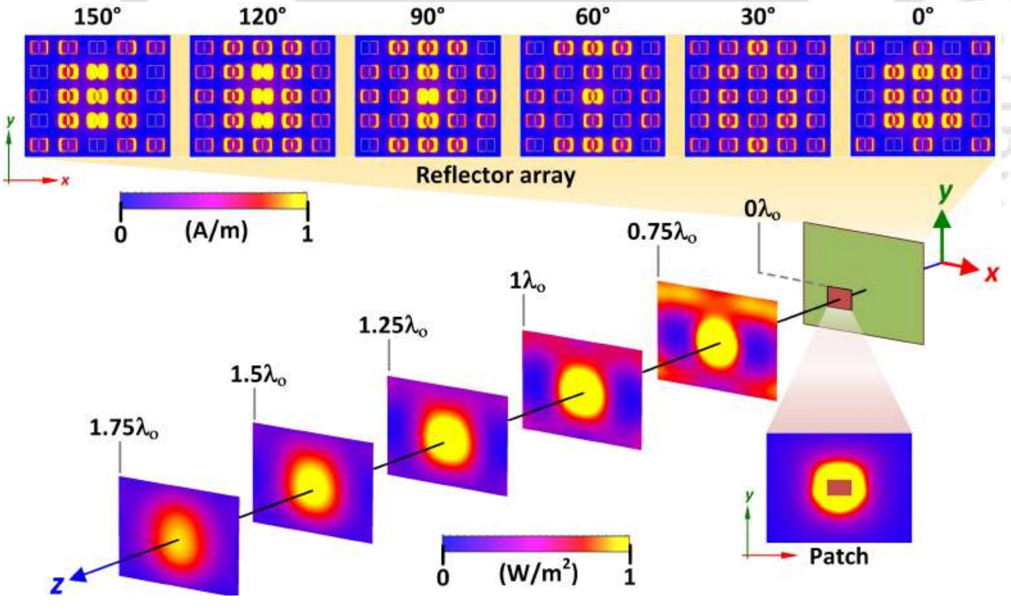

Figure 3.22: Simulation distribution at 2.45 GHz. Top: magnetic field on array in yoz plane, bottom: power flow in xoy plane.

Figure 3.22 and 3.23 presents the simulation distributions of fields at 2.45 GHz for optimum focus position. In practice, the misalignment in axis position reduces the reception power and results in zero for perfect cross polarisations [37]. The proposed MM reflector with an identical patch at optimum f provides the advantage of power reception from three distinct angles during rover displacement. At this stage, the sidelobes are useful to capture power. Unlike the parabolic reflectors that receive optimum in line-of-sight, the proposed MM reflector is advantageous for multi-directional power reception. Figure 3.22 presents the power distribution in xoy planes spaced $0.25\lambda_0$ apart in z^+ direction. A concentrated power flow is observed to improve the reception distance in microwave WPT systems.

Figure 3.23 presents the electric and magnetic fields for different phases with the patch at $f = 0.6\lambda_0$. The electric current on the walls of the unit cell, as shown in Figure 3.18a, which maintains a distance h from the substrate, contributes mainly to the radiation of the MM reflector in the z^- direction. The oscillating electric current emits an EM wave in both the z^+ and z^- directions as the array is realised with a uniform coating of the copper layer in the array. The induced field distribution alters at every phase and is displayed in Figure 3.22. The total antenna radiation is affected by the interference between the field emitted by the patch toward the reflector and the field reflected by the MM reflector in the z^+ direction. The area offered to the incident field in the xoz plane is higher than the xoy plane as the patch and unit cell have larger dimensions in the $x-$axis.

With an increase in the phase, the field induced at the reflector covers the entire array dimension. This results in reflection from every unit cell travelling towards the z^+. The total reflection is reduced when the field radiated by the patch and MM reflector are in phase. Therefore, the distance f significantly impacts the structure's ability to reflect EM waves. It is observed from Figure 3.23 that the MM reflector offers a smooth transition to the incidence field that emerges as a planar wave.

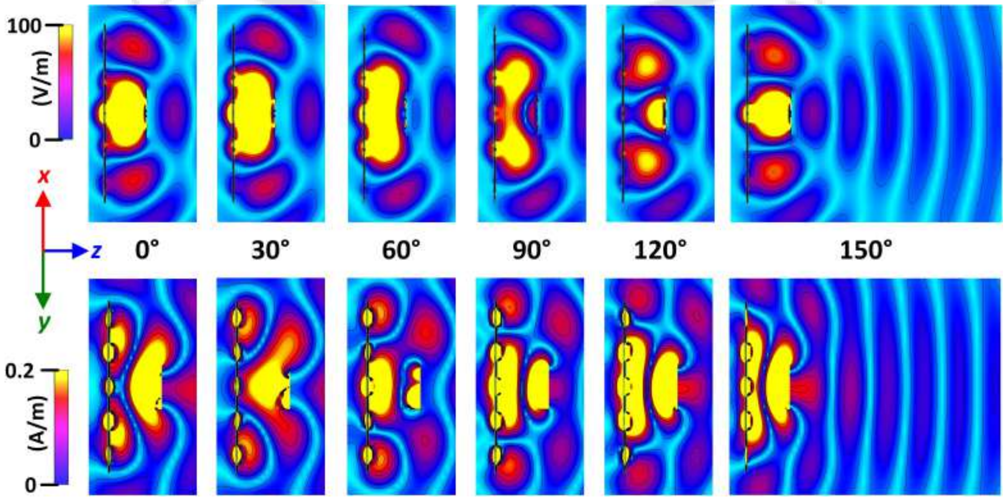

Figure 3.23: Propagation of EM wave; top: electric field, bottom: magnetic field.

3.4.2 Fabrication and measurement

The proposed MM reflector array is fabricated by a standard PCB fabrication technique on a 0.8 mm thick FR4 sheet. A 5×5 array is illuminated by a patch antenna at $0.6\lambda_0$ focus from the centre. The reflector assembly is mounted on a PLA material-based 3D-printed stand. The patch and reflector are tied with adhesive tape to stay at a standstill. As seen from Figure 3.20b, the entire assembly can be fitted onto a rover, meaning a prototype used for rover charging. A standard 9.43 dBi horn antenna at 2.45 GHz measures the far-field patterns in an anechoic chamber. Figure 3.24 illustrates the arrangement in E- and H-plane opted to measure the radiation patterns.

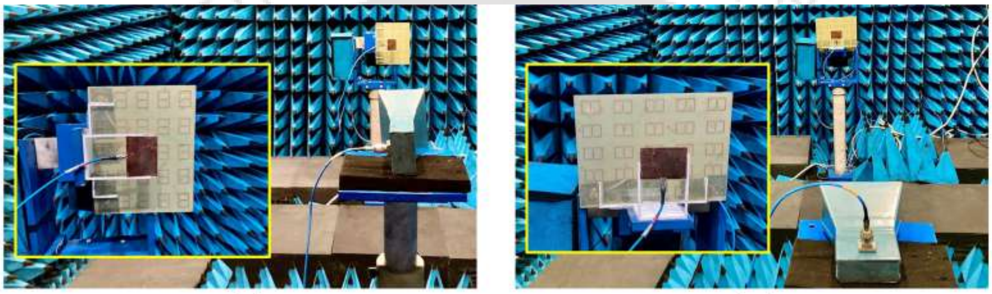

(a) (b)

Figure 3.24: Experimental arrangement for radiation pattern measurement in (a) E- and (b) H-plane.

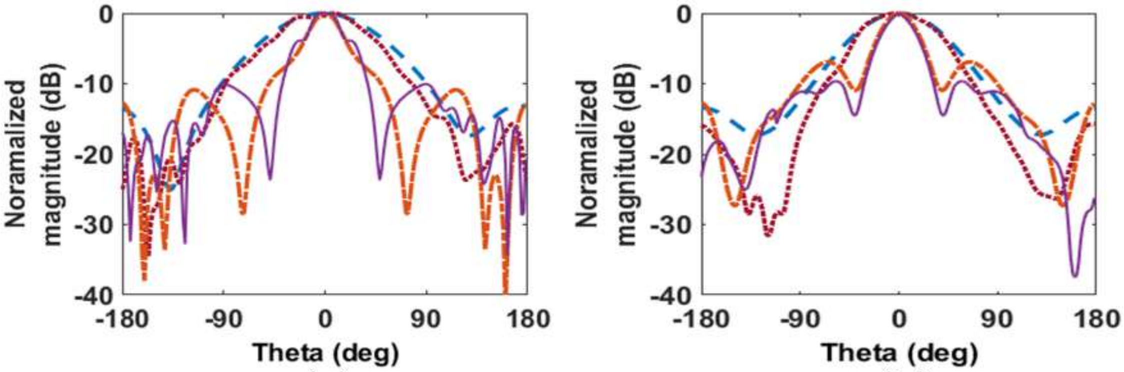

(a) (b)

Figure 3.25: Simulated and measured radiation pattern at 2.45 GHz for horn and horn with proposed MM array in (a) E- and (b) H-plane (solid, violet: MM reflector sim; dash-dot, orange: MM reflector mes; dot, brown: patch sim; dash, blue: patch mes).

The far-field radiation pattern in E- and H-plane at 2.45 GHz is given in Figure 3.25. A shift in E-plane sidelobes between $+90^\circ \leq \theta \leq +135^\circ$ in simulation to $+45^\circ \leq \theta \leq +120^\circ$ during measurement is observed. The discrepancy in the results is attributed to the tolerances in the symmetrically aligned feed patch placement at the focus. The radiation pattern measured in H-plane follows the simulation well despite a small variation for $-130^\circ \leq \theta \leq -80^\circ$. The measured and simulated studies demonstrate that the proposed MM reflector has a superior characteristic for increased power reception compared to a mono-patch antenna reception method.

3.5 Results and discussion

3.5.1 Radiation properties

A comparison between gain and beamwidth at 2.45 GHz on the simulation and measurement basis is tabulated in Table 3.4. A maximum of 14.12 dBi is recorded when the MM array is placed at $D_{opt} = 2.25\lambda_0$. Also, for the MM reflector placed at $f/\lambda_0 = 0.6$ from the feed patch, the Rx gain is 5.97 dBi. Nevertheless, observed improvements in manufacturing and physical placement tolerances are close to simulation predictions. The half-power beam widths in E- and H-plane are lowered by 34° and 20.8°, respectively. With the insertion of the MM reflector on the Rx side, HBPW is effectively reduced to 33° from 90° in the E-plane and to 43° from 75.6° in the H-plane.

Table 3.4: Gain and beamwidth comparison of Tx and Rx antenna

Case	Gain (dBi)		HPBW (deg)			
			E-plane		H-plane	
	sim	mes	sim	mes	sim	mes
Horn	11.3	10.6	51.5	60	49.3	46
Horn with MM array	14.8	14.12	24.3	26	22.7	25.2
Patch	3.16	2.78	93.8	97.2	79.8	75.6
Patch with MM reflector	6.71	5.97	32	33	37.8	43

3.5.2 Experimental setup

As formulated in Section-I, we set up a horn with an MM GRIN lens on the Tx side and a rover equipped with an MM reflector array and electric field probe at $f = 0.6\lambda_0$ on the Rx side. Figure 3.26 illustrates four types of Tx-Rx arrangement as Case-I,-II, -III, and -IV in an anechoic chamber. A rover equipped with an MM reflector and EP-601 field probe (Make: Narda) at focus is placed on the reception side. Figure 3.27 presents rover without and with MM reflector. A magnetron (make: Samsung, model no.:OM75S(31)ESGN) as a source is attached to the horn antenna open end waveguide throat via WR340 (86.36×43.18 mm^2) standard Connector Pressurised Rectangular (CPR) flange. The magnetron produces 800W peak power at 50% duty cycle for t = 18 seconds. A rover prototype is placed at $R = 3$ m line-of-sight from the Tx horn, and the electric field is measured using an electric field probe at R.

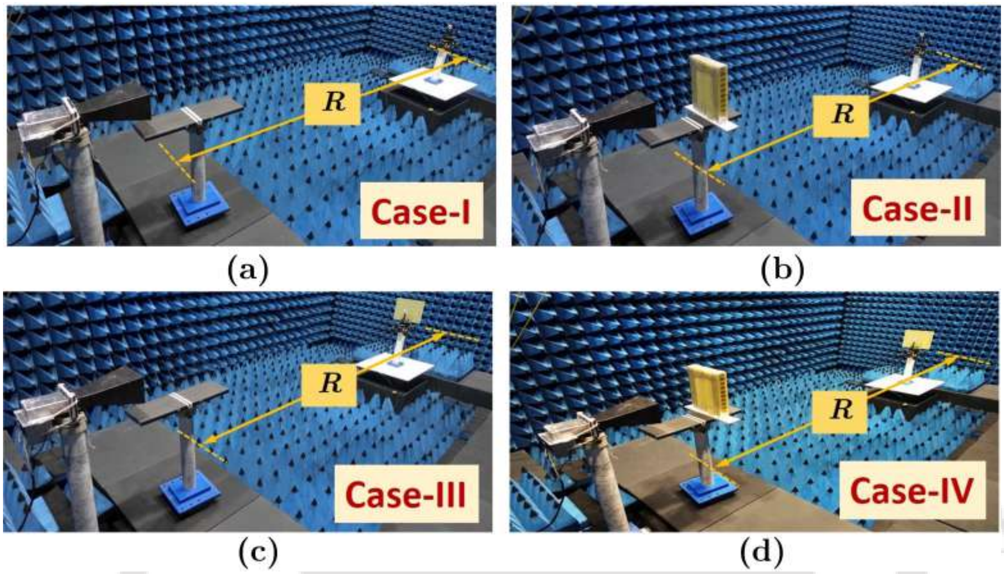

Figure 3.26: Experimental arrangement for electric field improvement at rover placed at $R = 3$ m in (a) Case-I, (b) Case-II, (c) Case-III, (d) Case-IV.

We study four cases, namely Case-I (Tx: horn, Rx: field probe), Case-II (Tx: MM GRIN lens, Rx: field probe), Case-III (Tx: horn, Rx: field probe+MM reflector), and Case-IV (Tx: MM GRIN lens, Rx: field probe+MM reflector). Figure 3.27 depicts the placement of the field probe with and without an MM reflector on the top of a rover. In Case-II,-IV field is recorded for $1.5\lambda_0 \leq D_{opt} \leq 2.5\lambda_0$ at $0.25\lambda_0$ intervals by placing MM array on a black wooden sheet.

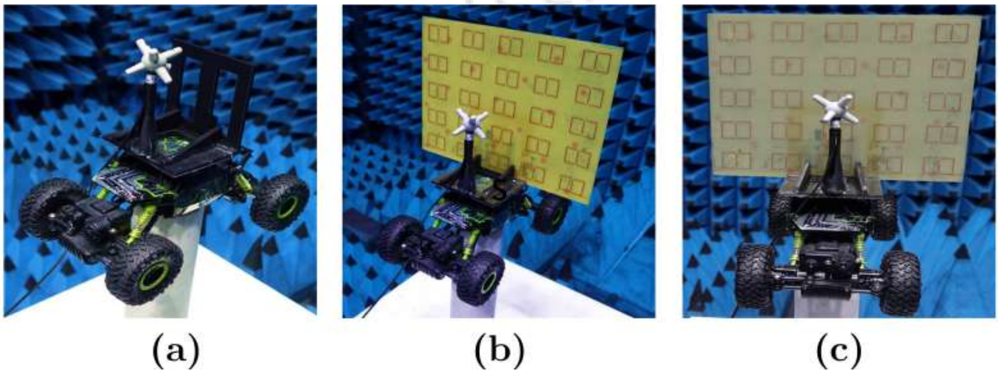

Figure 3.27: A rover prototype with EP-601 electric field probe at focus. (a) Without MM reflector, (b) and (c) with MM reflector.

It is evident from field distributions as plotted in Figure 3.12 that the positioning of the MM GRIN lens has a major impact. The shifts in the radiation plot reduce the effective beam area aimed for WPT. The lens positioned (inset of Figure 3.13c) ensures tightness for a uniform volumetric GRIN slab, providing maximum beam area fall onto the aperture. The GRIN distribution, as depicted in Figure 3.6b, considers radial variation with the centre at the lens centre. However, fabricated rectangular strips offer much coverage compared to a cylindrical slab with $-1.22\lambda_0 \leq r \leq 1.22\lambda_0$. Also, a slight deviation from the central axis in practical realisation and testing can reduce A_e, affecting the received electric field.

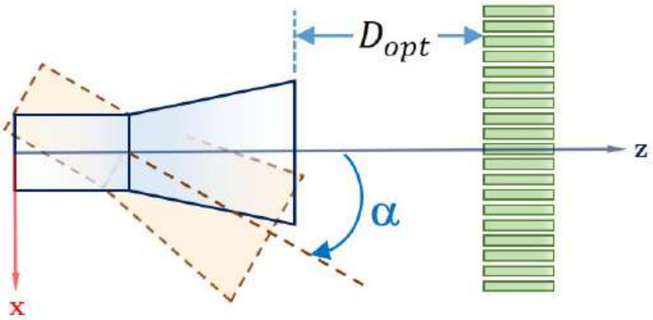

Figure 3.28: External deviation angle α

The discussions above are studied and tested by providing an external angular variation α and are depicted in Figure 3.28. The rotation is applied via a stepper motor mounted at the Tx bottom between $-60° \leq \alpha \leq +60°$ in ten degrees steps. An 18-sec microwave pulse with a 50% duty cycle is provided at every step. The radiated field propagates through free space, GRIN MM lens, and free space towards the reflector. The maximum electric field is recorded for $0 \leq t \leq 18$ sec period. It is to be noted that the field measured at $\alpha = 0°$ is maximum compared to any other value of $\alpha \neq 0°$.

3.5.3 Electric field measurement

Figure 3.29 shows the variation of the peak electric field at $R = 3$ m. In Case-I, a maximum of 173 V/m is obtained and is the lowest. With increment in D_{opt} from $1.5\lambda_0$ in Case-II, the field is rises from 169.13 V/m to 255 V/m at $D_{opt} = 2.25\lambda_0$ and reduces further. The field measured is 81.53 V/m higher compared to Case-I. In Case-III, using an MM reflector on the Rx side resulted in a maximum field of 243.8 V/m. It is 9 V/m lower than Case-II, as the gain of the Tx is higher than that of the Rx. At $D_{opt} = 2.25\lambda_0$, Case-IV achieves a

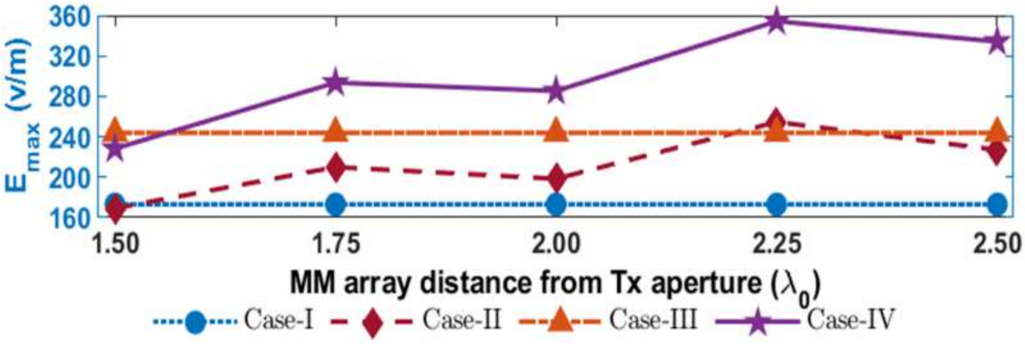

Figure 3.29: Variation of maximum electric field measured at $R = 3$ m with MM array distance and $\alpha = 0°$ for all four cases.

maximum of 354.33 V/m, which is 181.33, 99.33, and 110.53 V/m higher than Case-I, -II, and -III, respectively.

Except for $D_{opt} = 1.5\lambda_0$, it is also observed that the field received in Case-IV is always greater than the fields observed in the other cases for $1.75\lambda_0 \leq D_{opt} \leq 2.5\lambda_0$. A similar measurement is made for Case-II, and it is attributed to the fact that moving the MM array beyond $1.5\lambda_0$ reduces the extent of obstruction to the incoming waves from the antenna aperture. The measurements show that the proposed methodology enhances the field by a factor of two.

The received field is altered by misalignment in the MM array positioning to cover the horn aperture evenly. To investigate this, the received field for 10° intervals of $-60° \leq \alpha \leq +60°$ and is illustrated in Figure 3.30. The figure shows that when the MM array is included at $D_{opt} = 2.25\lambda_0$ in Case-II and -IV, the beam area narrows, which emerges to a pointed beam. A steep reduction in the field between $-20° \leq \alpha \leq +20°$ observed in Case-IV shall deliver concentrated power towards the Rx. In Case-I, the field lowers from 173 V/m at $\alpha = 0°$ to 107.53 V/m at $\alpha = +30°$ and 101.14 V/m at $\alpha = -30°$.

In Case-II, the field at $\alpha = +30°$ with $D_{opt} = 2.25\lambda_0$ decreased by 79.18% percent of its highest value at $\alpha = 0°$ and is 47.6 V/m less compared to $\alpha = +30°$ in Case-I. Figure 3.30 for Case-III shows a nearly similar distribution for $0 \leq t \leq 18$ sec, $-60° \leq \alpha \leq +60°$ as compared to typical WPT system, i.e. Case-I. The measured field is 49.165 V/m and 35.86 V/m higher than Case-I at $\alpha = -30°$ and $\alpha = +30°$ respectively. The field observed in Case-IV is highly concentrated between $-30° \leq \alpha \leq +30°$ and is reduced from 354.33 V/m at $\alpha = 0°$ to 78.23% and 73.58% of optimum.

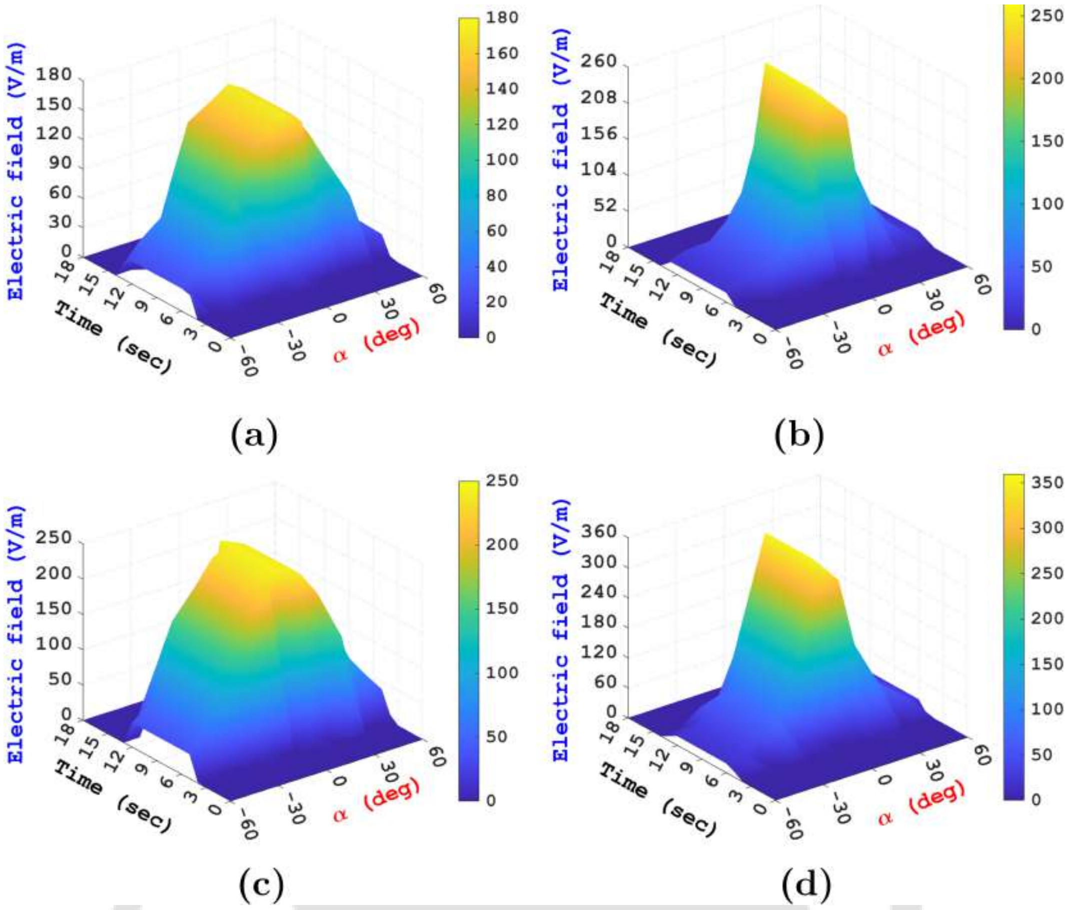

Figure 3.30: Distribution of measured electric field at $R = 3$ m for $-60^\circ \leq \alpha + 60^\circ$ with 50% duty cycle input pulse for (a) Case-I, (b) Case-II, (c) Case-III, and (d) Case-IV.

3.6 Summary

This chapter presented the design, fabrication, and experimental demonstration of electric field improvement at $R = 3$ m. The observations by using a novel MM GRIN lens and MM reflector are summarised below:

- The MM array, when placed at $D_{opt} = 2.25\lambda_0$ from Tx antenna aperture, a maximum of 14.12 dBi gain is measured and is 3.52 dBi greater than typical horn. The field on the receiving side is increased by utilising an MM reflector with a feed patch at $f/\lambda_0 = 0.6$. An improvement of 3.19 dBi gain is observed on the measurement basis, compared to the typical patch with a gain of 2.78 dBi operating at 2.45 GHz.

- The Tx GRIN MM lens and Rx MM reflector arrangement are tested, and far-field radiation patterns are analysed, showing good agreement and reduced half-power beam widths for effective beam focusing.

- A rover prototype incorporating MM reflector with electric field probe installed at the focus kept at $R = 3$ m fed with 800W peak power magnetron pulsed at 50% duty cycle. Four case studies demonstrate an improvement of 181.33, 99.33, and 110.53 V/m in Case-IV compared to Case-I,-II,-III, respectively, for $D_{opt} = 2.25\lambda_0$ and $f/\lambda_0 = 0.6$.
- Considering misalignment effects in physical array placement, the Tx horn is rotated by $-60^\circ \leq \alpha + 60^\circ$ keeping the MM array constant. The distribution of the measured electric field shows considerable improvement in power concentration for far-field microwave WPT applications.

Experiment findings also indicate that microwave WPT can efficiently use a novel GRIN MM lens as a repeater between Tx-Rx pairs in the far field. The separation distance can also be increased for high-power applications to allow for an equivalent layout on the Rx side. As demonstrated in the experimental investigation, the battery recharge duration can be significantly reduced by including an MM reflector on the Rx side*. The lightweight and compact MM reflector is best suited for mobile receivers, e.g., rovers, aerostats, drones, etc., in a 2.45 GHz microwave WPT system.

The planar MM reflector offered ease in placement and less Rx antenna assembly volume, making the system reliable for mobile use. The next chapter discusses using novel planar MM as a sub-reflector in dual reflector antennas. With the inclusion of the MM sub-reflector in the dual-reflector antenna, simultaneous power beaming in multiple directions is achieved.

---

*Shashank. S. Kulkarni**, Amarnath Kumar, Niraja P. Sanghai, Anurag R. Lambor, Sisir Kumar Nayak, and D. Senthil Kumar "An Electric Field Enhancement System For Automated Mobile Vehicle Charging," Grant No:437297, Grant date:05/07/2023, for twenty years from 27/10/2022.

Chapter 4

Design of metasurface sub-reflector based dual-reflector antenna for multi-directional beaming

---

Overview

This chapter presents a novel Metasurface sub-reflector (MSSR) dual-reflector antenna inspired by the Cassegrain arrangement for simultaneous power beaming in multiple directions. By changing the focal distance, i.e., placement of MSSR, power distribution in the sidelobe can be altered. Also, the gain in the main direction and half-power beam widths can be adjusted. The inclusion of MSSR can be helpful in scenarios wherein multiple small targets spaced at sidelobes can be charged. The performance of the proposed antenna at 2.45 GHz is assessed by designing a perfectly reflecting MS unit cell and the experiments are performed by fabricating its prototype. The electric field measured shows higher values at three distinct angles, including the main direction, showing the remarkable capability of simultaneous beaming.

4.1 Introduction

Wireless power transfer technology offers the convenience of charging devices anywhere and anytime [23]. However, current WPT technologies relying on electromagnetic induction [115], [116] have limited range and struggle with multitarget charging due to the need for precise alignment. To achieve simultaneous WPT for multiple targets, a new design using radiated microwave beams with non-diffraction self characteristics [117], [118] is necessary. Cassegrain antennas are a popular choice for their high gain, low profile, and strong directionality [119]- [122]. They are especially suitable for producing multiple beams due to their superior performance, reduced weight compared to lens antennas, and well-established technology [123]- [126]. While hyperbolic sub-reflectors require precise positioning for effective reflection, planar reflectors offer simple arrangement. They can be installed with less effort, resulting in a smaller physical volume for the entire Cassegrain antenna assembly. To meet the demands of directional beaming, Metasurfaces (MS) in the form of 2D thin arrays have been explored. The Metasurface Reflector (MSR) possesses electromagnetic wave manipulation capabilities, tailored to the desired frequency [127]- [131]. The binary coded MS [132]- [134] enables the deflection or reflection of electromagnetic waves at specific or predefined angles (θ, ϕ) through the controlled switching of diodes.

While conventional phased arrays [135] can modulate electromagnetic waves to produce specialised beams, they require multiple phase shifters, which adds to the system's cost. To overcome this, we employ a metasurface [136], [137] to flexibly adjust the incident electromagnetic wave from the feed, thus eliminating the need for phased arrays. Using a metasurface sub-reflector (MSSR) in conjunction with the MSR enables the generation of multiple beams, focusing power in desired directions without interference caused by traditional feed horns. The mathematical calculations for EM wave incidence onto a planar surface are simpler than a hyperbolic sub-reflector.

This chapter introduces a planar metasurface sub-reflector (MSSR)-based dual-reflector antenna capable of simultaneous power focusing in specific directions. The combination of bit coding and phase-changing MS enables selective reflection angles for radar, space, and WPT applications in the microwave range. The following sections discuss different reflector antenna types and the fundamentals of Cassegrain antennas. Subsequently, the theory and design of the planar sub-reflector Cassegrain antenna are presented, followed by an investigation into the MSSR unit cell and array design at 2.45 GHz. The results and discussions section covers simulation and experimental studies using a fabricated prototype, summarising the performance study in the final section.

4.2 Reflector antenna

4.2.1 Types of reflector antenna

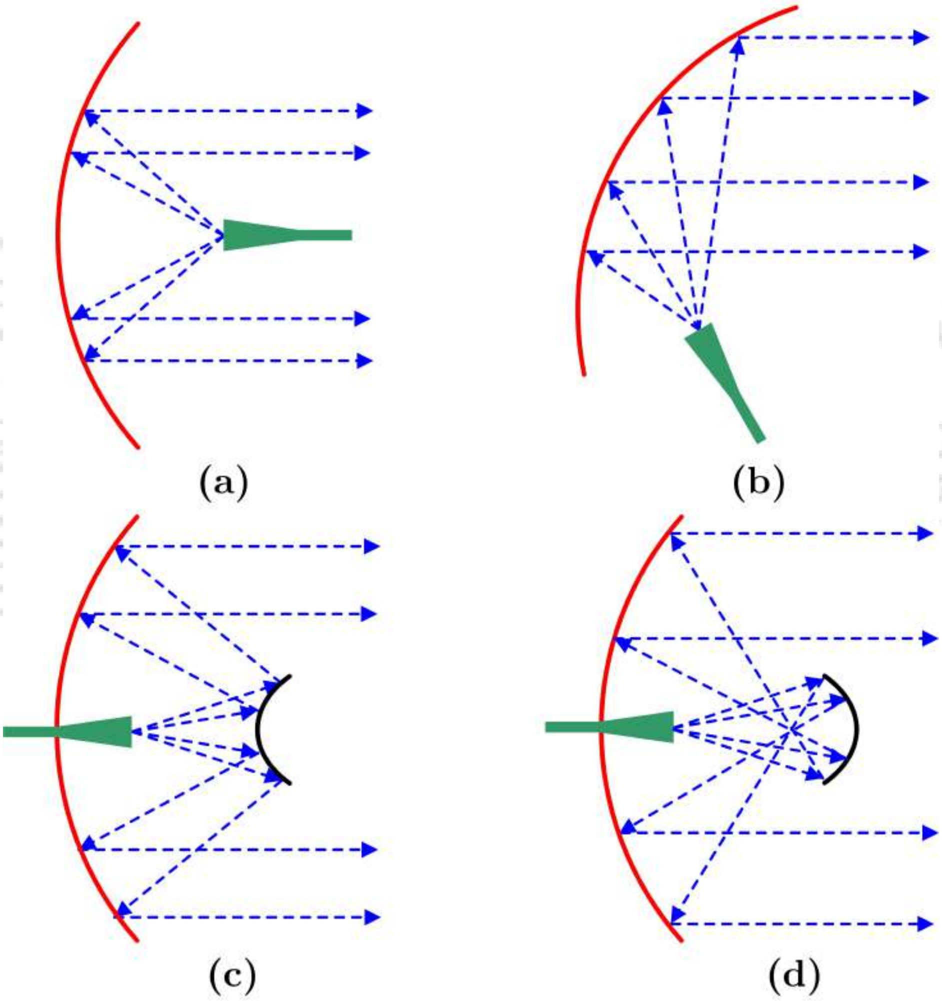

Figure 4.1: Basic types of reflector antenna. (a) Parabolic feed, (b) offset feed, (c) Cassegrain feed, and (d) Gregorian feed.

The success of space exploration has led to the development of antenna theory. Complex antennas had to be employed to broadcast and receive signals that had to travel millions of miles due to the necessity of communicating over long distances. A parabolic reflector is a relatively typical antenna shape for such an application. This antenna has been constructed with huge diameters compared to their operating wavelength. Such huge dimensions are necessary to attain the high gain to transmit or receive signals after travelling millions of kilometres. A waveguide excites a horn antenna, which is a practical and efficient radiator. One of the most popular antennas used as a focal point feed in many reflector antennas is the horn antenna since the horn's losses are often insignificant. The horn aims to create a more directive, uniform phase front with a bigger aperture than the waveguide.

The parabolic reflector antenna is the most prominent microwave antenna, which is typically considered for microwave systems, is the parabolic reflector antenna. The small wavelengths involved allow reflector antennas to be used at microwave frequencies. At lower frequencies, reflectors are theoretically feasible, but the antennas would have to be enormous in size because of the longer wavelengths. Various radiators (horn, dipole, helical) may be used with parabolic dish feed geometries for feeding parabolic dish antennas. Also, pyramidal and conical horn antennas are the most practical fit for feed.

4.2.2 Cassegrain antenna

The primary reflector in the traditional Cassegrain configuration is parabolic, and the secondary mirror is hyperbolic. Modern variations can incorporate a hyperbolic primary for improved performance, and either or both mirrors might be spherical or elliptical for simpler fabrication. The Cassegrain reflector is named after a reflecting telescope designed by Laurent Cassegrain in 1672. The classical Cassegrain has a hole in the primary mirror and a secondary mirror that is hyperbolic and reflects light down through it.

The secondary reflector is often installed on an optically flat, optically clear glass plate that closes the telescope tube on smaller telescopes and camera lenses. The closed tube is kept clean, and the primary is protected at the expense of a slight decrease in light-gathering power. The parabolic mirror reflects parallel light beams entering the telescope to its focus, which is also the focus of the hyperbolic mirror. The image is then seen at the other focus of the hyperbolic mirror once it reflects those light rays there. Including a second reflector, called the sub-reflector or sub-dish, provides an extra degree of freedom for achieving better performance in various applications. The Cassegrain configuration often offers several advantages, such as

- flexibility to place the feed in a suitable location
- minimise in minor lobe radiation
- the capacity to scan or modify the beam by repositioning one of the reflecting surfaces.

Hannan [119] pioneered the Cassegrain configuration analysis as a microwave antenna. His work involved deriving the geometrical shape of the reflecting surfaces using geometrical optics (GO) and introducing the concepts of the virtual feed and equivalent parabola. Traditionally, reflector designs were based on GO, especially when the reflectors' sizes and curvature radii were considerably compared to the operating wavelength. Both single-reflector and double-reflector (Cassegrain) systems aimed to transform a spherical wave at the source (focal point) into a plane wave. Hence, the reflecting surfaces of these reflector systems were primarily selected to convert the spherical wavefront into a planar phase. In this configuration, when energy is incident on the reflector system in parallel rays, the sub-reflector receives energy reflected from the primary reflector, which has a large concave surface. The convex surface of the sub-dish then reflects this energy towards the vertex of the main dish. By placing the paraboloid and hyperboloid reflectors as the primary and sub-reflectors, respectively, the incoming parallel rays are focused at a single point, and the receiver is positioned at this focal point.

The concept of the virtual feed, as described by Hannan [119], proves to be a valuable tool for analysing the performance of a Cassegrain antenna. This method involves substituting the real feed and sub-reflector with a virtual feed positioned precisely at the focal point of the primary reflector. By locating the optical image of the real feed, it becomes possible to determine the configuration of this virtual feed. The convex curvature of the sub-reflector leads to an increase in beamwidth, and this widening can be calculated by equating the ratio of the virtual-feed beamwidth to the real-feed beamwidth with the ratio of the angles. By utilising a Cassegrain arrangement with a large feed and a short focal length for the primary reflector, it becomes feasible to design an antenna with relatively small dimensions. This makes the virtual-feed approach a useful and practical method for analysing and optimising Cassegrain antennas.

The concept of the equivalent parabola offers a solution to address certain limitations of the virtual-feed approach [119]. This approach replaces both the primary dish and the sub-reflector with an equivalent focusing surface positioned at a specific distance from the real focal point. This surface is defined as the locus of intersection of incoming rays parallel to the antenna axis and the extension of the respective rays converging towards the actual focal point. Using simple geometrical optics ray tracing, the equivalent focusing surface for a Cassegrain configuration is a paraboloid with a focal length equal to the distance between its vertex and the real focal point. This equivalent system can also be reduced to a single-reflector configuration with a different primary reflector but the same feed. The theoretical formulations for analysing this system are provided in Appendix C. Similarly to the primary dish and the sub-reflector, this equivalent focusing surface effectively concentrates an incoming plane wave incident from the opposite direction towards the actual focal point.

4.3 Planar sub-reflector cassegrain antenna

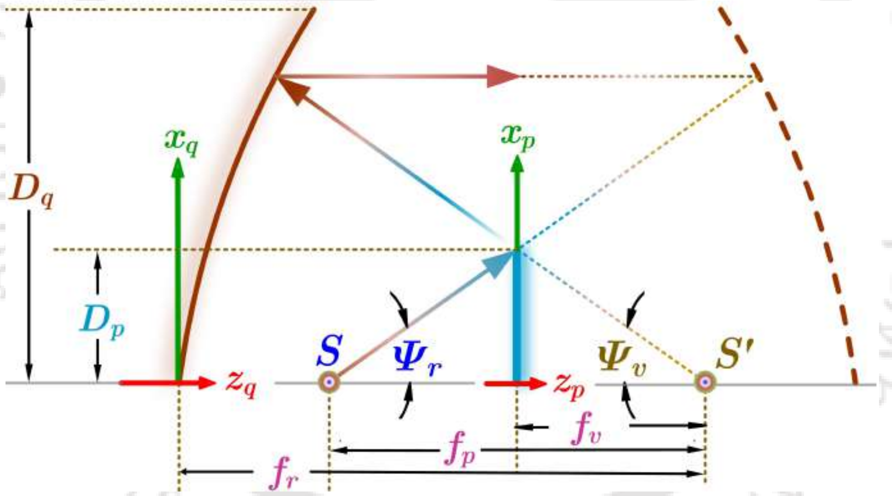

Figure 4.2: Schematic of a planar sub-reflector based Cassegrain reflector antenna.

Figure 4.2 presents the geometric arrangement of a planar sub-reflector Cassegrain antenna. The ray emitted from source S strikes the planar sub-reflector, which extends in the (z_p, x_p) coordinates and has a maximum dimension of D_p. The sub-reflected ray propagates in the same direction as the source after undergoing secondary reflection from a parabolic dish, which extends in the (z_q, x_q) coordinates and has a maximum dimension of D_q. To analyse the reflection system, a virtual source S' and the parabolic contour of the main dish are introduced. The dependency of design parameters on each other is determined based on the main dish's contour given by [119],

$$z_q = \frac{x_q^2}{4f_r} \tag{4.1}$$

$$\tan\left(\frac{\Psi_v}{2}\right) = \frac{D_q}{4f_r} \tag{4.2}$$

$$\frac{1}{\tan(\Psi_v)} + \frac{1}{\tan(\Psi_r)} = \frac{2f_p}{D_p} \tag{4.3}$$

$$1 - \frac{\sin\frac{1}{2}(\Psi_v - \Psi_r)}{\sin\frac{1}{2}(\Psi_v + \Psi_r)} = 2\frac{f_v}{f_p} \tag{4.4}$$

where f_r is distance between center of primary reflector and virtual source S', f_p is distance between real source S and virtual source S', f_v is distance between planar sub-reflector and S', D_p is maximum dimension of planar sub-reflector, D_q is maximum dimension of main parabolic reflector, and Ψ_r, Ψ_v are real and virtual angles respectively.

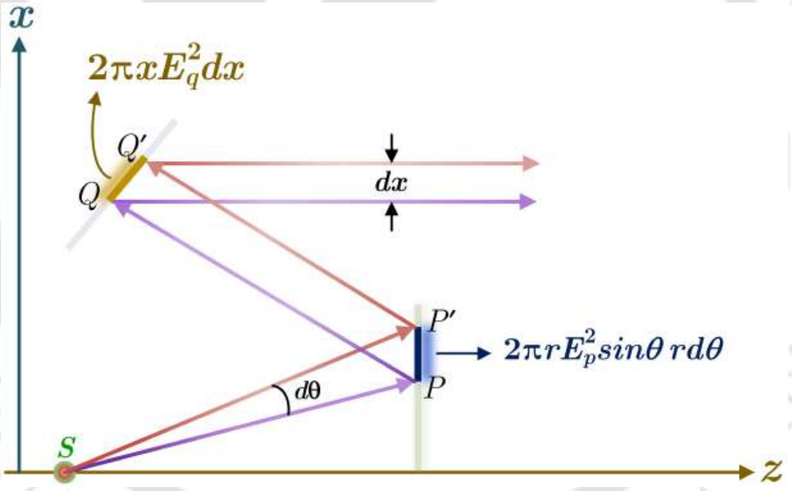

Figure 4.3: Schematic of energy flow in a planar sub-reflector based Cassegrain antenna.

The energy conservation law states that the power radiated from the feed horn must equal the spread over energy on a circle that is normal to the refracted main beam in the aperture plane. Figure 4.3 shows the energy relation, which may be expressed in the energy conservation relation as

$$E_p^2(2\pi r)\sin\theta r d\theta = 2\pi x E_d^2 dx \tag{4.5}$$

In (4.5) E_p^2 and E_d^2 should be normalized. The overall energy conservation incident to the sub-reflector and distributed throughout the aperture is used for this purpose. The overall energy conservation may be represented as follows:

$$\int_0^{\theta_m} r^2 E_p^2 \sin\theta d\theta = \int_0^{x_m} x E_d^2 dx \tag{4.6}$$

where θ_m is maximum incident angle. The variation of r in the left side integral of (4.6) is very small compared to the changes in E_p^2. Therefore, in the case of integration, r is the constant C.

$$C^2 \int_0^{\theta_m} E_p^2 \sin\theta d\theta = \int_0^{x_m} x E_d^2 dx \tag{4.7}$$

By dividing (4.5) by (4.7), E_p^2 and E_d^2 are normalised and given as [138],

$$\frac{dx}{d\theta} = \frac{E_p^2 (\frac{r}{C})^2 \int_0^{x_m} E_q^2 x dx}{x E_q^2 \int_0^{\theta_m} E_p^2 \sin\theta d\theta} \tag{4.8}$$

where C is a constant, E_p and E_q are the field distributions on the primary and the secondary side, respectively. The required E_q can be achieved with proper design and positioning of the sub-reflector and dish reflector. Therefore, the inclusion of MSSR at the planar side will provide directional capabilities to E_p to produce a required pattern E_q when reflected by D_q.

The fundamental equations establish a connection between the dimensions and angles of the primary and secondary reflectors in designing an MSSR-based dual-reflector antenna. The concept of an equivalent parabola and virtual feed aids in developing this antenna configuration. The flat-sub dish reflectors are characterised by infinite eccentricity ($e = \infty$) and have non-zero values for f_p and f_v [119]. The positioning of the MSSR array near the horn plays a crucial role, affecting f_r while maintaining $\Psi_v/\Psi_r = 1$. However, if the dimensions of the MSSR array are much larger than those of the primary dish, then $e = 1$, and $f_p = \infty$, resulting in blockage to all the incident waves.

4.4 Metasurface sub-reflector

4.4.1 Unit cell

Based on the MM reflector design presented in Chapter 3, this section describes the design, optimisation and analysis of the planar Metasurface sub-reflector array. Figure 4.4a illustrates the geometry of an MSSR unit cell designed on a 0.8 mm thick FR4 substrate ($\varepsilon_r = 4.3 + j0.025$). A 35 μmm thick conductor is used in the design. The front side consists of a plus '+' shape that follows a simple geometry, also found a well-derived approach [139]. The strip length is p, and the width is s at the substrate centre. On the back side, the letter 'I' is designed by joining two horizontal strips (length×width $= a \times b$) and a vertical strip (length×width $= c \times d$) in xoy plane. The simple geometries on the front and back sides provide extra space to tune to the desired frequency. Also, the thin metallic portions keep the internal resistive losses (R_{ext}) to a minimum that generally occurs as ohmic and thermal losses at the resonance.

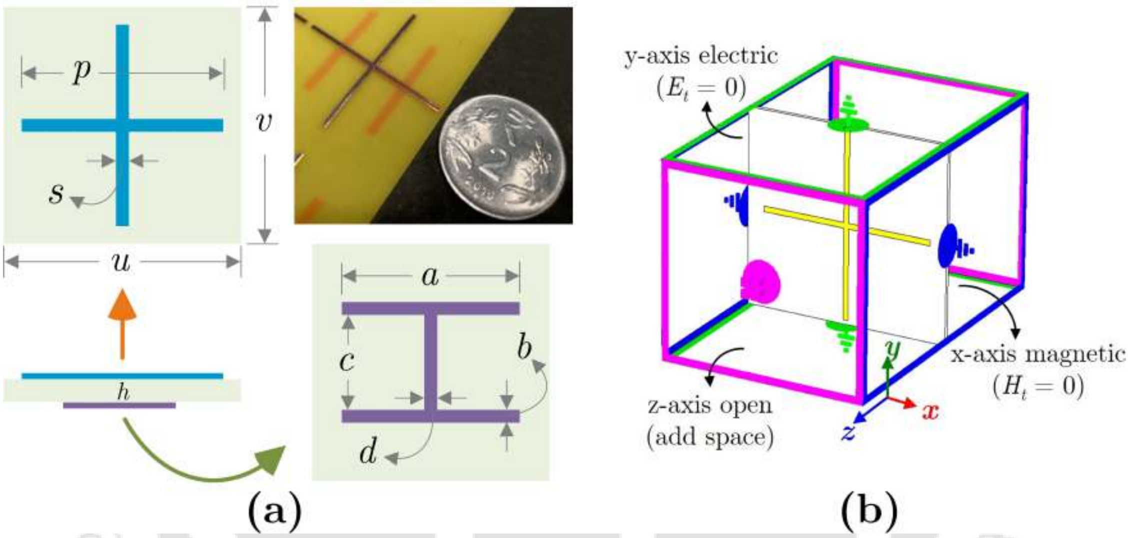

Figure 4.4: (a) Geometry of the proposed MM reflector unit cell designed on $h = 0.0065\lambda_0$ thick FR4 substrate. (b) Simulation boundary condition in CST.

Table 4.1: Unit Cell Parameters Optimised for $f_0 = 2.45$ GHz

parameter	value (λ_0)	value (mm)	parameter	value (λ_0)	value (mm)
a	0.204	25	p	0.273	33.5
b	0.016	2	s	0.008	1
c	0.114	14	u	0.326	40
d	0.015	1.8	v	0.285	35

The MSSR unit cell is simulated using CST software for a frequency range of 2−2.9 GHz, with a $y-$polarized field incidence. Figure 4.4b shows the imposed boundary conditions during the electromagnetic modelling. The optimum performance at the operating frequency is achieved by tuning the constructional parameters, as illustrated in Figure 4.5a. The calculated S-parameters reveal a resonance at the operating frequency, with the obtained values at 2.45 GHz being $S_{11} = -0.844 + j0.485$ and $S_{21} = -0.021 + j0.014$.

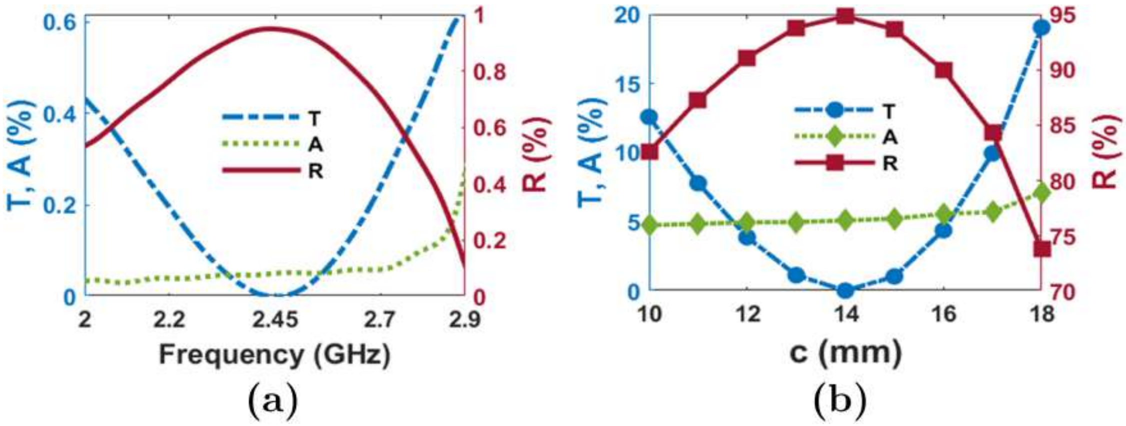

Figure 4.5: Variation of T, R, A for unit cell. (a) With frequency for optimum dimensions, and (b) with different values c at 2.45 GHz.

From the S-parameters, the Transmittance ($T = |S_{21}|^2$), Reflectance ($R = |S_{11}|^2$), and Absorptance ($A = 1 - T - R$) are determined, all showing a resonance at the operating frequency. At this point, the unit cell exhibits minimum transmission ($T = 0.065$) and maximum reflection ($R = 0.948$) with an absorptance value of $A = 0.051$. Notably, changes in the physical widths and lengths of the conducting strips lead to shifts in the resonance. The variation of the effective surface area and the gap between strips, as shown in Figure 2.7, affects the inductance and capacitance, influencing the resonant frequency relation. Figure 4.5b displays the variation of T, R, and A with distinct values of c. Over the range $10 \leq c \leq 18$ mm, the transmission remains above 70% for all values. The minimum values of $\%T = 0.065$ and $\%A = 5.126$ within 5% are observed for $c = 14$ mm and are considered in the study.

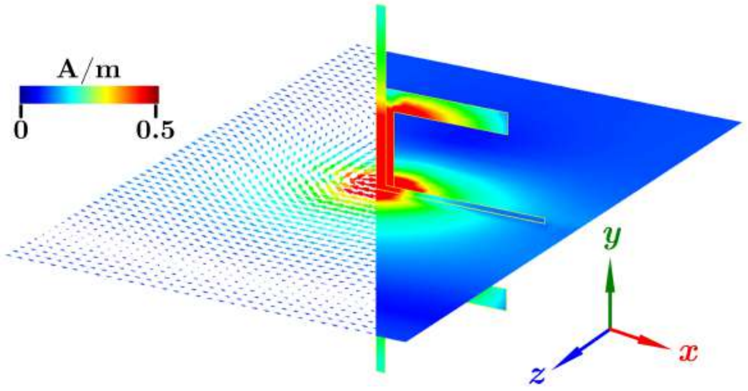

Figure 4.6: Simulation distribution of magnetic field at 2.45 GHz.

Figure 4.6 displays a magnetic field at 2.45 GHz on the unit cell. It shows the formation of a closed loop line in the xoz plane, forming a magnetic dipole. The conducting area (S)

remains constant and hence increment in dipole moment ($\mathbf{m}$) is a result of higher induced current as $\mathbf{m} = I\mathbf{S} = IS\hat{\mathbf{a}}_n$. Therefore, the magnetic field ($\mathbf{H}$) is also increased as $\chi_m\mathbf{H} = IS\hat{\mathbf{a}}_n/V$ where V is volume.

4.4.2 MSSR array

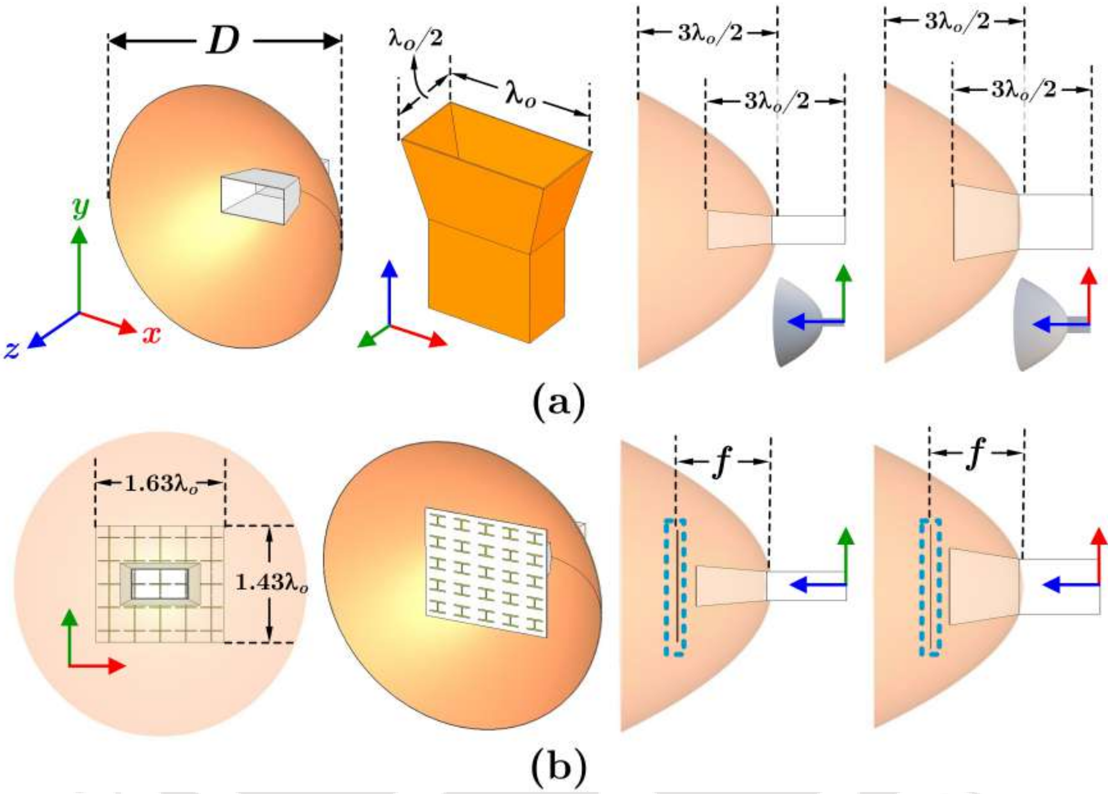

Figure 4.7: (a) Schematic of a dish reflector and a feed horn. (b) A planar MSSR positioned at f from feed horn in Cassegrain arrangement.

Figure 4.7a provides information about the dimensions of the primary parabolic dish reflector, feed horn, and a cross-sectional view. The parabolic dish has a diameter of $D = 4.33\lambda_0$ and a depth of $3\lambda_0/2$, constructed using a 1.2 mm thick PEC (Perfect Electric Conductor) sheet. The waveguide has a cross-sectional area of 86.36×43.14 mm^2 and a length of $3\lambda_0/4$. It supports the TE_{10} mode, and an electric field parallel to the y-axis radiates through a $\lambda_0 \times \lambda_0/2$ mm^2 aperture in the xoy plane, flaring with a length of $3\lambda_0/4$ from the waveguide's open end. The overall cubic dimensions of the completed Cassegrain reflector antenna are $D \times 2.25\lambda_0 \times 2.25\lambda_0$ mm^3.

Figure 4.7b presents the planar MSSR-based Cassegrain antenna, featuring a 5×5 MSSR array with a length of $1.63\lambda_0$ in the x-axis and $1.43\lambda_0$ in the y-axis, with a thickness of 0.8

mm. The MSSR array exhibits symmetry in the principal radiation planes and uniformly covers the feed horn aperture, resulting in minimal blockage to the secondary reflections. This configuration enhances the coverage of incident waves from the feed point. It reduces blockage to the reflected waves, leading to a concentrated beam in the desired direction and propagation angle. The focus (f) is the distance between the waveguide's open end and the MSSR array, optimised to achieve the desired radiation beam characteristics. Notably, the distance between the MSSR array and the feed horn aperture is equal in both the E-plane and H-plane.

4.5 Results and discussion

4.5.1 Simulation

The adjustment of the MSSR array's position relative to the feed horn aims to optimise both the gain and sidelobe values, as demonstrated in Figure 4.8a. The figure reveals that the maximum achieved gain is 16.2 dBi when the focus (f) is set to $0.93\lambda_0$. As the focus is increased within the range of $1\lambda_0$ to $1.18\lambda_0$, the gain decreases to 15.1 dBi, 13.20 dBi, and 10.60 dBi, respectively.

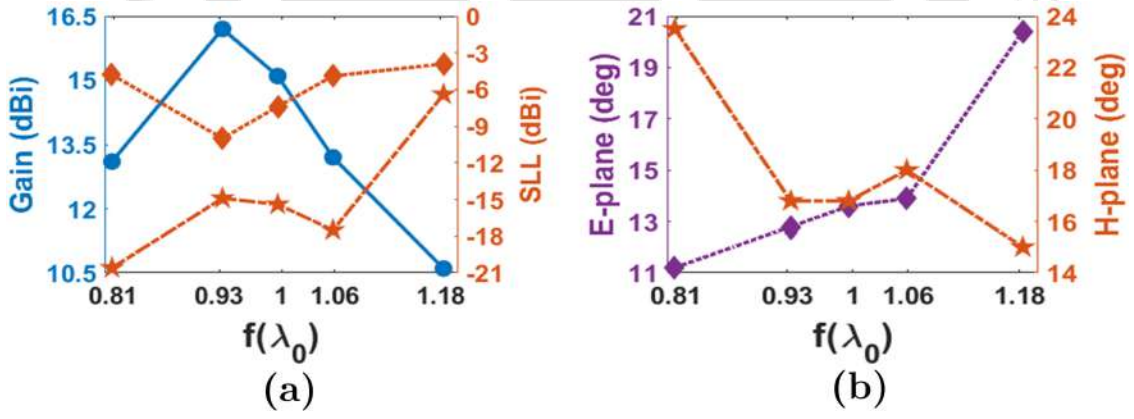

Figure 4.8: Variation of (a) gain and sidelobe level (SLL) and (b) half-power beamwidth (HPBW) with focus.

Figure 4.8a also displays the variations in sidelobe levels (SLLs), illustrating a reduction in main lobe power distribution with an increase in f. The adjustment of the focus allows for control over the power in sidelobes, and at the highest focus value ($= 1.18\lambda_0$), the SLLs approach half-power levels in both the E-plane and H-plane. This configuration holds promise for applications such as simultaneous charging, where most of the power is concentrated within the sidelobes. Furthermore, the variation of f has an impact on the $dx/d\theta$ in equation (4.8), leading to an increase in the travel time required for rays to reach the main reflector.

Figure 4.8b presents the variation of the antenna's half-power beamwidth (HPBW). Notably, the HPBW in the H-plane decreases as the focal length (f) increases, while the HPBW in the E-plane increases from 11.20° to 20.40° with an increase in f. The increase in f results in better alignment of the incident electric field, which offers a smaller cross-sectional area. Consequently, most of the radiation is sub-reflected towards the primary dish. Additionally, the length of the MSSR array in the H-plane provides a larger area for near-positioned focus. When the H-field interacts with the horizontal strips, it reflects in a split distribution. Consequently, the H-plane experiences a reduction in HPBW for higher focus values.

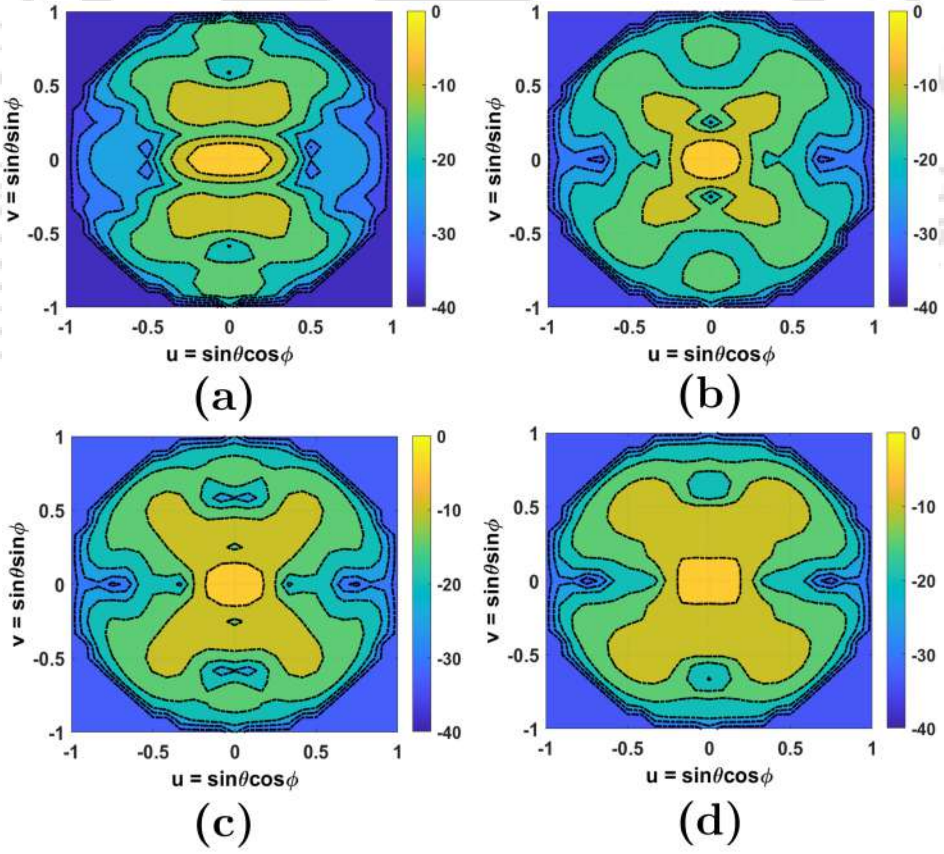

Figure 4.9: Distribution of gain for $0 \leq \phi \leq 2\pi$, $0 \leq \theta \leq \pi/2$. (a) $f = 0.81\lambda_0$, (b) $f = 0.93\lambda_0$, (c) $f = 1\lambda_0$, and (d) $f = 1.06\lambda_0$.

Figure 4.9 illustrates the radiation in main directions for various gain focus distributions. When the focus is set to $f = 0.81\lambda_0$, the figure demonstrates power splitting into dual beams, resulting in higher sidelobe levels (SLLs). On the other hand, at focus $f = 0.93\lambda_0$, the antenna achieves its highest gain with almost equal power in the sidelobes. The MSSR array effectively splits the beam, leading to low values of half power beamwidth (HPBW) in both the E- and H-planes and displaying symmetrical power distribution. However, as the focus (f) increases, the gain reduces, accompanied by a significant rise in SLLs. Despite this, these focus points produce a balanced radiation distribution in the E-plane and H-plane. It is important to note that all these focus values have potential applications in scenarios where the sidelobes can effectively receive a substantial amount of power simultaneously.

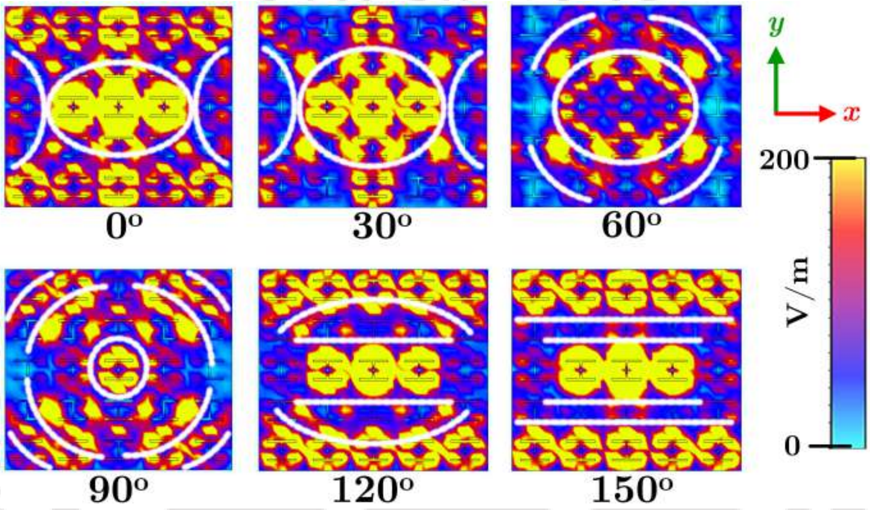

Figure 4.10: Distribution of electric field on the back side of MSSR array placed at $f = 0.93\lambda_0$ at 2.45 GHz.

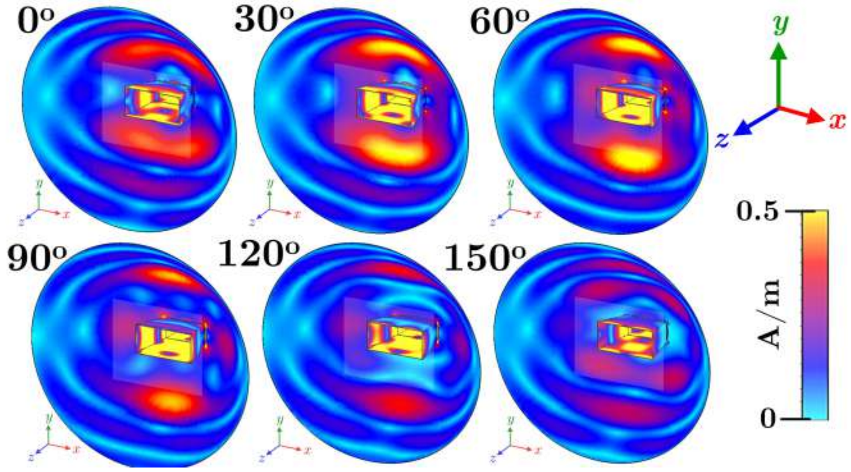

Figure 4.11: Distribution of electric field on the back side of MSSR array placed at $f = 0.93\lambda_0$ at 2.45 GHz.

Figure 4.10 depicts the electric field distribution on the back side of the MSR (Metasurface Reflector) array. A white dotted line, projected based on the dominant field, reveals a planar distribution for the E-field variation from 0° to 150° with phase. An elliptical formation is observed around the middle of the cells, with equal magnitude on the upper and lower sides. As the phase increases, the field becomes concentrated in the middle five MSR cells, while the first and fifth-unit cell rows exhibit very low values, except for the middle ones. This indicates a gradual field increment from the array centre towards the edges. Further advancement of the phase results in a concentric distribution, where points with equal amplitude are radially spaced, as demonstrated in Figure 4.10. This pattern concludes with a quasi-planar distribution, primarily concentrated in the middle three rows and slightly reduced in the uppermost and lowermost rows. At 150° phase, a perfect planar formation is observed, with identical sidelobe field distributions.

It is important to note that the reflected energy is mainly concentrated in the main lobe, evident from the surface current distributions. Interestingly, the MSR array's front and back sides follow an identical field distribution pattern for all respective phase values. The field plots on the array and surface currents on the primary dish, as shown in Figure 4.11, provide valuable information about the reflected and induced fields at various phases.

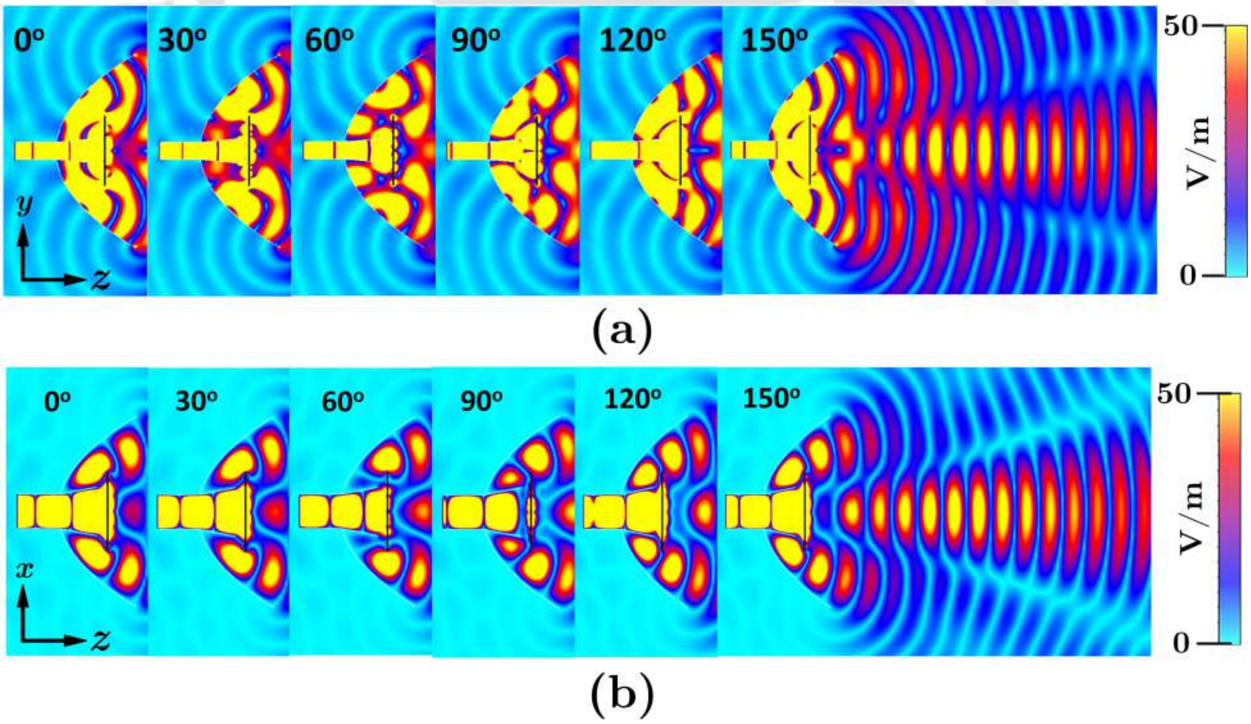

Figure 4.12: Propagation of EM wave with MSSR at $f = 0.93\lambda_0$ at 2.45 GHz in (a) E-plane and (b) H-plane.

In Figure 4.12, we observe the forward propagation of the electromagnetic (EM) wave after reflection from the MSSR and main dish in both the E-plane and H-plane. By setting the MSSR array at $f = 0.93\lambda_0$, optimal reflections are achieved, making efficient use of the depth and diameter of the dish. As the waves propagate from 0° to 150°, they exhibit non-destructive interference, resulting in a symmetrical field distribution and the formation of plane waves. These characteristics highlight the exotic directional capabilities of the antenna. As the waves exit the antenna, the amplitude distributions demonstrate constructive interference as they combine with the propagation path. The MSSR array effectively utilises the dish depth to distribute the incoming fields as planar waves at three distinct angles. This showcases the antenna's ability to manipulate and control the EM waves precisely.

4.5.2 Experiment

A conceptual proof is realised by fabricating and testing the MSSR array and parabolic dish antenna, as shown in Figure 4.13. The main dish and feed horn are constructed from a 1.2 mm thick aluminium sheet, and a WR340 standard CPR flange feeds the input to the horn illustrated in Figure 4.13a. The antenna is rotated by 90° in xoy plane to measure the radiation pattern in principal planes. Figure 4.13b,c presents the antenna in E- and H-plane, respectively. The MSSR is positioned at $f = 0.93\lambda_0$ by attaching it to a 0.8 mm thick acrylic sheet edge on the horn flaring and is depicted in Figure 4.14b. The simulation assumes free space between the horn aperture and the MSSR array. This arrangement provides an identical testing model designed in simulation, keeping minimal reflections from physical supports. The radiation characteristics are measured in an anechoic chamber facility at IIT Guwahati.

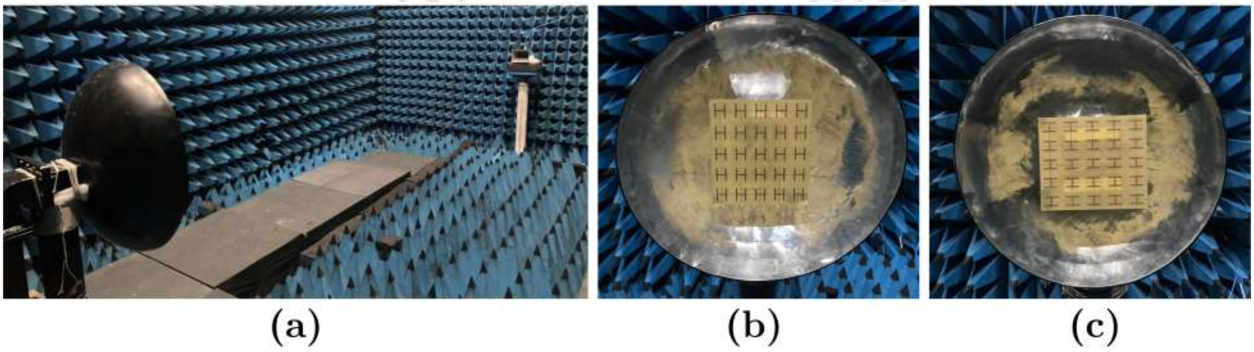

Figure 4.13: (a) Photograph of the experimental setup in an anechoic chamber to measure radiation pattern of proposed MSSR-based dual-reflector antenna. A closed view in (b) E-plane and (c) H-plane.

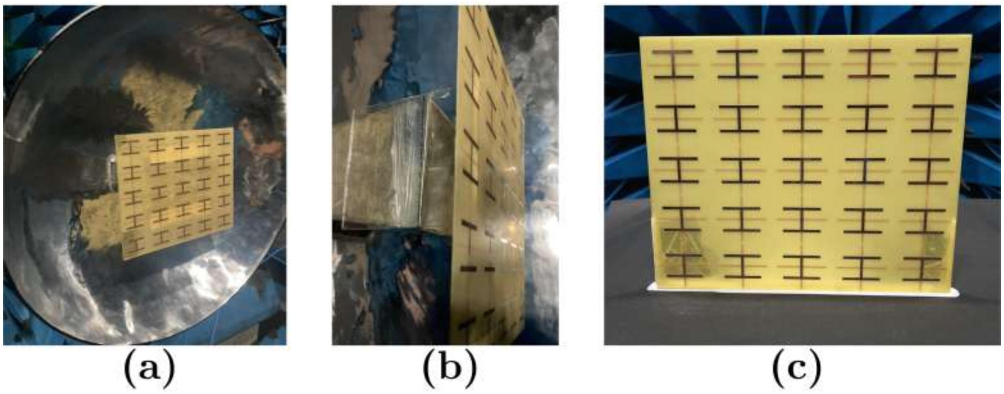

Figure 4.14: (a) MSSR dual-reflector antenna in H-plane. (b) A close view showing array positioning at $f = 0.93\lambda_0$, and (c) back view of fabricated MSSR array.

Electric field

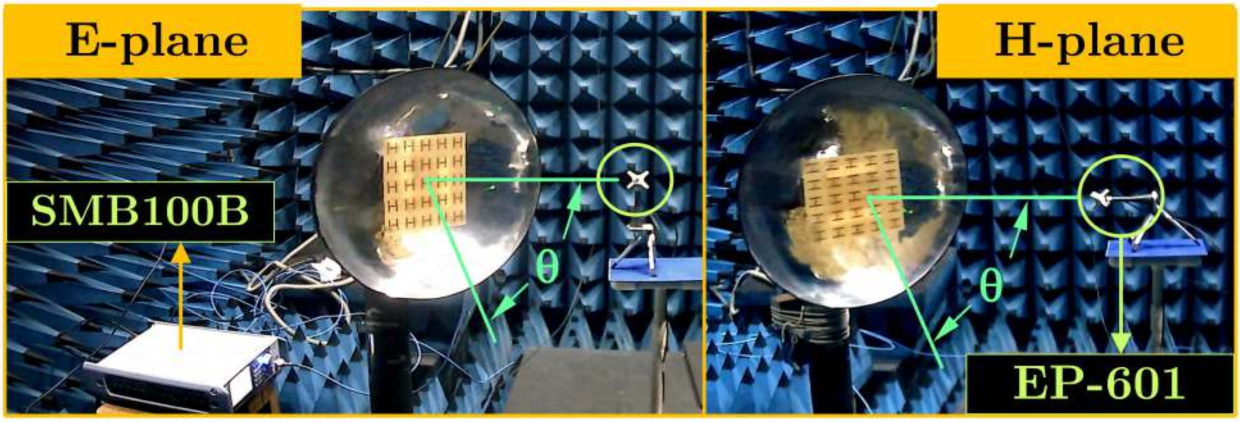

Figure 4.15: Experimental arrangement for electric field measurement in principal planes and fabricated Cassegrain antenna with proposed MSSR at $f = 0.93\lambda_0$.

Figure 4.15 depicts an electric field measurement arrangement in principal planes. To carry out the measurements, a signal generator (R&S: SMB100B) is utilised to supply 1W power, while an electric field probe (Narda: EP-601) instantaneously detects the electric field. A stepper motor is employed to rotate the probe position within the range of $-90^\circ \leq \theta \leq +90^\circ$ at distances ranging from 25 mm to 125 mm ($25 \leq R \leq 125$ mm).

The electric field variation is plotted in Figure 4.16, revealing higher field values in the E-plane compared to the H-plane. As the distance (R) increases, the field strength reduces from 17.1 V/m to 5.98 V/m in the E-plane and from 13.41 V/m to 4.43 V/m in the H-plane. Specifically, in the E-plane, at $R = 25$ cm, the measured electric field at $+\theta = +16.2^\circ$ and $\theta = -19.8^\circ$ is 15.21 V/m and 15.24 V/m, respectively. These values are lower than those in the main direction, indicating the presence of power in the side lobes. As predicted, the measured electric field exhibits significant values at respective angles due to the simulation distributions illustrated in Figure 4.9. This figure showcases the variation of the electric field concerning distance and angle, which is a critical factor for power harvesting, especially when the distance or angle of receivers is altered.

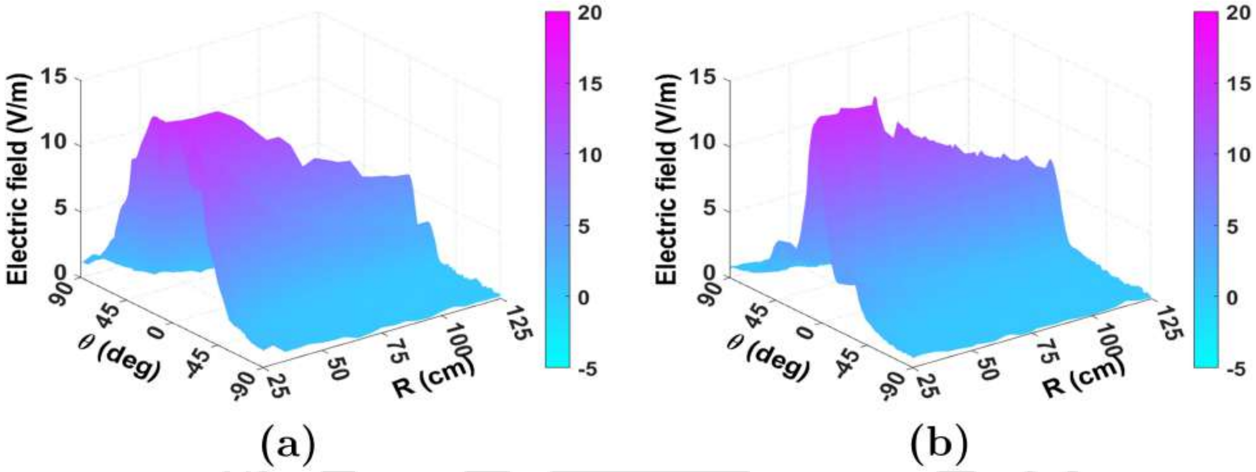

Figure 4.16: Variation of the measured electric field with θ and R at 2.45 GHz in (a) E-plane and (b) H-plane.

Radiation pattern

The Anritsu VNA, specifically the MS46122B model, was utilised to assess the radiation patterns in both E-plane and H-plane configurations, as displayed in Figure 4.13. Figure 4.17 was employed to compare the simulated and measured rectangular radiation patterns. Remarkably, the co-polarization measurements in both the E-plane and H-plane exhibited practically identical patterns as predicted by the simulations. Minor variations observed in the H-plane for $-39.6° \leq \theta \leq -16.2°$ were attributed to manual errors during the positioning of the MSSR at $f = 0.93\lambda_0$, as depicted in Figure 4.17b. Despite the ideal smoothness of the main reflector, the mechanical fabrication of a thin sheet introduced non-uniform surface finishes to maintain the correct f/D ratio, leading to a possibility of the reflected beam shifting in principal planes. Additionally, E-plane vertical strips caused a small electromagnetic interaction area for the H-field.

Nevertheless, the measured results closely aligned with the simulation predictions, displaying only minor discrepancies. The antenna's cross-polarisation arrangement in both planes followed a similar pattern. However, slight deviations were observed due to the rear part of the antenna dish resembling a PEC (Perfect Electric Conductor) sphere and the effects of multiple reflections at the dish edges and waveguide-dish joint connection. As a result, the cross-pol plots exhibited shifts or deviations at the same frequency in both planes. The study demonstrated a favourable agreement between the simulation and measurement data, providing valuable insights into the antenna's performance.

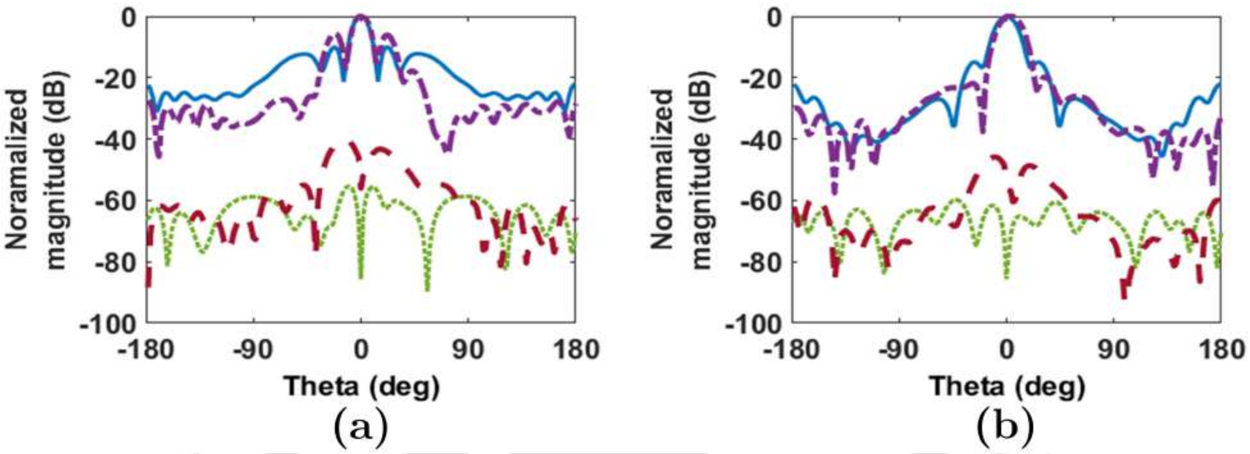

Figure 4.17: Simulated and measured radiation pattern at 2.45 GHz with proposed MSSR at $f = 0.93\lambda_0$ in (a) E- and (b) H-plane (blue: sim co-pol, magenta: mes co-pol, brown: sim X-pol, green: mes X-pol).

Table 4.2 compares the proposed antenna performance with prior designs. The highest value of gain and lowest values of HPBWs are noted. The values above show a justified choice of proposed MSSR Cassegrain antenna in microwave beaming environments.

Table 4.2: Comparison of the proposed and other high gain antennas

Ref	Frequency (GHz)	Gain (dBi)	HPBW (deg)	Antenna type
[128]	4.5	10.7	38° (E-), 42° (H-)	lens antenna
[129]	3.1	10.6	14.4° to 27.2°	no reflector
[139]	5.8	13.7	28° (E-), 38° (H-)	quasi-Cassegrain
[140]	2.4, 5.8	7.54, 6.8	–	planar reflector
[141]	1.6-1.86, 2.25-2.45	10.9, 9.5	–	corner reflector
[142]	4.2	5.8	64° (E-), 65° (H-)	patch with MSR
[143]	7.5	10.79	31°	planar reflector
[144]	5.82	9.1	29°	patch with MSR
[145]	4.7	8.65	64.6°	loop antenna
Chapter 2	2.45	10.22	43.6° (E-), 42° (H-)	lens antenna
This work	2.45	15.8	13.4° (E-), 25.2° (H-)	dual-reflector

4.6 Summary

This study introduces a novel dual-reflector antenna with a unique planar Metasurface sub-reflector array design. The antenna enables simultaneous beaming in far-field microwave wireless power transmission at 2.45 GHz[*]. At the operating frequency, the MSSR unit cell demonstrates 94.8% reflectance, 0.065% transmittance, and 5.1% absorptance. The proposed unit cell exhibits an impressive 140 MHz bandwidth between 2.38-2.52 GHz, with reflectance (R) remaining above 90% and transmittance (T) achieving a minimum of 0.065% between 2.4-2.5 GHz. When employing a planar MSSR array, the antenna achieves an optimal gain of 15.8 dBi and half-power beamwidths of 13.4° and 25.2° in the E- and H-planes, respectively. This is accomplished by adjusting the focus, i.e., the position of the MSSR array relative to the feed horn aperture.

The measurements indicate that the electric field values at $\theta = -19.8^\circ, 0^\circ, 16.2^\circ$ are 15.24, 17.1, and 15.21 V/m, respectively, suggesting nearly equal values in the main and sidelobes simultaneously for $F = 0.93\lambda_0$. With the proposed methodology and bit-coded MS (Metasurface), this novel dual-reflector antenna opens the potential for selective beaming and enhanced wireless power transmission applications in the future[†].

---

[*] **Shashank. S. Kulkarni**, Amarnath Kumar, Anurag R. Lambor, Sisir Kumar Nayak, and D. Senthil Kumar, "A Planar Meta-Surface Sub-Reflector-Based Cassegrain Reflector System for Transferring and Harvesting of Power and Energy," Grant No.:433790, Grant date: 06/06/2023, twenty years from 27/10/2022.

[†] **Shashank. S. Kulkarni**, Amarnath Kumar, Anurag R. Lambor, and Sisir Kumar Nayak, "Planar Metasurface Sub-reflector based Dual-reflector Antenna for Multi-directional beaming," AEU-Int. J. Electron. Comm., doi: https://doi.org/10.1016/j.aeue.2023.154621.

Chapter 5

Planar MSR antenna radiation pattern prediction using RFR-ML

Overview

This chapter introduces an innovative machine learning approach utilising Random Forest Regression (RFR) to predict the radiation characteristics of a planar metasurface reflector (PMSR) antenna. The RFR model is trained using key PMSR parameters at 2.45 GHz, focusing on power flows and radiation properties. To validate its accuracy, an experiment is conducted with PMSR fed by the patch at $d = 0.6\lambda_0$ and compared the RFR and CST results, revealing close alignment with minimal discrepancies. This novel method proves invaluable for assessing antenna radiation properties in scenarios with non-line-of-sight or misaligned receivers, serving as a foundational study and design reference for lightweight, planar mobile reception reflector antennas.

5.1 Introduction

Planar metasurface reflector (PMSR) antennas have emerged as a promising technology for next-generation wireless communication systems. With the increasing demand for compact and efficient antennas in modern wireless networks, PMSRs have gained significant attention. These antennas manipulate electromagnetic (EM) waves, offering advantages such as wide bandwidth [146] and low-profile designs [147], high gain [148, 149], and beam scanning capabilities [150]. The unit cells are designed with unique properties, such as resonant or binary coding-based elements [151], that enhance radiation properties [140].

To optimise the radiation properties of a reflector antenna, accurate modelling of its electromagnetic behaviour is essential. This is particularly challenging since the performance of these antennas is highly sensitive to the geometrical parameters and arrangement of the unit cells. To address this issue, machine learning (ML) techniques, such as random forest regression (RFR), have been employed to predict and optimise the radiation properties of PMSR. It combines the principles of ensemble learning and decision trees. It can be used to establish a nonlinear mapping [152] between the input parameters of a PMSR and its corresponding radiation properties. It enhances diversity among trees by growing them from different training data subsets, reducing correlations, and ensuring computational efficiency [153]. This diversity increases RFR's stability, making it robust against slight variations in input data [154].

Bagging also provides noise immunity, generating non-correlated trees through distinct training samples [155]. During each regression tree's construction in the bagging process, a new training set (bootstrap samples) is created by randomly selecting data with replacements from the original dataset. It can adapt various input parameters and non-linear relationships to predict antenna behaviour in real-world conditions. The ensemble of decision trees prevents overfitting and improves prediction accuracy, producing reliable results. The RFR can substantially reduce the time and resources required to conduct tangible experiments or lengthy simulations.

Therefore, this chapter presents a novel use of the RFR-ML study that predicts the radiation properties of PMSRs for different focus points. Utilising a patch antenna at the focus, the system attains 6.12 dBi gain at 2.45 GHz and is greater than the patch with a gain of 2.78 dBi during measurement. A concentrated field distribution is observed at the near-field boundary and in the far-field, indicating optimum reception.

5.2 Problem formulation

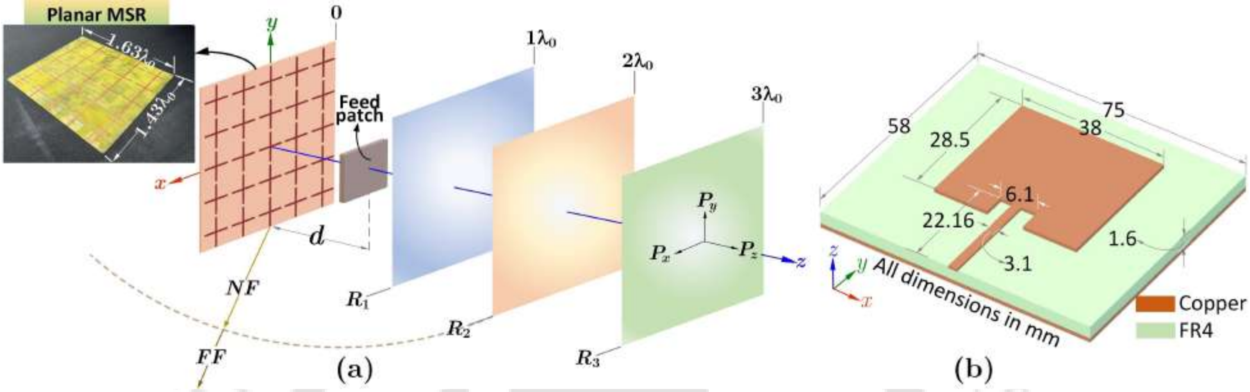

Figure 5.1: Schematic of the problem formulation for RFR prediction of patch-fed PMSR antenna.

The receiver's position directly impacts antenna radiation in microwave far-field WPT systems. Even with the receiver in line of sight, free space losses and undesired reflections can reduce beam strength [156]. However, fitting a large receiving antenna onto a lightweight mobile device is difficult. PMSR with a lightweight shape can be integrated into the current system for optimal reception. Figure 5.1a illustrates the problem formulation, where a patch antenna feeds the PMSR of maximum dimension $D = 2.17\lambda_0$. The distance $(= d)$ at which the field concentrates is crucial in obtaining the gain, half-power beam widths (HPBWs) and side lobes. This study uses the planar metasurface sub-reflector (MSSR) in Chapter 4 as PMSR to design a lightweight mobile receiver.

For reliable predictions by RFR-ML, the power flow in the radiative near-field, at the far-field boundary and in the far-field is analysed. Based on the $D = 2.17\lambda_0$ of the PMSR, near-field $(NF = 0.63\sqrt{D^3/\lambda_0} \approx 2\lambda_0)$ is obtained. Therefore, far-field radiation properties and power distribution calculated as $P_t = \sqrt{P_x^2 + P_y^2 + P_z^2}$ (W/m^2) in the xoy plane at $R_1 = 1\lambda_0$, $R_2 = 2\lambda_0$, and $R_3 = 3\lambda_0$ from PMSR is considered. These distinct spatial values of R in the NF, at the boundary, and in the far-field $(FF = 2D^2/\lambda_0)$ provide input data points for accurate prediction. The feature extraction process for a patch-fed PMSR involves employing EM modelling over a distance $(= d)$ range.

This comprehensive approach allows a thorough analysis of the PMSR's behaviour in the near-field and far-field regions. In the next step, the power distributions in the xoy plane at three distinct positions are studied, denoted as R_1, R_2, and R_3. These power distribution profiles are crucial as they serve as the primary input data for the RFR-ML model, a technique designed to extract valuable insights from the EM data. Furthermore, we also extract and visualise the radiation pattern of the PMSR in its principal planes as a function of d. This approach ensures a detailed and holistic examination of the PMSR's behaviour under varying conditions, providing valuable information for further analysis and optimisation.

Figure 5.1b illustrates the geometry of the patch antenna used as a feed. The patch antenna is excited through a microstrip line, resulting in a y-polarised electric field consistent with the electromagnetic modelling of the unit cell and PMSR. It is excited through a microstrip line, resulting in a y-polarised electric field consistent with the EM modelling of the unit cell and PMSR. It exhibits 3.1 dBi gain with 93.8° and 79.8° HPBW in E- and H-plane, respectively.

5.3 RFR-ML approach

After suitable training, RFR-ML makes it feasible to parameterise and model complex non-linear functions with limited parameters. At its core, RFR is a collection of decision trees, each trained on a random subset of data and features. This ensemble approach mitigates over-fitting and captures complex relationships within the data, making it well-suited for modelling the behaviour of PMSR antennas. In an environment where even slight parameter variations can lead to significant performance differences, the ability to make accurate predictions is paramount. The interpretability of RFR allows antenna engineers to identify key factors influencing performance, aiding in the decision-making process. Proper feature selection, dataset pre-processing, training and validation are vital steps in harnessing the full power of RFR.

The RFR prediction employed in the proposed study is shown in Figure 5.2. The RFR model offers prediction by constructing multiple de-correlated decision trees. Each tree in RFR is grown with a randomised subset of predictors. RF uses L tree-structured base

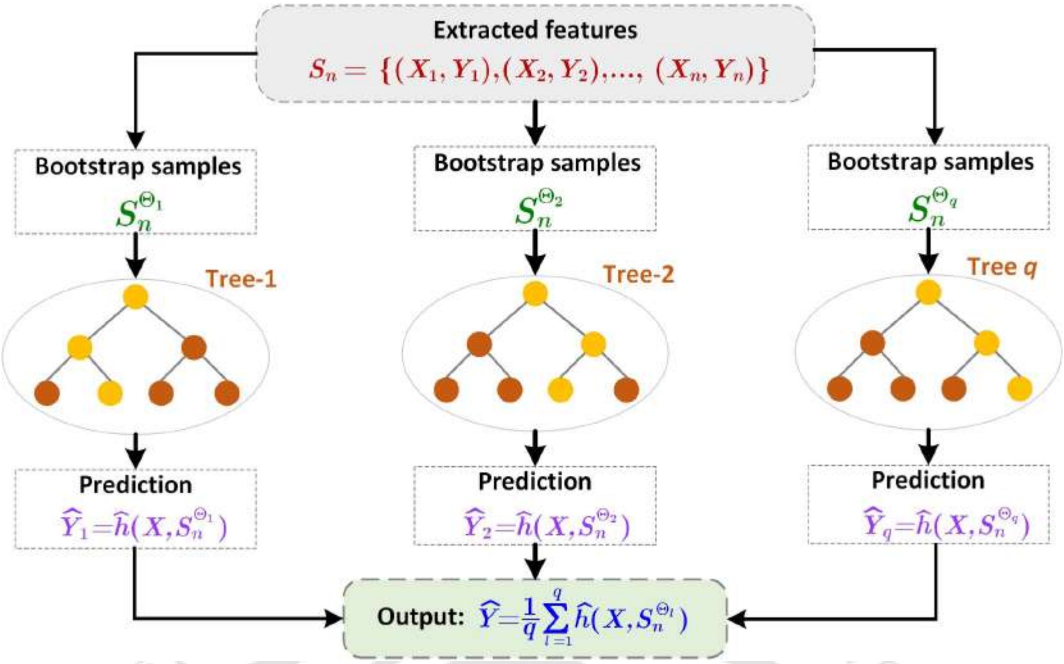

Figure 5.2: Schematic of random forest regression ML method.

classifier $h(X, \Theta_k)$, where $k = 1, \ldots, L$, Θ_k is an independent, identically distributed random vectors with X as an input vector. It is an ensemble method combining all the generated decision trees using a bootstrap aggregation algorithm. It reduces the prediction variance, thereby improving the prediction performance. Here, the scalar output Y and the training set (S_n) containing n observations is expressed as [152],

$$S_n = \{(X_1, Y_1), .., (X_n, Y_n)\}, X \in \mathbb{R}^m, Y \in \mathbb{R} \tag{5.1}$$

RFR can be built by randomly sampling a feature subset for each decision tree and by randomly sampling a training data subset. Randomly selecting n observations with replacement from S_n creates a bootstrap sample with a probability of $1/n$. It selects several bootstrap samples $(S_n^{\Theta_1}, \ldots, S_n^{\Theta_q})$ and applies the previous tree decision algorithm to these samples to construct a collection of q prediction trees $\hat{h}(X, S_n^{\Theta_1}), ..., \hat{h}(X, S_n^{\Theta_q})$. The ensemble produces q outputs corresponding to each tree, $\widehat{Y}_1 = (X, S_n^{\Theta_1}), ..., \widehat{Y}_q = (X, S_n^{\Theta_q})$. Then, the aggregation is performed by averaging the outputs of all trees, and the estimated output Y is obtained by [152],

$$\widehat{Y} = \frac{1}{q}\sum_{l=1}^{q} \widehat{Y}_l = \frac{1}{q}\sum_{l=1}^{q} \hat{h}(X, S_n^{\Theta_l}) \tag{5.2}$$

5.4 Results and discussion

The input and output data i.e. extracted features, exhibit complex relations between parameters, are depicted in Figure 5.2. The d plays a crucial role, and the variation alters the radiation properties. The MSSR presented in [6] suggests that altering the focus can impact the power distribution in both the sidelobes and the main direction. Also, the half-power beam widths in both planes can be changed by varying the focus. The geometry and finite dimensions of the PMSR and feed patch lead to a substantial change in output. In EM modelling, the boundary conditions are imposed to yield the radiation, and the performance of the fabricated prototype is measured in an anechoic chamber.

To comprehensively study the principal planes' resultant power distribution and radiation patterns, we vary the distance ($= d$) as depicted in Figure 5.1. For the training set S_n, the extracted parameters for $0.1\lambda_0 \leq d \leq 1\lambda_0$ are utilised. The M feature vectors, $\{x_1, x_2, \ldots, x_m\}$, and their outputs, $\{y_1, y_2, \ldots, y_m\}$, can be obtained from each of the simulation results to form a training dataset $\{(x_i, y_i), i = 1, 2, \ldots, M\}$ used to construct a random forest (RF) model. At the end of this training process, a prediction function of tree base classifier $\hat{h}(X, S_n)$ is constructed over S_n.

5.4.1 Simulation

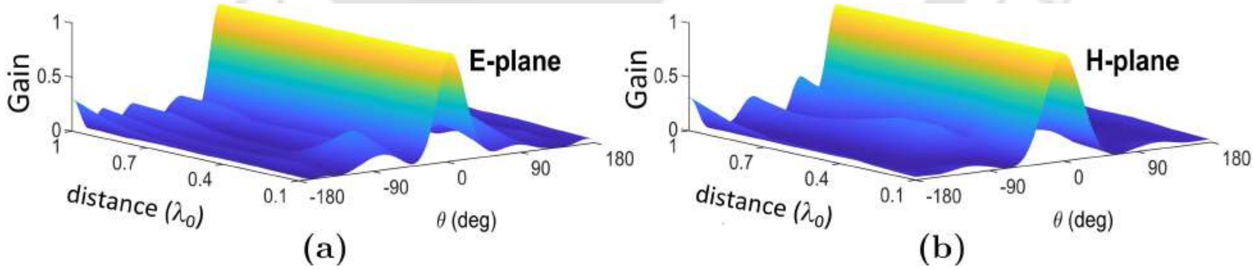

Figure 5.3: Distribution of gain at 2.45 GHz for $0.1\lambda_0 \leq d \leq 1\lambda_0$ in (a) E- and (b) H-plane.

The feature extraction of a patch-fed PMSR is carried out by EM modelling for $0.1\lambda_0 \leq d \leq 1\lambda_0$. The power distributions in the xoy plane obtained at R_1, R_2, and R_3 are the input to the RFR-ML model. Also, the radiation pattern in the principal planes is extracted for the d and is plotted in Figure 5.3. By placing the patch close to the PMSR along the z-axis and d, the main lobe in the E-plane shifts by 5°. When the axis passes through the substrate's centre, the patch exhibits asymmetry in the E-plane due to the microstrip feed line at the bottom. The major radiating structure is in the upper half and a shift is occurred.

For $d = 0.25\lambda_0$, the field exhibits side lobes in the E-plane due to improper reflection from the PMSR. As d is increased beyond $0.4\lambda_0$, the regions R_1, R_2, and R_3 show concentration along the main axis with increased gain. The side lobes in the E-plane are reduced as the patch has more radiating area. This distance also produces H-plane side lobes as the PMSR cells in the x-axis are at higher radii values of the spherical waves radiated by the feed patch.

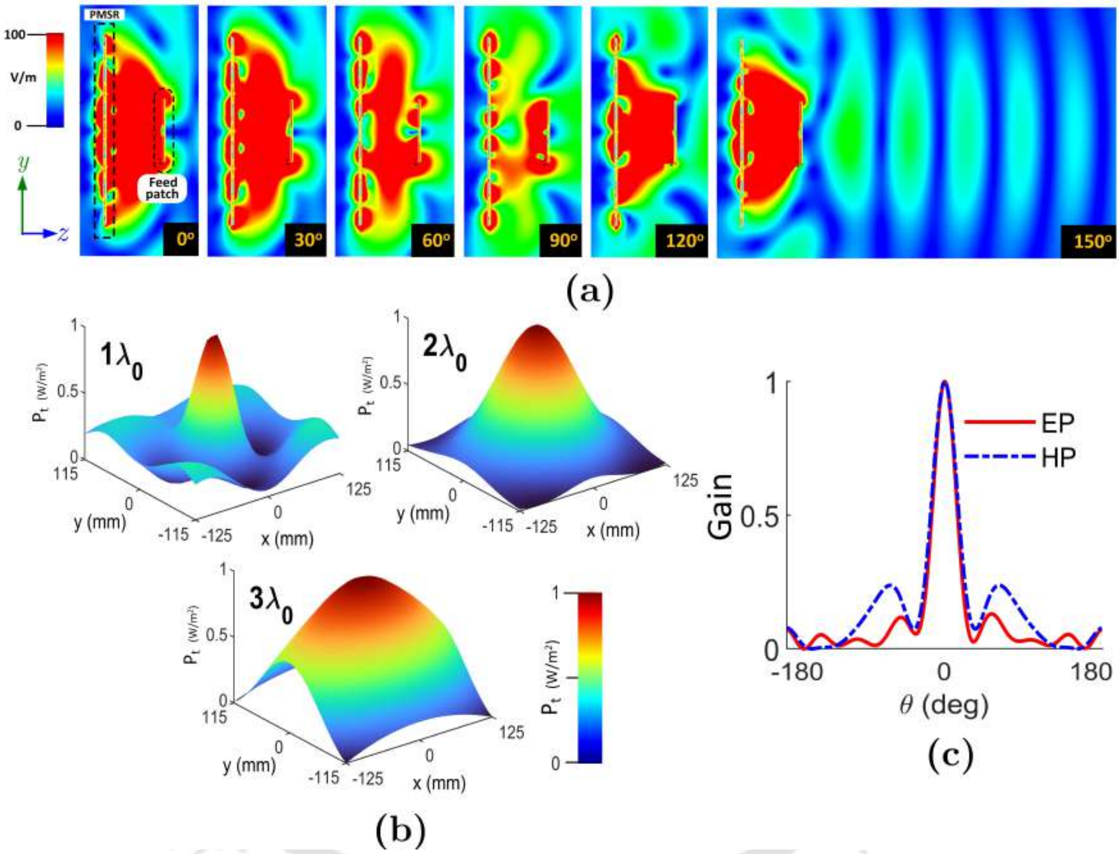

Figure 5.4: (a) Propagation of electric field at 2.45 GHz in the *yoz* plane. (b) Distribution of $P_t(W/m^2)$ at R_1, R_2, and R_3 for $d = 0.55\lambda_0$. (c) Distribution of gain at 2.45 GHz.

At $d = 0.55\lambda_0$, a maximum gain is obtained, showing the optimum power reception of the incident beam. This distance is approximately half the wavelength, offering sufficient space for wave propagation towards PMSR and the reflection is displayed in Figure 5.4. The H-plane exhibits a greater length compared to the E-plane. The difference in spherical distance in the principal planes from the feed patch and asymmetry due to the feed line in the y-axis result in a difference in the path length of the impinging wave. The length difference makes reflected fields produce an optimum gain in their respective planes compared to other values of d. When this distance is reduced, it decreases the effective radiating area available to the patch. This alteration affects the electromagnetic field, primarily due to the rectangular geometry of the PMSR. Conversely, increasing the distance leads to an extended travel time for electromagnetic waves to reach the PMSR and reflect.

Furthermore, during propagation towards the z^+ axis, there is a possibility of interference from the incoming wave originating from the patch, potentially causing reflections in undesired directions. Maintaining the half-wavelength distance provides a sufficient region for radiated and reflected EM waves, thus mitigating losses in the main direction and is presented in Figure 5.4b,c. Notably, the patch and PMSR geometry are pivotal in optimising performance at this focal point. This study aims to comprehensively investigate the influence of change of focus on radiation properties, emphasising the complex relationship between geometry and performance.

An identical radiation distribution is observed when the patch is at $d = 0.85\lambda_0$ and $d = 1\lambda_0$. The field at $d = 1\lambda_0$ and R_1 is the field radiated by the patch and is maximum at the origin. After reflection from the PMSR, the interference between the feed and reflector field dominantly affects the gain. This shows the reflector's symmetry in the E- and H-plane, significantly impacting the radiation field. It is seen that the focus values between $0.4\lambda_0$ and $0.85\lambda_0$ result in a positive gain, lower side lobes, and an increased half-power beamwidth.

The dataset of 24849 antenna radiation distribution points extracted from CST is provided to the RFR model. It produces 100 bootstrap sample decision trees for $\widehat{Y}$ in (5.2), linking the input X to the power (P_t) at R_1, R_2, and R_3, and gain in the principal planes. For this, 70% data is used for the training and 30% is used for test and validation. Figure 5.5a illustrates predicted E- and H-plane radiation patterns. The predicted radiation for $d = 0.3\lambda_0$ matches well with the CST simulations. The field is not properly configured at $d = 0.25\lambda_0$, resulting in reduced gain. Results between $d = 0.55\lambda_0$ and $d = 0.7\lambda_0$ perfectly align with the ML predictions at $d = 0.6\lambda_0$, showing a positive gain in the radiation field. A good agreement is observed between CST and RFR predictions at this focus. Moving patch to $d = 0.9\lambda_0$, the predicted fields differ in sidelobe, which occurs mainly due to the large distance. The patch at $d = 0.9\lambda_0$ produces side lobes as the PMSR cells in the x-axis are at higher radii values of the spherical waves radiated by the feed patch.

A close match between CST and RFR is observed for the power at R_3 as plotted in

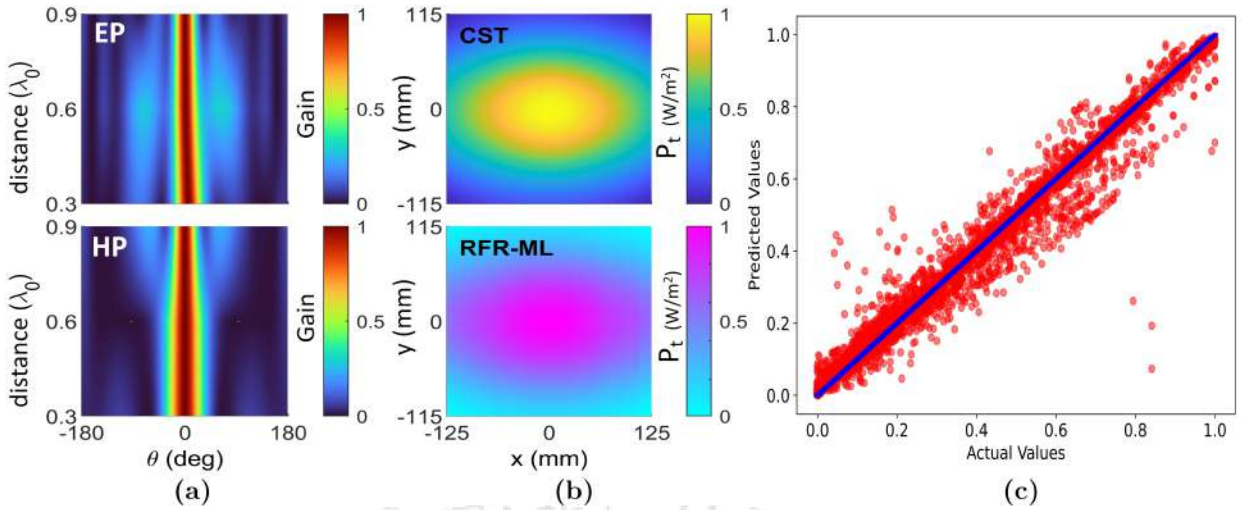

Figure 5.5: (a) Distribution of gain at 2.45 GHz for $d = 0.3\lambda_0$, $0.6\lambda_0$, and $0.9\lambda_0$. (b) P_t (W/m^2) at R_3 for $d = 0.6\lambda_0$. (c) Variation of actual and predicted values in the RFR model.

Figure 5.5b, and the actual values used to predict are shown in Figure 5.5c. The prediction accuracy obtained is 95.47% with a root mean square error (RMSE) of 0.051. This occurs as the CST uses a full wave electromagnetic solution method to estimate the fields and the radiated components; however, RFR-ML uses training data with limited extracted features prior to prediction. These disparities are enhanced when the patch is close or far from the focus. Despite these inconsistencies, CST and ML findings are highly aligned due to low error and high precision. This shows that RFR-ML can reliably forecast far-field properties of PMSR models.

This focus adjustment can be valuable for future applications involving power in side lobes or multi-directional beaming. The power flow at R_1, R_2, and R_3 provide insights into how the field propagates and is radiated by the PMSR for different d. For machine learning predictions, we propose $d = 0.3\lambda_0$, $0.6\lambda_0$, and $0.9\lambda_0$ as outputs. The selection of these points covers an entire d range and its effects on magnitude. Based on $d = 0.55\lambda_0$ and $0.7\lambda_0$, the ML for $d = 0.6\lambda_0$ shall produce a positive gain and reduced HPBWs.

5.4.2 Experiment

To ensure a fair comparison between CST and RFR results, we fabricated the PMSR and patch antenna and assessed their radiation properties at $d = 0.6\lambda_0$. It is fabricated using a conventional PCB design process and has a 200 mm width and 175 mm length. The feed patch antenna is kept at $0.6\lambda_0$ focus by attaching it to a stable 3D-printed polylactic acid

(PLA) stand. The measurements are performed in an anechoic chamber with a 10.6 dBi gain pyramidal horn antenna.

The highest gain with minimal differences between RFR and CST values is observed during measurements. Figure 5.6a depicts the experimental setup used in an anechoic chamber. The radiation pattern of the PMSR is measured using Anritsu VNA (MS46122B). In Figure 5.6b, the shift in the E plane's main lobe is attributed to the precise placement of the patch antenna at the correct focus. The variation between $d = 0.55\lambda_0$ and $d = 0.6\lambda_0$ is minimal, making results nearly identical with $d = 0.55\lambda_0$ and exactly matching $d = 0.6\lambda_0$. During measurement, the beam is shifted to -3° in the E- and 2° in the H-plane. This response is attributed to the fabrication tolerances, focal length shifts during feed patch installation, and cable and instrument noise. Variation of magnitude between $\theta = \pm 30^\circ$ shows a focused beam compared to a typical patch antenna.

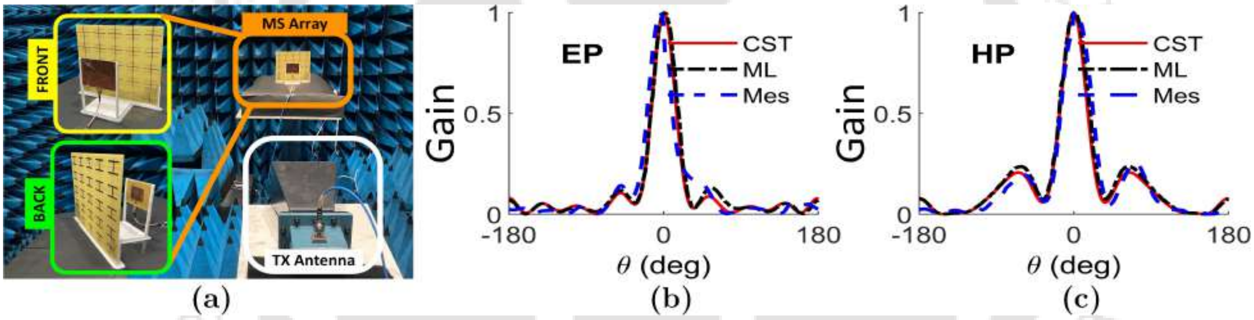

Figure 5.6: (a) Experimental setup to measure the radiation pattern of PMSR with feed patch at $d = 0.6\lambda_0$. Variation of gain for CST, RFR, and measurements at 2.45 GHz in (b) E- and (c) H-plane.

Figure 5.6 results affirm that measurements align with predictions, endorsing the suitability of our suggested RFR-ML approach for reflector design methodology. The measured gain is 6.12 dBi during experiments, with 32° and 36.4° HPBWs in the E- and H-plane. Compared with CST and ML, it exhibits a 1.14 dBi and 0.97 dBi reduction, respectively. The CST results are 28.8° and 32.4° for HPBWs in the E- and H-plane, whereas ML indicates 30° and 35°. Measurement results show reduced values for gain and HPBWs due to fabrication tolerances and losses incurred by connectors and cables. Nevertheless, the proposed RFR-ML methodology is well-suited for designing the focus point and PMSR for mobile receiving applications. A system comprising a high-power microwave transmitter and a proposed PMSR at the receiving side shall improve the efficiency, providing more RF input to the rectifier.

Table 5.1: Comparison of the proposed RFR-ML method and PMSR characteristics with prior articles

Ref	Frequency (GHz)	Reflector dimension ($=D$)	Gain (dBi)		
			simulation	measurement	ML
[147]	2.1, 5.8	144.5×144.5 mm^2	2.7 5.5	2.5 (@2.1 GHz) 5 (@5.8 GHz)	-
[149]	2.45	200×200 mm^2	9.2	8.5	-
[157]	2.45	NA	2.87	2.80	-
This work	2.45	200×175 mm^2	7.26	6.12	7.09

Table 5.1 presents a comparative analysis between proposed PMSR characteristics and the RFR-ML method with prior works. The proposed PMSR demonstrates a noteworthy gain while maintaining comparable reflector dimensions. It is noted that prior designs relied on simulations and measurements inside the anechoic chamber, whereas the proposed methodology introduces a novel approach to predict the radiation pattern using RFR-ML. The close alignment between ML predictions and simulations suggests the adaptability and cost-effectiveness of RFR-ML in antenna design. The proposed PMSR, characterised by high gain and a compact, lightweight geometry, can be conveniently installed on mobile vehicles for efficient power reception.

The RFR method employs a tree-based regression algorithm wherein the input and output relations are predicted based on the training of the extracted features. The proposed method can still be applied to other types of PMSR and feed wherein, the prior input and output relationship is defined during training. With an appropriately trained RFR tree for the reflector and feed configuration with input and output as a function of the geometrical design parameters, accurate predictions can be made.

This chapter leverages the power of ML to advance the field by employing RFR to predict antenna radiation properties, particularly near and far-field regions. Training the algorithm through RFR-ML facilitates easier predictions and significantly reduces computational time, making it a cost-effective solution. This approach is a noteworthy fusion of electronics and ML, paving the way for predictive modelling and design optimisation in electronics engineering. It showcases the potential effectiveness and efficiency of ML in the domain of emerging WPT technologies.

The significance of this work lies in its ability to reduce computation time and associated costs. It streamlines the design and analysis process using a trained ML model for accurate predictions. This is particularly valuable when exploring different PMSR configurations, feeds, distances, field regions, misalignments, and polarisation studies. his method leverages the power of machine learning to advance the field. It employs RFR to predict antenna radiation properties, particularly near and far-field regions. Training the algorithm through RFR-ML facilitates easier predictions and significantly reduces computational time, making it a cost-effective solution. This approach is a noteworthy fusion of electronics and ML, paving the way for predictive modelling and design optimisation in electronics engineering. It showcases the potential effectiveness and efficiency of ML in the domain of emerging WPT technologies. The following are key points of the analyses:

- Versatility: The RFR-ML approach presented in this thesis will still be applicable to other configurations of reflector and antenna feeds. An ML model trained with input-output dependencies can be used to predict the response of the system as a function of various non-linear conditions, distances, field regions, and polarisation studies.
- Cost-effective: While computer simulations are widely used for antenna design, they can be computationally intensive and time-consuming. The proposed RFR-ML method, once trained, and validated, offers an efficient and rapid means of predicting radiation properties, saving both time and computational resources.
- Experimental approach: The performance is studied by fabricating a prototype. It is observed that EM modelling, predictions using proposed RFR-ML, and experiments show minimal discrepancies in the output. This demonstrates the accuracy and reliability of the trained ML method, paving the way for its potential adoption in real-world antenna design.

5.5 Summary

This chapter introduces a novel RFR-ML method for predicting the radiation properties of PMSR antennas. After training on power flows and radiation properties in principal planes, the extracted parameters serve as input for RFR-ML. Based on the range of d, the far-field at $0.3\lambda_0$, $0.6\lambda_0$, and $0.9\lambda_0$ is predicted. For comparison, an experiment with PMSR fed by the patch at $d = 0.6\lambda_0$ is performed to estimate the difference in the RFR and CST. The observed gain on a measurement basis is 6.12 dBi with 32°(E-) and 36.4°(H-) HPBWs. The far-field plots match closely with the CST and RFR with minimal variations in the E- and H-plane[*]. The proposed compact PMSR can be attached to ground platforms, e.g. robots and rovers, and due to its lightweight, it can also be installed on drones, aerostats and similar areal vehicles. This novel method serves as a design guide for determining radiation patterns of a reflector antenna, wherein the d determines the received power.

---

[*] **Shashank S. Kulkarni**, Niraja P. Sanghai, Chayanika Baishya, Amarnath Kumar, and Sisir Kumar Nayak, "Random Forest Regression for Radiation Pattern Prediction of Planar Metasurface Reflector Antenna", AEU - International Journal of Electronics and Communications, 2023, 155018, ISSN 1434-8411, https://doi.org/10.1016/j.aeue.2023.155018.

Chapter 6

Conclusion and future work

Overview

This chapter summarises various studies carried out for far-field microwave WPT at 2.45 GHz. The objectives are addressed with the appropriate use of MM as a lens and a reflector. Including the same at the Tx and Rx sides enhanced the output regarding system efficiency or distance. Also, the planar MS sub-reflector of the Cassegrain antenna can direct the beam in distinct angles. This study can be used in the simultaneous powering of small circuits. It also explains the future far-field charging applications for robots, drones, and aerostats. The space-based solar power is a demand for future green energy and can be fulfilled with the justified use of an MM array and rectifier.

6.1 Summary of the present work

A microwave WPT system is highly dependent on transmission medium and path losses during propagation. The system efficiency is related by the Friis transmission equation, which shows that for a constant distance, input power, and frequency, the output can be enhanced by increasing the antenna gains. This is accomplished by including MMs that exhibit perfect transmission and reflection at the operating frequency. Three main chapters describe methodologies to enhance the efficiency and achieve directional beaming in the microwave regime. The work is summarised as follows:

- The concept, needs, and challenges in far-field microwave WPT are discussed in Chapter 1 with systems employing MM and their components. Based on the literature review and current challenges, objectives are formulated for the proposed MM-employed WPT applications.

- A 2.45 GHz far-field WPT system using GRIN MM with an induced magnetic dipole is constructed and tested for 1 m. Including the MM at $2.5\lambda_0$ from the Tx aperture results in 32.6% system efficiency, and is higher by 5.69% compared to a system without MM. In principal planes, HPBW is reduced by 16 degrees on average to confine the beam. Since MM always increases system efficiency η_{sys}, the proposed method is ideal for long-range WPT applications with a high power supply.

- The design, fabrication, and experimental demonstration of electric field improvement at $R = 3$ m using a novel MM array at the Tx and MM reflector at the Rx side. The gain of the Tx and RX side is improved by 3.52 and 3.19 dBi, respectively. With 800 W input power and $R = 3$ m, the electric field received is 354.33 V/m and is doubled compared to a conventional system without MM.

- A planar metasurface sub-reflector (MSSR) based dual-reflector antenna operating at 2.45 GHz. The position of the novel MSSR array can be varied to adjust the gain and power in SLL. With 97.4% reflection of the unit cell, the experimental results show 15.8 dBi gain and 13.4°, 25.2° HPBW in E- and H-planes.

- A machine learning approach for radiation pattern prediction of planar metasurface reflector antenna. The experimental results show minimal discrepancies compared to results obtained by EM modelling and predictions by RFR-ML. The measured gain at 2.45 GHz is 6.12 dBi, obtained by computer simulation is 7.26 dBi, and by ML prediction is 7.09 dBi.

- This shows exotic capabilities of MMs for reliable performance of WPT system at 2.45 GHz. To achieve high gain, low beamwidth, and multi-directional beaming, proposed MM arrays at their respective focus can be opted. An enhancement in the field in main and distinct angles will reduce the charging time or allow increased distance compared to systems without MM.

6.2 Suggestions for the future work

In the near future, WPT will have various applications in day-to-day life. One of the most famous is the use of inductively coupled smartphone chargers. Along with domestic applications, industrial applications include powering robots, UAVs, and aerostats for defence purposes. Solar-based power transfer is also being studied so that renewable energy sources can be utilised in practice.

6.2.1 WPT to UAV and robots

Let a UAV fly and capture real-time data near borders for defence administration. It runs on a battery that gives electrical power to propellers, cameras, and communication systems on board. When the battery drains below a threshold level, the UAV will be autonomously guided to the nearest charging station. It will hover at a particular height and receive microwave power when reached. The patch antenna connected at its bottom will collect the energy, and the battery will be charged after rectification and filtration of the 2.45 GHz frequency signal. The same methodology for powering the batteries of the robots and aerostats is adopted using MMs as a focusing lens that achieves beam convergence.

In Chapter 3, it is shown that the electric field at 3 meters is improved by double. As a result, the power density at the respective distance is also enhanced. The use of compact planar reflectors and feed antennas such as slotted patches or fractals makes the system lightweight and can be easily installed on land or aerial vehicles. A high-power magnetron attached to a high gain antenna and MM GRIN lens positioned at focus will result in an even more concentrated field aimed for directional beaming.

6.2.2 Solar based WPT

In the future, to solve the energy crisis, which is today mainly based on non-renewable sources, a new method of transferring power from space-based satellite systems is being studied. The satellite, when placed in space, works on the power collected by the solar radiations that fall on panels attached to it. A large array of solar panels in the space will collect the solar irradiation and convert it to DC power. The same will be inverted and given to the AC-operated high-power microwave generator. A highly directional antenna will direct the power towards the earth station through an MM lens. The MM lens further narrows the beam that travels to the receiving station on the earth. The rectenna array installed on the earth station will rectify and filter the 2.45 GHz power signal, and DC is available for the load.

List of Publications

Patents

Granted

- **Shashank. S. Kulkarni**, Amarnath Kumar, Anurag R. Lambor, Sisir Kumar Nayak, and D. Senthil Kumar, "A Planar Meta-Surface Sub-Reflector-Based Cassegrain Reflector System for Transferring and Harvesting of Power and Energy," Grant No.:433790, Grant date:06/06/2023, twenty years from 27/10/2022.
- **Shashank. S. Kulkarni**, Amarnath Kumar, Niraja P. Sanghai, Anurag R. Lambor, Sisir Kumar Nayak, and D. Senthil Kumar, "An Electric Field Enhancement System For Automated Mobile Vehicle Charging," Grant No:437297, Grant date:05/07/2023, for twenty years from 27/10/2022.
- Baghel Amit Kumar, **Kulkarni Shashank Satish**, Nayak Sisir Kumar, and D. Senthil Kumar, "Parabolic Pyramidal Horn Antenna," Grant No:385322, Grant date:28/12/2021, for twenty years from 19/01/2018.
- Rohith Sangineni, **Kulkarni Shashank Satish**, and Nayak Sisir Kumar, "Non-intrusive and Non- destructive System and Method for Condition Assessment of Transformer Liquid Insulation," Grant No.: 503817, Grant date: 27/01/2024, for twenty years from 11/03/2022.

Published

- **Shashank S. Kulkarni**, Amit Kumar Baghel, Sisir Kumar Nayak, and D. Senthil Kumar, "Far-field Wireless Power/Energy Transfer/Harvesting to/for Manned and/or

Unmanned Systems using Metamaterial," Indian patent no.:201931023905, published on 12/07/2019.

- Amit Kumar Baghel, **Shashank S. Kulkarni**, Sisir Kumar Nayak, and D. Senthil Kumar, "Aperture Matched Parabolic Pyramidal Horn Antenna," Indian patent no.: 201931023910, published on 12/07/2019.

Journals

- **Shashank S. Kulkarni**, Niraja P. Sanghai, Chayanika Baishya, Amarnath Kumar, and Sisir Kumar Nayak, "Random Forest Regression for Radiation Pattern Prediction of Planar Metasurface Reflector Antenna", AEU - International Journal of Electronics and Communications, 2023, 155018, ISSN 1434-8411.
- **Shashank S. Kulkarni**, Amarnath Kumar, Anurag R. Lambor, and Sisir Kumar Nayak, "Planar Metasurface Sub-reflector based Dual-reflector Antenna for Multi-directional beaming," AEU-Int. J. Electron. Comm., Volume 164, 2023, 154621.
- **Shashank S. Kulkarni**, A. K. Baghel, and Sisir Kumar Nayak, "Graded Refractive Index Metamaterial for Enhanced Far-field Wireless Power Transfer Efficiency in S-band," AEU-Int. J. Electron. Comm., Volume 138, 2021, 153859, ISSN 1434-8411, https://doi.org/10.1016/j.aeue.2021.153859.
- Baghel, AK, **Shashank S. Kulkarni**, Nayak, SK.,"A high gain aperture match parabolic horn antenna with stable phase center and higher FBR in S-band". Microw. Opt. Technol. Lett. 2021; 63: 2179– 2185. https://doi.org/10.1002/mop.32869.
- Amit Kumar Baghel, **Shashank S. Kulkarni**, and Sisir Kumar Nayak, "Linear to Cross-Polarization Transmission Converter using Ultra-Thin and Smaller Periodicity Metasurface", IEEE Antennas Wireless Propag. Lett. vol. 18, no. 7, pp. 1433-1437, July 2019.
- Amit Kumar Baghel, **Shashank S. Kulkarni**, and Sisir Kumar Nayak, "Far-field Wireless Power Transfer Using GRIN Lens Metamaterial at GHz Frequency", IEEE Microw. Wireless Component Lett., vol. 29, no. 6, pp. 424-426, June 2019.

- Amit Kumar Baghel, **Shashank S. Kulkarni**, and Sisir Kumar Nayak, “A parabolic profile pyramidal horn antenna with lower phase center variation and 3dB beam width in S-band”, IET Microwaves, Antennas and Propag., doi:10.1049/iet-map.2018.5824.

Conferences

- **Shashank. S. Kulkarni**, A. K. Baghel and S. K. Nayak, “Square Slotted Patch Antenna for 2.45 GHz Far-field Wireless Power Transfer”, 2019 IEEE International Conference on Microwaves, Antennas, Communications and Electronic Systems (COMCAS), 2019, pp. 1-4, doi: 10.1109/COMCAS44984.2019.8958143.
- **Shashank S. Kulkarni**, and Sisir Kumar Nayak, “Ring Fractal Patch Antenna for GPS Applications,” IEEE International Conference for Convergence in Technology (I2CT), 29-31 Mar 2019, Pune, India.
- Vivek Kumar, Baghel A. K., **Shashank S. Kulkarni**, Sanghai N. P., Nayak S. K., “High Power Microwave Rectifier for Lower Variation to Input Power and Phase,” 2022 IEEE International Conference on Signal Processing, Informatics, Communication and Energy Systems (SPICES), Thiruvananthapuram, India, 2022, pp. 339-342, doi: 10.1109/SPICES52834.2022.9774143.
- A. K. Baghel, **Shashank S. Kulkarni** and S. K. Nayak, “Enhancement of received power in far-field microwave wireless power transfer,” 2020 IEEE Wireless Power Transfer Conference (WPTC), 2020, pp. 102-105, doi:10.1109/WPTC48563.2020.9295611.
- A. K. Baghel, **Shashank S. Kulkarni** and S. K. Nayak, “Simple way of Frequency Tuning using Pin Diode of Transmission type Digital Metasurface,” 2019 IEEE International Conference on Microwaves, Antennas, Communications and Electronic Systems (COMCAS), 2019, pp. 1-3, doi:10.1109/COMCAS44984.2019.8958455.
- A. K. Baghel, **Shashank S. Kulkarni** and S. K. Nayak, “Efficient Modeling of DC-RF module of Space Solar Power Satellite with Improved Antenna design and Metasurface”, 2019 IEEE International Conference on Microwaves, Antennas, Communications and Electronic Systems (COMCAS), 2019, pp. 1-4.

Achievements

- **Certificate cum Merit**, DRDO Dare to Dream 4.0 Contest, “Metamaterial-based Microwave Directional Energy Weapon for High-Power Beaming”, **Shashank Satish Kulkarni**.

- **First Prize**, National Student Research Convention Anveshan 2023, on 16-17 March 2023, Gujarat “All in One Soil Health & Plant Disease Monitoring using Machine Learning,” Anurag R. Lambor, **Shashank S. Kulkarni**, Amarnath Kumar, and Sisir Kumar Nayak

- **Prof. S. K. Mukherjee Gold Medal** for National Winner and **First Prize**, National Student Research Convention Anveshan 2021-2022, on 28 March 2022, Academy of Maritime Education & Training, Chennai 2022 “Wireless Power Transmission with Advanced Electromagnetic Field Detector,” Anurag R. Lambor, **Shashank S. Kulkarni**, Amarnath Kumar, and Sisir Kumar Nayak

- **First Prize** 2022 Open Data Hackathon, 24 Feb 2022, Nashik, Maharashtra, “Portable Inexpensive Potentiostat,” Anurag R. Lambor, **Shashank S. Kulkarni**, Sanghai Niraja Pravin

- **Second Runner-up**, AeroIndia – 2019, Yelahanka Air Force Station, Bengaluru, on 23 Feb 2019 by Hon’ble Governor of Karnataka, “Charging UAV by far-field WPT”, Amit Kumar Baghel, **Shashank Satish Kulkarni**, Deepak Kumar Sahoo.

Appendix A

Propagation of EM wave

Consider a region of space filled with a material that is

- linear: μ and ε are constant;
- isotropic: There is full rotational symmetry (no preferred direction in space);
- Source-free: the charge density ρ is zero;
- non-conducting: the conductivity σ is zero, and hence $\mathbf{J} = \sigma\mathbf{E}$ is also zero. In this

region, Maxwell's equation takes the form:

$$\nabla \cdot \mathbf{E} = 0 \tag{A.1}$$

$$\nabla \cdot \mathbf{B} = 0 \tag{A.2}$$

$$\nabla \times \mathbf{B} = \mu\varepsilon\mathbf{E} \tag{A.3}$$

$$\nabla \times \mathbf{E} = -\frac{\partial \mathbf{B}}{\partial t} \tag{A.4}$$

The wave equations using the Hertzian operator are written as

$$\left(\nabla^2 - \mu\varepsilon\frac{\partial^2}{\partial t^2}\right)\begin{Bmatrix}\mathbf{E}(\mathbf{r},\mathbf{t})\\ \mathbf{B}(\mathbf{r},\mathbf{t})\end{Bmatrix} = 0 \tag{A.5}$$

The wave equation (A.5) can be solved by

$$\mathbf{E}(\mathbf{r},\mathbf{t}) = \mathbf{E}_0\cos(\omega t - \mathbf{k}\cdot\mathbf{r} + \phi_0) \tag{A.6}$$

where $\mathbf{E}_0$ and $\mathbf{k}$ are constant vectors, and ω and ϕ_0 are constant scalars. It is a plane wave of single frequency ω at a time and is hence called a monochromatic wave. The field (A.6) is a valid solution of the wave equation (A.5) if $\mathbf{k}$ and ω satisfy

$$\frac{\omega^2}{\mathbf{k}^2} = v^2 = \frac{1}{\mu\varepsilon} \tag{A.7}$$

and is known as a dispersion relation. It relates the frequency of the wave ω to the wave vector $\mathbf{k}$. By writing the vector $\mathbf{E}_0$ and $\mathbf{k}$ in terms of components:

$$\mathbf{E}_0 =< \mathbf{E}_{0x}, \mathbf{E}_{0y}, \mathbf{E}_{0z} > \tag{A.8}$$

$$\mathbf{k} =< \mathbf{k}_x, \mathbf{k}_y, \mathbf{k}_z > \tag{A.9}$$

We find that for the field given by equation (A.6) in relation with (A.1) only satisfies for all positions $\mathbf{r}$ and time t if $\mathbf{k}$ and $\mathbf{E}_0$ satisfies:

$$\mathbf{k} \cdot \mathbf{E}_0 = 0 \tag{A.10}$$

In the solution (A.6) of the wave equation

$$\mathbf{E}(\mathbf{r}, \mathbf{t}) = \mathbf{E}_0 \cos(\omega t - \mathbf{k} \cdot \mathbf{r} + \phi_0) \tag{A.11}$$

at fixed position $\mathbf{r}$, the field strength $\mathbf{E}$ varies sinusoidally with angular frequency ω in the direction of $\mathbf{k}$. The field along a plane perpendicular to $\mathbf{k}$ is equiphase. Therefore, the electric field $\mathbf{E}(\mathbf{r}, t)$ takes the form of a plane wave advancing in the direction of $\mathbf{k}$. Since $\mathbf{k} \cdot \mathbf{E}_0 = 0$, the field is perpendicular to the direction of motion and known as a transverse wave.

The wave equation (A.6) for the magnetic field $\mathbf{B}$ has a similar solution of the form

$$\mathbf{B}(\mathbf{r}, \mathbf{t}) = \mathbf{B}_0 \cos(\omega t - \mathbf{k} \cdot \mathbf{r} + \phi_0) \tag{A.12}$$

where $\mathbf{B}_0$ and $\mathbf{k}$ are constant vectors, and ω and ϕ_0 are constant scalars.

Appendix B

Antenna terminologies

Field regions

The space surrounding the antenna is divided into three regions; namely, *reactive near field*, *radiating near-field* (Fresnel) and *far-field* (Fraunhofer). The amplitude pattern of an antenna, as the observation distance is varied from the reactive near-field to the far field, changes in shape because of variations of the field, both magnitude and phase. The reactive near field is defined as that portion of the near-field region immediately surrounding the antenna wherein the reactive field predominates. The outer boundary of this region for most of the antennas is considered to exist as a distance $R < 0.62\sqrt{D^3/\lambda}$ from the antenna surface, where λ is the wavelength (in mm) and D is the largest physical dimension (in mm) of the antenna.

Radiating near field (Fresnel) region is defined as that region of the field of an antenna between the reactive near-field and the far-field region wherein radiation fields predominate and wherein the angular field distribution is dependent upon the distance from the antenna. If the antenna has a maximum dimension that is very small as compared to its wavelength ($D \ll \lambda$), this region may not exist. For antennas focused at infinity, this region is sometimes referred to as the Fresnel region on the basis of analogy to optical terminology. This region has existence between the distance $R \geq 0.62\sqrt{D^3/\lambda}$ and $R < 2D^2/\lambda$.

Far-field (Fraunhofer) region is defined as that region of the field of an antenna where the angular field distribution is essentially independent of the distance from the antenna. For an antenna focused at infinity, the far-field region is also referred to as the Fraunhofer region on the basis of analogy to optical terminology. This region is considered to exist at a distance $R > 2D^2/\lambda$. In this region, the field components are transverse and angular distribution is independent of the radial distance $R = 2D^2/\lambda$.

Radiation intensity

Radiation intensity in a given direction is defined as the power radiated from an antenna per unit solid angle. It's a far-field parameter and can be obtained by multiplying radiation intensity by the square of the distance. Mathematically [37],

$$U = r^2 W_{rad} \tag{B.1}$$

where

U = radiation intensity (W/unit solid angle)

W_{rad} = radiation density (W/m^2)

The far-zone radiation intensity is given by [**?**],

$$U(\theta,\phi) = \frac{r^2}{2\eta}|\mathbf{E}(r,\theta,\phi)|^2 \backsimeq \frac{1}{2\eta}[|E^o_\theta(\theta,\phi)|^2 + |E^o_\phi(\theta,\phi)|^2] \tag{B.2}$$

where

$\mathbf{E}(r,\theta,\phi)$ = far-zone electric field intensity of the antenna = $(\mathbf{E}^o(\theta,\phi)e^{-jkr})/r$

E_θ, E_ϕ = far-zone electric field components of the antenna

η = intrinsic impedance of the medium

Beamwidth

Beamwidth is the angular separation between two identical points on the opposite side of the maximum value of the pattern. There are two beamwidths that are Half-Power Beamwidth (HPBW) and First-Null Beamwidth (FNBW). HPBW is that beamwidth where the power drops to half of its maximum and FNBW is where the main lobe approaches zero (null) value for the first time.

Gain

The gain of an antenna in a particular direction is defined as the ratio of the intensity in a given direction to the radiation intensity that would be obtained if the power accepted by the antenna were radiated isotropically. The radiation intensity corresponding to the isotropically radiated power is equal to the power accepted (input) by the antenna divided by 4π. Mathematically [37],

$$G = 4\pi \frac{\text{radiation intensity}}{\text{total input (accepted) power}}$$

$$G = 4\pi \frac{U(\theta,\phi)}{P_{in}} \tag{B.3}$$

Gain is related to directivity as

$$G(\theta,\phi) = e_{cd} D(\theta,\phi) \tag{B.4}$$

where

e_{cd} = antenna radiation intensity (dimensionless)

When $e_{cd} = 1$, the gain become maximum and denoted as G_0 and can be expressed with its partial components as [37],

$$G_0 = G_\theta + G_\phi \tag{B.5}$$

$$G_\theta = \frac{4\pi U_\theta}{P_{in}} \tag{B.6}$$

$$G_\phi = \frac{4\pi U_\phi}{P_{in}} \tag{B.7}$$

where

U_θ = radiation intensity in a given direction contained in E_θ field components

U_ϕ = radiation intensity in a given direction contained in E_ϕ field components

P_{in} = total input (accepted) power

Antenna efficiency

The total antenna efficiency e_0 (dimensionless) is used to take into account losses at the input terminals and within the structure of the antenna. These losses may due to the reflections because of the mismatch between the transmission line and the antenna, conduction and dielectric losses. The general expression for antenna efficiency is written as [37],

$$e_0 = e_r e_c e_d = e_r e_{cd} \tag{B.8}$$

where

e_0 = total efficiency

e_r = reflection (mismatch) efficiency = $(1 - |\Gamma|^2)$

$e_{cd} = e_c e_d$

e_c = conduction efficiency

e_d = dielectric efficiency

Γ = voltage reflection coefficient at the antenna input terminals

Appendix C

Parabolic reflector

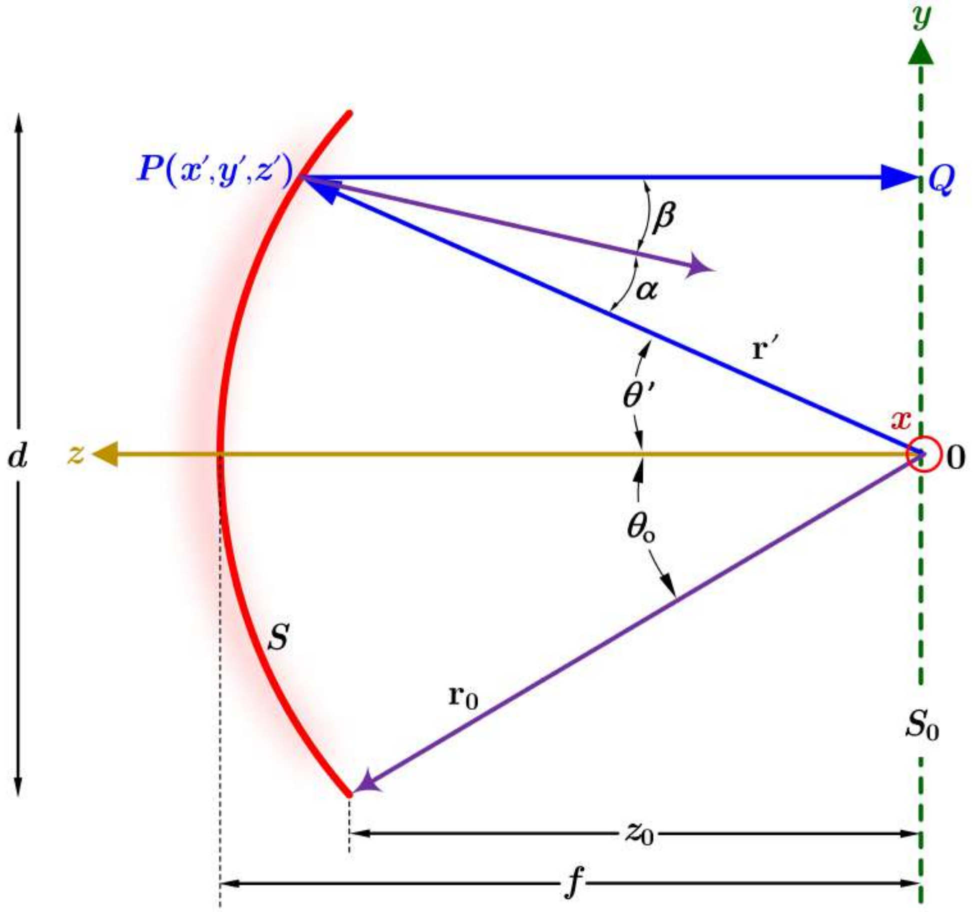

Figure C.1: 2D cross-section of a front-fed paraboloidal reflector.

A parabola is rotated about its axis to form the surface of a paraboloidal reflector. Its surface must have a paraboloid of revolution to convert rays from the reflector's focus into plane waves. The design is based on optical principles and does not account for any deformations (diffractions) caused by the reflector's rim. Using Figure **??** and a plane perpendicular to the reflector's axis through the focus, it follows that

$$OP + PQ = 2f = C_k \tag{C.1}$$

where C_k is a constant. Since

$$OP = r' \tag{C.2}$$

$$PQ = r' \cos\theta'$$

(C.1) cab be written as

$$r'(1 + \cos\theta') = 2f \tag{C.3}$$

or

$$r' = \frac{2f}{(1 + \cos\theta')} = f \sec^2\left(\frac{\theta'}{2}\right)\theta \leq \theta' \tag{C.4}$$

(C.4) is also the equation of a paraboloid in terms of the spherical coordinates r',θ',ϕ' given that a paraboloid is a parabola of rotation (around its axis). As a result of its rotational symmetry, ϕ' is unaffected by any modifications. In rectangular coordinates, (C.4) can be written as

$$r' + r' \cos\theta' = \sqrt{(x')^2 + (y')^2 + (z')^2} + z' = 2f \tag{C.5}$$

or

$$(x')^2 + (y')^2 = 4f(f - z') \tag{C.6}$$

with the condition

$$(x')^2 + (y')^2 \leq (d/2)^2 \tag{C.7}$$

It is preferred to define a unit vector normal to the local tangent at the surface reflection point while analyzing parabolic reflectors. To do this, (C.4) is first written as

$$f - r' \cos^2\left(\frac{\theta'}{2}\right) = S = 0 \tag{C.8}$$

a gradient is obtained to form a normal to the surface as follows

$$\begin{aligned}\mathbf{N} &= \nabla\Big[f - r' \cos^2\left(\frac{\theta'}{2}\right)\Big] \\ &= \hat{\mathbf{a}}_r' \frac{\partial S}{\partial r'} + \hat{\mathbf{a}}_\theta' \frac{1}{r'}\frac{\partial S}{\partial \theta'} \\ &= -\hat{\mathbf{a}}_r' \cos^2\left(\frac{\theta'}{2}\right) + \hat{\mathbf{a}}_\theta' \cos\left(\frac{\theta'}{2}\right) \sin\left(\frac{\theta'}{2}\right)\end{aligned} \tag{C.9}$$

A unit vector normal to S is formed from (C.9) as

$$\hat{\mathbf{n}} = \frac{\mathbf{N}}{|\mathbf{N}|} = -\hat{\mathbf{a}}_r' \cos\left(\frac{\theta'}{2}\right) + \hat{\mathbf{a}}_\theta' \sin\left(\frac{\theta'}{2}\right) \tag{C.10}$$

In order to determine the angle between a vector pointing from the focus to the reflection point and the unit vector $\hat{\mathbf{n}}$, which is normal to the surface at the reflection point [37], we form

$$\begin{aligned}\cos\alpha &= -\hat{\mathbf{a}}_r' \cdot \hat{\mathbf{n}} = -\hat{\mathbf{a}}_r' \cdot \Big[-\hat{\mathbf{a}}_r' \cos\left(\frac{\theta'}{2}\right) + \hat{\mathbf{a}}_\theta' \sin\left(\frac{\theta'}{2}\right)\Big] \\ &= \cos\left(\frac{\theta'}{2}\right)\end{aligned} \tag{C.11}$$

Similarly, the angle between $\hat{\mathbf{n}}$ and the z-axis is given by

$$cos\beta = -\hat{\mathbf{a}}_z' \cdot \hat{\mathbf{n}} = -\hat{\mathbf{a}}_z' \cdot \Big[-\hat{\mathbf{a}}_r' \cos\left(\frac{\theta'}{2}\right) + \hat{\mathbf{a}}_\theta' \sin\left(\frac{\theta'}{2}\right)\Big] \tag{C.12}$$

using the transformations

$$\begin{bmatrix} A_r \\ A_\theta \\ A_\phi \end{bmatrix} = \begin{bmatrix} \sin\theta\cos\phi & \sin\theta\sin\phi & \cos\theta \\ \cos\theta\cos\phi & \cos\theta\sin\phi & -\sin\theta \\ -\sin\phi & \cos\phi & 0 \end{bmatrix} \begin{bmatrix} A_x \\ A_y \\ A_z \end{bmatrix} \tag{C.13}$$

(C.12) can be written as

$$\begin{aligned}\cos\beta &= -(\hat{\mathbf{a}}_r' \cos\theta' - \hat{\mathbf{a}}_\theta') \cdot \Big[-\hat{\mathbf{a}}_r' \cos\left(\frac{\theta'}{2}\right) + \hat{\mathbf{a}}_\theta' \sin\left(\frac{\theta'}{2}\right)\Big] \\ &= \cos\left(\frac{\theta'}{2}\right)\end{aligned} \tag{C.14}$$

The relationship between the subtended angle θ_0 and the f/d ratio is an additional expression that is typically prominent in reflector analysis. geometry derived from Figure **??** as

$$\theta_0 = \tan^{-1}\left(\frac{d/2}{z_0}\right) \tag{C.15}$$

where z_0 is the distance along the reflector's axis from the focal point to the rim's edge. From (2.6)

$$z_0 = f - \frac{x_0^2 + y_0^2}{4f} = f - \frac{(d/2)^2}{4f} = f - \frac{d^2}{16f} \tag{C.16}$$

Substituting (C.16) in (C.15) reduces it to

$$\theta_0 = \tan^{-1}\left|\frac{\frac{d}{2}}{f - \frac{d^2}{16f}}\right| = \tan^{-1}\left|\frac{\frac{1}{2}(\frac{f}{d})}{(\frac{f}{d})^2 - \frac{d^2}{16f}}\right| \tag{C.17}$$

which can also be expressed as

$$f = \left(\frac{d}{4}\right)\cot\left(\frac{\theta_0}{2}\right) \tag{C.18}$$

Aperture distribution method

In the aperture distribution approach, the field reflected by the paraboloid's surface is first determined over a plane perpendicular to the reflector's axis. For this, geometrical optics techniques (ray tracing) are typically used. As shown in Figure C.2, the aperture plane is taken through the focal point, over which the equivalent sources are subsequently formed. The equivalent sources are considered zero outside the reflector's projected area on the aperture plane. The advantage of the aperture distribution method is that the integration over the aperture plane can be accomplished with equal ease regardless of the feed pattern or feed position. The following approximations for the reflector in Figure C.2 are assumed:

- The current density is zero on the reflector's shadow side.
- The current density discontinuity over the reflector's rim is neglected.
- Direct radiation and aperture blockage by the feed are neglected.

Assume a y-polarized source with a gain function of $G_f(\theta', \phi')$ is positioned at the focus

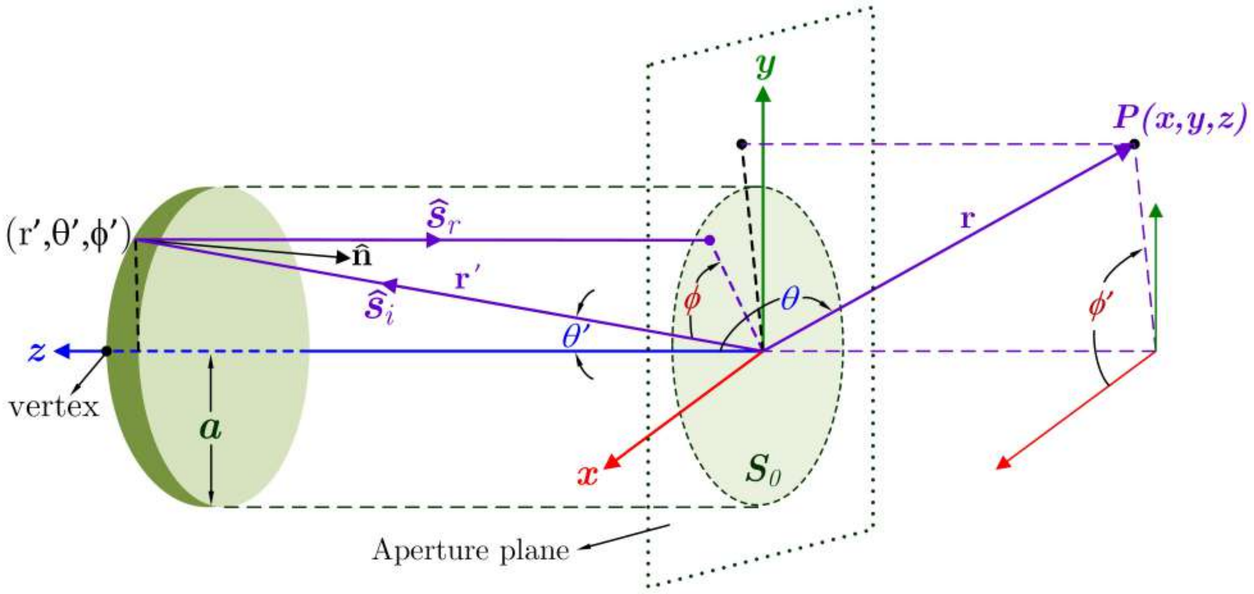

Figure C.2: Three dimensional geometry of a paraboloidal reflector system.

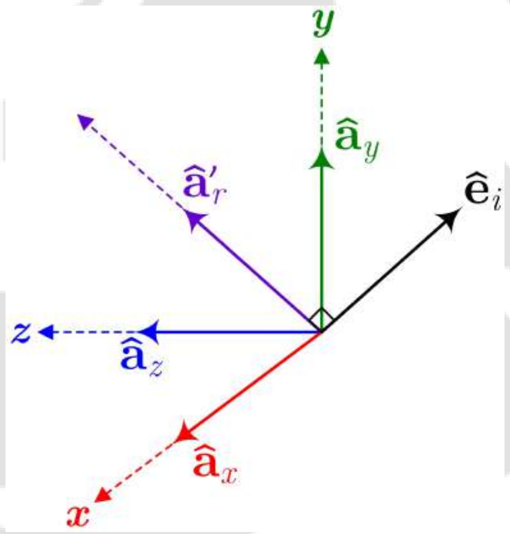

Figure C.3: Three dimensional geometry of a paraboloidal reflector system.

of a paraboloid reflector. The radiation output of this source is given by

$$U(\theta', \phi') = \frac{P_t}{4\pi} G_f(\theta', \phi') \tag{C.19}$$

where P_t is the total radiated power. In the far zone, the intensity at a point r' is written as

$$U(\theta', \phi') = \frac{1}{2}\Re\Big[\mathbf{E}_0(\theta', \phi') \times \mathbf{H}_0^*(\theta', \phi')\Big] = \frac{1}{2\eta}|\mathbf{E}_0(\theta', \phi')|^2 \tag{C.20}$$

or

$$|\mathbf{E}_0(\theta', \phi')| = \Big[2\eta U(\theta', \phi')\Big]^{1/2} = \Big[\eta \frac{P_t}{2\pi} G_f(\theta', \phi')\Big]^{1/2} \tag{C.21}$$

The incidence field with respect to a direction perpendicular to the radial distance is therefore expressed as

$$
\begin{aligned}
\mathbf{E}^i(r',\theta',\phi') &= \hat{\mathbf{e}}_i \frac{e^{-jkr'}}{r'}\left[\sqrt{\frac{\mu}{\varepsilon}}\frac{P_t}{2\pi}G_f(\theta',\phi')\right]^{1/2} \\
&= \hat{\mathbf{e}}_i \frac{e^{-jkr'}}{r'} C_1\sqrt{G_f(\theta',\phi')} \qquad \text{(C.22)} \\
C_1 &= \left(\frac{\mu}{\varepsilon}\right)^{1/4}\left(\frac{P_t}{2\pi}\right)^{1/2} \qquad \text{(C.23)}
\end{aligned}
$$

where $\hat{\mathbf{e}_i}$ is a unit vector perpendicular to $\hat{\mathbf{a}'}_r$ and parallel to the plane formed by $\hat{\mathbf{a}'}_r$ and $\hat{\mathbf{a}}_y$ as shown in Figure C.3. It can be shown that on the surface of the reflector [37]

$$
\begin{aligned}
\mathbf{J}_s &= \left(2\sqrt{\frac{\varepsilon}{\mu}}\right)\left[\hat{\mathbf{n}} \times \left(\hat{\mathbf{s}}_i \times \mathbf{E}^i\right)\right] \\
&= \left(2\sqrt{\frac{\varepsilon}{\mu}}\right)\frac{e^{-jkr'}}{r'}C_1\sqrt{G_f(\theta',\phi')}\mathbf{u} \qquad \text{(C.24)}
\end{aligned}
$$

where

$$\mathbf{u} = \hat{\mathbf{n}} \times (\hat{\mathbf{a}'}_r \times \hat{\mathbf{e}}_i) = (\hat{\mathbf{n}} \cdot \hat{\mathbf{e}}_i)\hat{\mathbf{a}'}_r - (\hat{\mathbf{n}} \cdot \hat{\mathbf{a}'}_r)\hat{\mathbf{e}}_i \qquad \text{(C.25)}$$

which reduced to

$$
\begin{aligned}
\mathbf{u} = \Big[&-\hat{\mathbf{a}}_x \sin\theta' \sin\left(\frac{\theta'}{2}\right)\sin\phi'\cos\phi' + \hat{\mathbf{a}}_y \cos\left(\frac{\theta'}{2}\right)(\sin^2\phi' cos\theta' + \cos^2\phi') \\
&-\hat{\mathbf{a}}_z \cos\theta' \sin\phi' \sin\left(\frac{\theta'}{2}\right)\Big] \Big/ \sqrt{1-\sin^2\theta' sin^2\phi'} \qquad \text{(C.26)}
\end{aligned}
$$

The reflected electric field ($\mathbf{E}^r$) at a point r' is calculated first to find the aperture field $\mathbf{E}_{ap}$.

$$\mathbf{E}^r = \hat{\mathbf{e}}_r \frac{e^{-jkr'}}{r'} C_1\sqrt{G_f(\theta'\phi')} \qquad \text{(C.27)}$$

where unit vector $\hat{\mathbf{e}}_r$ is the polarization vector in direction of the reflected field. The surface current density is

$$
\begin{aligned}
\mathbf{J}_s &= 2\hat{\mathbf{n}} \times \mathbf{H}^r \approx \frac{2}{\eta}\left[\hat{\mathbf{n}} \times (\hat{\mathbf{s}}_r \times \mathbf{E}^r)\right] \\
&= 2\sqrt{\frac{\varepsilon}{\mu}}\hat{\mathbf{n}} \times (\hat{\mathbf{s}}_r \times \mathbf{E}^r)\Big] \qquad \text{(C.28)}
\end{aligned}
$$

since $\hat{\mathbf{s}}_r = -\hat{\mathbf{a}}_z$, using (C.27), (C.28) can be written as

$$\mathbf{J}_s = 2\sqrt{\frac{\varepsilon}{\mu}} C_1 \frac{e^{-jkr'}}{r'} \sqrt{G_f(\theta', \phi')}\mathbf{u} \tag{C.29}$$

where

$$\mathbf{u} = \hat{\mathbf{n}} \times (-\hat{\mathbf{a}}_z \times \hat{\mathbf{e}}_r) = -\hat{\mathbf{a}}_z(\hat{\mathbf{n}} \cdot \hat{\mathbf{e}}_r) - \hat{\mathbf{e}}_r \cos\left(\frac{\theta'}{2}\right) \tag{C.30}$$

The vector $\mathbf{u}$ in (C.29) and (C.30) is same as that of (C.24)-(C.26). Therefore, it can be shown that [37],

$$\hat{\mathbf{e}}_r = \frac{\hat{\mathbf{a}}_x \sin\phi' \cos\phi'(1 - \cos\theta') - \hat{\mathbf{a}}_y(\sin^2\phi' \cos\theta' + \cos^2\phi')}{\sqrt{1 - \sin^2\theta' \sin^2\phi'}} \tag{C.31}$$

Thus, the field $\mathbf{E}^r$ at the point of reflection r' is defined as (C.27), where $\hat{\mathbf{e}}_r$ is given in (C.31). The field on the plane passing through the focal point is expressed as

$$\mathbf{E}_{ap} = \hat{\mathbf{e}}_r C_1 \frac{e^{-jkr'(1+\cos\theta')}}{r'} \sqrt{G_f(\theta', \phi')} = \hat{\mathbf{a}}_x E_{xa} + \hat{\mathbf{a}}_y E_{ya} \tag{C.32}$$

where E_{xa} and E_{ya} represent the $x-$ and $y-$components of the reflected plane wave over the aperture. Using these components, an equivalent formed on the aperture plane is given as

$$\begin{aligned}\mathbf{J}'_s &= \hat{\mathbf{n}} \times \mathbf{H}_a \\ &= -\hat{\mathbf{a}}_z \times \left(\hat{\mathbf{a}}_x \frac{E_{ay}}{\eta} - \hat{\mathbf{a}}_y \frac{E_{ax}}{\eta}\right) \\ &= -\hat{\mathbf{a}}_x \frac{E_{ay}}{\eta} - \hat{\mathbf{a}}_y \frac{E_{ax}}{\eta} \end{aligned} \tag{C.33}$$

$$\begin{aligned}\mathbf{M}'_s &= -\hat{\mathbf{n}} \times \mathbf{E}_a \\ &= +\hat{\mathbf{a}}_z \times \left(\hat{\mathbf{a}}_x E_{ax} + \hat{\mathbf{a}}_y E_{ay}\right) \\ &= -\hat{\mathbf{a}}_x E_{ay} + \hat{\mathbf{a}}_y E_{ax} \end{aligned} \tag{C.34}$$

The integration over the predicted cross-sectional area S_0 of the reflector's aperture plane is obtained by

$$E_{\theta S} = jC_{S_0} \iint_{S_0} \Big(E_{ax} \cos\phi - E_{ay} \sin\phi \Big) e^{jk(u'+v')} dx' dy' \tag{C.35}$$

$$E_{\phi S} = jC_{S_0} \iint_{S_0} \Big(E_{ax} \sin\phi + E_{ay} \cos\phi \Big) e^{jk(u'+v')} dx' dy' \tag{C.36}$$

$$C_{S_0} = \frac{ke^{-jkr}}{4\pi r}(1 - \cos\theta)$$

$$u' = x' \sin\theta \cos\phi$$

$$v' = y' \sin\theta \sin\phi$$

The aperture distribution approach and numerical integration techniques are utilized to determine the radiation patterns of the paraboloidal and spherical reflectors. The components in (D.35) and (D.36) are the secondary patterns formed by scattering from the reflector. The sum of the primary pattern and secondary pattern of the feed element determines the system's overall pattern. Due to its relatively low intensity, the principal pattern in the reflector's boresight (forward) direction is usually negligible for most feeds (including horns).

References

[1] D. Wu, R. Mai, W. Zhou, Y. Liu, F. Peng, S. Zhao, and Q. Zhou, "An improved pulse density modulator in inductive power transfer system," *IEEE Trans. Power Electron.*, 2021.

[2] Y. Wang, A. a Mostafa, H. Zhang, Y. Mei, C. Zhu, and F. Lu, "Sensitivity investigation and mitigation on power and efficiency to resonant parameters in an LCC network for inductive power transfer," *IEEE Journal of Emerging and Selected Topics in Industrial Electronics*, 2021.

[3] X. Zan and A.-T. Avestruz, "100 MHz symmetric current-mode class D wireless power transfer," *IEEE Journal of Emerging and Selected Topics in Power Electronics*, 2022.

[4] P. Yadav and M. Veerachary, "Auxiliary coil based square coupler for wireless power transfer system," *IEEE Trans. Ind. Appl.*, 2022.

[5] W. Dong, U. Madawala, and C. Baguley, "A versatile unified model for inductive power transfer (IPT) systems," *IEEE Journal of Emerging and Selected Topics in Industrial Electronics*, 2021.

[6] L. Qian, K. Cui, H. Xia, H. Shao, J. Wang, and Y. Xia, "An inductive power transfer system for powering wireless sensor nodes in structural health monitoring applications," *IEEE Trans. Micro. Theory Techniq.*, 2022.

[7] A. Garcia-Bediaga, A. Avila, I. Alzuguren, A. Sanchez, and A. Rujas, "Power factor corrector control strategies of a bidirectional wireless battery charger with an unfolding active rectifier," *IEEE Journal of Emerging and Selected Topics in Power Electronics*, 2022.

[8] R. He, P. Zhao, G. Ning, K. Yue, Y. Liu, and M. Fu, “Optimal driving and loading scheme for multiple-receiver inductive power transfer,” *IEEE Trans. Ind. Electron.*, 2021.

[9] J. H. Kim, B.-S. Lee, J.-H. Lee, S.-H. Lee, C.-B. Park, S.-M. Jung, S.-G. Lee, K.-P. Yi, and J. Baek, “Development of 1-MW inductive power transfer system for a high-speed train,” *IEEE Trans. Ind. Electron.*, vol. 62, no. 10, pp. 6242–6250, 2015.

[10] J.-H. Choi, S.-K. Yeo, S. Park, J.-S. Lee, and G.-H. Cho, “Resonant regulating rectifiers (3R) operating for 6.78 MHz resonant wireless power transfer (RWPT),” *IEEE Journal of Solid-state Circuits*, vol. 48, no. 12, pp. 2989–3001, 2013.

[11] Y. Zhang, T. Lu, Z. Zhao, F. He, K. Chen, and L. Yuan, “Selective wireless power transfer to multiple loads using receivers of different resonant frequencies,” *IEEE Trans. Power Electron.*, vol. 30, no. 11, pp. 6001–6005, 2014.

[12] Q. Li and Y. C. Liang, “An inductive power transfer system with a high-Q resonant tank for mobile device charging,” *IEEE Trans. Power Electron.*, vol. 30, no. 11, pp. 6203–6212, 2015.

[13] A. Namadmalan, “Self-oscillating tuning loops for series resonant inductive power transfer systems,” *IEEE Trans. Power Electron.*, vol. 31, no. 10, pp. 7320–7327, 2015.

[14] F. Lu, H. Zhang, H. Hofmann, and C. C. Mi, “An inductive and capacitive combined wireless power transfer system with lc-compensated topology,” *IEEE Trans. Power Electron.*, vol. 31, no. 12, pp. 8471–8482, 2016.

[15] G. Ke, Q. Chen, S. Zhang, X. Xu, and L. Xu, “A single-ended hybrid resonant converter with high misalignment tolerance,” *IEEE Trans. Power Electron.*, 2022.

[16] D. E. Raible, “High intensity laser power beaming for wireless power transmission,” Ph.D. dissertation, Cleveland State University, 2008.

[17] N. Kawashima and K. Takeda, “Laser energy transmission for a wireless energy supply to robots,” *Robotics and Automation in Construction*, vol. 10, pp. 373–380, 2008.

[18] D. Shi, L. Zhang, H. Ma, Z. Wang, Y. Wang, and Z. Cui, “Research on wireless power transmission system between satellites,” in *2016 IEEE Wireless Power Transfer Conference (WPTC)*. IEEE, 2016, pp. 1–4.

[19] K. Jin and W. Zhou, “Wireless laser power transmission: A review of recent progress,” *IEEE Trans. Power Electron.*, vol. 34, no. 4, pp. 3842–3859, 2018.

[20] Z.-X. Du and X. Y. Zhang, “High-efficiency single-and dual-band rectifiers using a complex impedance compression network for wireless power transfer,” *IEEE Trans. Ind. Electron.*, vol. 65, no. 6, pp. 5012–5022, 2017.

[21] E. Schamiloglu, “High power microwave sources and applications,” in *2004 IEEE MTT-S International Microwave Symposium Digest (IEEE Cat. No. 04CH37535)*, vol. 2. IEEE, 2004, pp. 1001–1004.

[22] N. Tesla, “System of transmission of electrical energy.” Mar. 20 1900, United States Patent 645,576.

[23] W. C. Brown, “The history of power transmission by radio waves,” *IEEE Trans. Micro. Theory Techn.*, vol. 32, no. 9, pp. 1230–1242, 1984.

[24] W. C. Brown, “Experiments involving a microwave beam to power and position a helicopter,” *IEEE Trans. Aerospace Electron. Systems*, no. 5, pp. 692–702, 1969.

[25] W. C. Brown and E. E. Eves, “Beamed microwave power transmission and its application to space,” *IEEE Trans. Micro. Theory Techn.*, vol. 40, no. 6, pp. 1239–1250, 1992.

[26] N. Shinohara and H. Matsumoto, “Experimental study of large rectenna array for microwave energy transmission,” *IEEE Trans. Micro. Theory Techn.*, vol. 46, no. 3, pp. 261–268, 1998.

[27] C. R. Valenta and G. D. Durgin, “Harvesting wireless power: Survey of energy-harvester conversion efficiency in far-field, wireless power transfer systems,” *IEEE Microwave Magazine*, vol. 15, no. 4, pp. 108–120, 2014.

[28] R. M. Dickinson, “Performance of a high-power, 2.388 GHz receiving array in wireless power transmission over 1.54 km,” in *1976 IEEE-MTT-S International Microwave Symposium.* IEEE, 1976, pp. 139–141.

[29] J. Chen, Z. Hu, S. Wang, Y. Cheng, and M. Liu, “Investigation of wireless power transfer for smart grid on-line monitoring devices under HV condition,” *Procedia Computer Science*, vol. 83, pp. 1307–1312, 2016.

[30] Y. Z. Cheng, J. Jin, W. L. Li, J. F. Chen, B. Wang, and R. Z. Gong, “Indefinite-permeability metamaterial lens with finite size for miniaturized wireless power transfer system,” *AEU-Int J Electron Commun*, vol. 70, no. 9, pp. 1282–1287, 2016.

[31] Y. Cho, J. J. Kim, D.-H. Kim, S. Lee, H. Kim, C. Song, S. Kong, H. Kim, C. Seo, S. Ahn *et al.*, “Thin PCB-type metamaterials for improved efficiency and reduced EMF leakage in wireless power transfer systems,” *IEEE Trans. Micro. Theory Techn.*, vol. 64, no. 2, pp. 353–364, 2016.

[32] T. Takahashi, T. Sasaki, Y. Homma, S. Mihara, K. Sasaki, S. Nakamura, K. Makino, D. Joudoi, and K. Ohashi, “Phased array system for high efficiency and high accuracy microwave power transmission,” in *2016 IEEE International Symposium on Phased Array Systems and Technology (Past).* IEEE, 2016, pp. 1–7.

[33] V. R. Gowda, O. Yurduseven, G. Lipworth, T. Zupan, M. S. Reynolds, and D. R. Smith, “Wireless power transfer in the radiative near field,” *IEEE Antennas Wireless Propag. Lett.*, vol. 15, pp. 1865–1868, 2016.

[34] S.-T. Khang, D.-J. Lee, I.-J. Hwang, T.-D. Yeo, and J.-W. Yu, “Microwave power transfer with optimal number of rectenna arrays for midrange applications,” *IEEE Antennas Wireless Propag. Lett.*, vol. 17, no. 1, pp. 155–159, 2017.

[35] C. Wang, J. Li, A. Zhang, W. T. Joines, and Q. H. Liu, “Dual-band capacitively loaded annular-ring slot antenna for dual-sense circular polarization,” *Journal of Electromagnetic Waves and Applications*, vol. 31, no. 9, pp. 867–878, 2017.

[36] X. Yi, X. Chen, L. Zhou, S. Hao, B. Zhang, and X. Duan, “A microwave power transmission experiment based on the near-field focused transmitter,” *IEEE Antennas Wireless Propag. Lett.*, vol. 18, no. 6, pp. 1105–1108, 2019.

[37] C. A. Balanis, *Antenna theory: analysis and design.* John wiley & sons, 2015.

[38] A. Massa, G. Oliveri, F. Viani, and P. Rocca, “Array designs for long-distance wireless power transmission: State-of-the-art and innovative solutions,” *Proceedings of the IEEE*, vol. 101, no. 6, pp. 1464–1481, 2013.

[39] G. A. Landis, “Re-evaluating satellite solar power systems for earth,” in *2006 IEEE 4th World Conference on Photovoltaic Energy Conference*, vol. 2, 2006, pp. 1939–1942.

[40] V. Talla, B. Kellogg, B. Ransford, S. Naderiparizi, S. Gollakota, and J. R. Smith, “Powering the next billion devices with Wi-Fi,” 2015.

[41] V. Rodriguez, “A brief history of horns,” *Compliance Magazine*, 2010.

[42] D. Oloumi, P. Mousavi, M. I. Pettersson, and D. G. Elliott, “A modified TEM horn antenna customized for oil well monitoring applications,” *IEEE Trans. Antennas Propag.*, vol. 61, no. 12, pp. 5902–5909, 2013.

[43] M. A. Morgan and T. A. Boyd, “A 10–100 GHz double-ridged horn antenna and coax launcher,” *IEEE Trans. Antennas Propag.*, vol. 63, no. 8, pp. 3417–3422, 2015.

[44] R. C. Gupta, S. Saxena, M. B. Mahajan, and R. Jyoti, “Design of dual-band multimode profiled smooth-walled horn antenna for satellite communication,” *IEEE Antennas Wireless Propag. Lett.*, vol. 9, pp. 338–341, 2010.

[45] X.-H. Yin and S.-C. Shi, “A simple design method of multimode horns,” *IEEE Trans. Antennas Propag.*, vol. 53, no. 1, pp. 455–459, 2005.

[46] A. Bhattacharyya and G. Goyette, “Step-horn antenna with high aperture efficiency and low cross-polarisation,” *Electron. Lett.*, vol. 38, no. 24, p. 1, 2002.

[47] H. Deguchi, M. Tsuji, and H. Shigesawa, “Compact low-cross-polarization horn antennas with serpentine-shaped taper,” *IEEE Trans. Antennas Propag.*, vol. 52, no. 10, pp. 2510–2516, 2004.

[48] B. Jacobs, J. W. Odendaal, and J. Joubert, "An improved design for a 1–18 GHz double-ridged guide horn antenna," *IEEE Trans. Antennas Propag.*, vol. 60, no. 9, pp. 4110–4118, 2012.

[49] C. Bruns, P. Leuchtmann, and R. Vahldieck, "Analysis and simulation of a 1–18 GHz broadband double-ridged horn antenna," *IEEE Trans. Electromagn. Compat.*, vol. 45, no. 1, pp. 55–60, 2003.

[50] M. Ignatenko, B. Simakauskas, M. Notaros, and D. S. Filipovic, "A phase center-stabilized K/Ka/V-band linearly polarized horn for luneburg lenses," *IEEE Antennas Wireless Propag. Lett.*, vol. 16, pp. 2726–2729, 2017.

[51] A. D. Olver and J. Xiang, "Design of profiled corrugated horns," *IEEE Trans. Antennas Propag.*, vol. 36, no. 7, pp. 936–940, 1988.

[52] L. Lucci, R. Nesti, G. Pelosi, and S. Selleri, "Phase centre optimization in profiled corrugated circular horns with parallel genetic algorithms," *Progress In Electromagnetics Research*, vol. 46, pp. 127–142, 2004.

[53] S. López-Ruiz, R. Sanchez Montero, F. Tercero-Martínez, P. López-Espí, and J. López-Fernandez, "Optimization of a conical corrugated antenna using multiobjective heuristics for radio-astronomy applications," *International Journal of Antennas and Propagation*, vol. 2016, 2016.

[54] K.-J. Lee, S.-S. Oh, Y.-H. Lee, and Y.-S. Kim, "Front-to-back ratio improvement of a short pyramidal horn antenna using metal strips/rods in LTE/cellular band," *IET Microwaves, Antennas & Propag.*, vol. 10, no. 1, pp. 111–118, 2016.

[55] T. T. Thai, G. R. DeJean, and M. M. Tentzeris, "Design and development of a novel compact soft-surface structure for the front-to-back ratio improvement and size reduction of a microstrip yagi array antenna," *IEEE Antennas Wireless Propag. Lett.*, vol. 7, pp. 369–373, 2008.

[56] P. Aguilà, S. Zuffanelli, G. Zamora, F. Paredes, F. Martín, and J. Bonache, "Front-to-back ratio improvement of printed antennas based on electrically small resonators for microwave presence detectors," *Electron. Lett.*, vol. 51, no. 11, pp. 836–837, 2015.

[57] A. K. Baghel, S. Kulkarni, and S. K. Nayak, "Parabolic profile pyramidal horn antenna with lower phase centre variation and 3 dB beamwidth in S-band," *IET Microwaves, Antennas & Propag.*, vol. 13, no. 10, pp. 1626–1636, 2019.

[58] A. K. Baghel, S. S. Kulkarni, and S. K. Nayak, "A high gain aperture match parabolic horn antenna with stable phase center and higher fbr in s-band," *Microw. Opt. Technol. Lett.*, vol. 63, no. 8, pp. 2179–2185, 2021.

[59] R. A. Shelby, D. R. Smith, and S. Schultz, "Experimental verification of a negative index of refraction," *science*, vol. 292, no. 5514, pp. 77–79, 2001.

[60] A. K. Iyer and G. V. Eleftheriades, "A multilayer negative-refractive-index transmission-line (NRI-TL) metamaterial free-space lens at X-band," *IEEE Trans. Antennas Propag.*, vol. 55, no. 10, pp. 2746–2753, 2007.

[61] M. Navarro-Cia, M. Beruete, I. Campillo, and M. S. Ayza, "Beamforming by left-handed extraordinary transmission metamaterial bi-and plano-concave lens at millimeter-waves," *IEEE Trans. Antennas Propag.*, vol. 59, no. 6, pp. 2141–2151, 2011.

[62] S. Das, H.-L. Nguyen, G. N. Babu, and A. K. Iyer, "Free-space focusing at C-band using a flat fully printed multilayer metamaterial lens," *IEEE Trans. Antennas Propag.*, vol. 63, no. 11, pp. 4702–4714, 2015.

[63] J. P. Turpin, Q. Wu, D. H. Werner, B. Martin, M. Bray, and E. Lier, "Near-zero-index metamaterial lens combined with AMC metasurface for high-directivity low-profile antennas," *IEEE Trans. Antennas Propag.*, vol. 62, no. 4, pp. 1928–1936, 2014.

[64] L. H. Yuan, W. X. Tang, H. Li, Q. Cheng, and T. J. Cui, "Three-dimensional anisotropic zero-index lenses," *IEEE Trans. Antennas Propag.*, vol. 62, no. 8, pp. 4135–4142, 2014.

[65] Q.-W. Lin and H. Wong, "A low-profile and wideband lens antenna based on high-refractive-index metasurface," *IEEE Trans. Antennas Propag.*, vol. 66, no. 11, pp. 5764–5772, 2018.

[66] Z. L. Mei, J. Bai, T. M. Niu, and T. J. Cui, “A half maxwell fish-eye lens antenna based on gradient-index metamaterials,” *IEEE Trans. Antennas Propag.*, vol. 60, no. 1, pp. 398–401, 2011.

[67] H.-X. Xu, G.-M. Wang, Z. Tao, and T. Cai, “An octave-bandwidth half maxwell fish-eye lens antenna using three-dimensional gradient-index fractal metamaterials,” *IEEE Trans. Antennas Propag.*, vol. 62, no. 9, pp. 4823–4828, 2014.

[68] H. F. Ma, B. G. Cai, T. X. Zhang, Y. Yang, W. X. Jiang, and T. J. Cui, “Three-dimensional gradient-index materials and their applications in microwave lens antennas,” *IEEE Trans. Antennas Propag.*, vol. 61, no. 5, pp. 2561–2569, 2013.

[69] E. Erfani, M. Niroo-Jazi, and S. Tatu, “A high-gain broadband gradient refractive index metasurface lens antenna,” *IEEE Trans. Antennas Propag.*, vol. 64, no. 5, pp. 1968–1973, 2016.

[70] D. R. Smith, J. J. Mock, A. Starr, and D. Schurig, “Gradient index metamaterials,” *Physical Review E*, vol. 71, no. 3, p. 036609, 2005.

[71] A. K. Baghel, S. S. Kulkarni, and S. K. Nayak, “Far-field wireless power transfer using GRIN lens metamaterial at ghz frequency,” *IEEE Microw. Wireless Compon. Lett.*, vol. 29, no. 6, pp. 424–426, 2019.

[72] K. P. Esselle *et al.*, “A low-profile compact microwave antenna with high gain and wide bandwidth,” *IEEE Trans. Antennas Propag.*, vol. 55, no. 6, pp. 1880–1883, 2007.

[73] H. Zhang, Y. Abdallah, R. Chantalat, M. Thevenot, T. Monediere, and B. Jecko, “Low-profile and high-gain yagi wire-patch antenna for WiMAX applications,” *IEEE Antennas Wireless Propag. Lett.*, vol. 11, pp. 659–662, 2012.

[74] Z.-Z. Yang, F. Liang, Y. Yi, D. Zhao, and B.-Z. Wang, “Metasurface-based wideband, low-profile, and high-gain antenna,” *IET Microwaves, Antennas & Propag.*, vol. 13, no. 4, pp. 436–441, 2019.

[75] H. Xu, J. Zhou, K. Zhou, and Z. Yu, “Low-profile circularly polarised patch antenna with high gain and conical beam,” *IET Microwaves, Antennas & Propag.*, vol. 12, no. 7, pp. 1191–1195, 2018.

[76] S. X. Ta and I. Park, “Compact wideband circularly polarized patch antenna array using metasurface,” *IEEE Antennas Wireless Propag. Lett.*, vol. 16, pp. 1932–1936, 2017.

[77] S. W. Marcus, “Metamaterial-coated plates for emulating non-specular reflection and antenna reflectors,” *IEEE Trans. Antennas Propag.*, vol. 61, no. 6, pp. 3093–3101, 2013.

[78] S. A. Rezaeieh, M. A. Antoniades, and A. M. Abbosh, “Miniaturization of planar yagi antennas using mu-negative metamaterial-loaded reflector,” *IEEE Trans. Antennas Propag.*, vol. 65, no. 12, pp. 6827–6837, 2017.

[79] M. D. Gregory, J. A. Bossard, Z. C. Morgan, C. S. Cicero, J. A. Easum, J. D. Binion, D. Z. Zhu, C. P. Scarborough, P. L. Werner, D. H. Werner *et al.*, “A low cost and highly efficient metamaterial reflector antenna,” *IEEE Trans. Antennas Propag.*, vol. 66, no. 3, pp. 1545–1548, 2018.

[80] A. Ericsson, D. Sjöberg, G. Gerini, C. Cappellin, F. Jensen, P. Balling, N. J. Fonseca, and P. de Maagt, “A contoured-beam reflector satellite antenna using two doubly curved circular polarization selective surfaces,” *IEEE Trans. Antennas Propag.*, vol. 69, no. 2, pp. 658–671, 2020.

[81] Y. Han, J. Zhang, Y. Li, J. Wang, S. Qu, H. Yuan, and J. Yu, “Miniaturized-element offset-feed planar reflector antennas based on metasurfaces,” *IEEE Antennas Wireless Propag. Lett.*, vol. 16, pp. 282–285, 2016.

[82] S. Wang, H.-X. Xu, M. Wang, C. Wang, Y. Wang, and X. Ling, “A low-RCS and high-gain planar circularly polarized cassegrain meta-antenna,” *IEEE Trans. Antennas Propag.*, 2022.

[83] Z. Wang, S. Zhao, and Y. Dong, "Pattern reconfigurable, low-profile, vertically polarized, ZOR-metasurface antenna for 5G application," *IEEE Trans. Antennas Propag.*, 2022.

[84] S. A. Sis and H. Akça, "Maximizing the efficiency of wireless power transfer systems with an optimal duty cycle operation," *AEU-Int J Electron Commun*, vol. 116, p. 153081, 2020.

[85] Y. Shi, Y. Zhang, M. Shen, Y. Fan, C. Wang, and M. Wang, "Design of a novel receiving structure for wireless power transfer with the enhancement of magnetic coupling," *AEU-Int J Electron Commun*, vol. 95, pp. 236–241, 2018.

[86] M. K. T. Al-Nuaimi, W. Hong, and Y. Zhang, "Design of high-directivity compact-size conical horn lens antenna," *IEEE Antennas Wireless Propag. Lett.*, vol. 13, pp. 467–470, 2014.

[87] X. Ding, H. Yu, S. Zhang, Y. Wu, K. Zhang, and Q. Wu, "Ultrathin metasurface for controlling electromagnetic wave with broad bandwidth," *IEEE Trans. Magnetics*, vol. 51, no. 11, pp. 1–4, 2015.

[88] X. Wang, Y. Wang, Y. Hu, Y. He, and Z. Yan, "Analysis of wireless power transfer using superconducting metamaterials," *IEEE Trans. Applied Superconductivity*, vol. 29, no. 2, pp. 1–5, 2018.

[89] D. C. Corrêa, U. C. Resende, and F. S. Bicalho, "Experiments with a compact wireless power transfer system using strongly coupled magnetic resonance and metamaterials," *IEEE Trans. Magnetics*, vol. 55, no. 8, pp. 1–4, 2019.

[90] D. Brizi, J. P. Stang, A. Monorchio, and G. Lazzi, "A compact magnetically dispersive surface for low-frequency wireless power transfer applications," *IEEE Trans. Antennas Propag.*, vol. 68, no. 3, pp. 1887–1895, 2020.

[91] X. Chen, Y. Ge, and T. S. Bird, "Reduction of sidelobe radiations of the standard pyramidal horn using a thin metamaterial lens," *Electron. Lett.*, vol. 52, no. 24, pp. 1973–1974, 2016.

[92] Z. Yang, L. Guo, C. Yao, Q. Zhang, Z. Xu, M. Guo, and Z. Wang, "Ultrawideband antipodal tapered slot antenna with gradient refractive index metamaterial lens," *IEEE Antennas Wireless Propag. Lett.*, vol. 18, no. 12, pp. 2741–2745, 2019.

[93] I. Aghanejad, H. Abiri, and A. Yahaghi, "Design of high-gain lens antenna by gradient-index metamaterials using transformation optics," *IEEE Trans. Antennas Propag.*, vol. 60, no. 9, pp. 4074–4081, 2012.

[94] Z. Tao, W. X. Jiang, H. F. Ma, and T. J. Cui, "High-gain and high-efficiency GRIN metamaterial lens antenna with uniform amplitude and phase distributions on aperture," *IEEE Trans. Antennas Propag.*, vol. 66, no. 1, pp. 16–22, 2017.

[95] J.-T. Shen, P. B. Catrysse, and S. Fan, "Mechanism for designing metallic metamaterials with a high index of refraction," *Physical review letters*, vol. 94, no. 19, p. 197401, 2005.

[96] A. Pimenov and A. Loidl, "Experimental demonstration of artificial dielectrics with a high index of refraction," *Physical Review B*, vol. 74, no. 19, p. 193102, 2006.

[97] X. Gao, F. L. Yu, C. L. Cai, C. Y. Guan, J. H. Shi, and F. Hu, "Terahertz metamaterial with broadband and low-dispersion high refractive index," *Optics Letters*, vol. 45, no. 17, pp. 4754–4757, 2020.

[98] X. Chen, H. Feng Ma, X. Ying Zou, W. Xiang Jiang, and T. Jun Cui, "Three-dimensional broadband and high-directivity lens antenna made of metamaterials," *Journal of Applied Physics*, vol. 110, no. 4, p. 044904, 2011.

[99] H.-X. Xu, G.-M. Wang, Z. Tao, and T. J. Cui, "High-directivity emissions with flexible beam numbers and beam directions using gradient-refractive-index fractal metamaterial," *Scientific reports*, vol. 4, no. 1, pp. 1–10, 2014.

[100] H. Li, G. Wang, H.-X. Xu, T. Cai, and J. Liang, "X-band phase-gradient metasurface for high-gain lens antenna application," *IEEE Trans. Antennas Propag.*, vol. 63, no. 11, pp. 5144–5149, 2015.

[101] E. Pires, G. Fontgalland, M. Melo, R. Valle, and S. E. Barbin, "Metamaterial-inspired wire antennas," *IEEE Trans. Magnetics*, vol. 49, no. 5, pp. 1893–1896, 2013.

[102] S. Zhang, R. K. Arya, W. G. Whittow, D. Cadman, R. Mittra, and J. Vardaxoglou, "Ultra-wideband flat metamaterial grin lenses assisted with additive manufacturing technique," *IEEE Trans. Antennas Propag.*, vol. 69, no. 7, pp. 3788–3799, 2020.

[103] Z. Szabo, G.-H. Park, R. Hedge, and E.-P. Li, "A unique extraction of metamaterial parameters based on kramers–kronig relationship," *IEEE Trans. Micro. Theory Techn.*, vol. 58, no. 10, pp. 2646–2653, 2010.

[104] B. Arritt, D. Smith, and T. Khraishi, "Equivalent circuit analysis of metamaterial strain-dependent effective medium parameters," *Journal of Applied Physics*, vol. 109, no. 7, p. 073512, 2011.

[105] P. Lu, K. Huang, C. Song, Y. Ding, and G. Goussetis, "Optimal power splitting of wireless information and power transmission using a novel dual-channel rectenna," *IEEE Trans. Antennas Propag.*, vol. 70, no. 3, pp. 1846–1856, 2021.

[106] D. Lee and J. Oh, "Broad dual-band rectifier with wide input power ranges for wireless power transfer and energy harvesting," *IEEE Microw. Wireless Compon. Lett.*, 2022.

[107] B. Wang, K. H. Teo, T. Nishino, W. Yerazunis, J. Barnwell, and J. Zhang, "Experiments on wireless power transfer with metamaterials," *Applied Physics Letters*, vol. 98, no. 25, p. 254101, 2011.

[108] B. Yang, X. Chen, J. Chu, T. Mitani, and N. Shinohara, "A 5.8-GHz phased array system using power-variable phase-controlled magnetrons for wireless power transfer," *IEEE Trans. Micro. Theory Techn.*, vol. 68, no. 11, pp. 4951–4959, 2020.

[109] Y. Tanaka, H. Hamase, K. Kanai, R. Hasaba, H. Sato, Y. Koyanagi, T. Ikeda, H. Tani, M. Gokan, S. Kajiwara *et al.*, "Simulation and implementation of distributed microwave wireless power transfer system," *IEEE Trans. Micro. Theory Techn.*, 2022.

[110] N. Zhang, W. X. Jiang, H. F. Ma, W. X. Tang, and T. J. Cui, "Compact high-performance lens antenna based on impedance-matching gradient-index metamaterials," *IEEE Trans. Antennas Propag.*, vol. 67, no. 2, pp. 1323–1328, 2018.

[111] A. Papathanasopoulos, Y. Rahmat-Samii, N. C. Garcia, and J. D. Chisum, "A novel collapsible flat-layered metamaterial gradient-refractive-index lens antenna," *IEEE Trans. Antennas Propag.*, vol. 68, no. 3, pp. 1312–1321, 2019.

[112] D. Jia, Y. He, N. Ding, J. Zhou, B. Du, and W. Zhang, "Beam-steering flat lens antenna based on multilayer gradient index metamaterials," *IEEE Antennas Wireless Propag. Lett.*, vol. 17, no. 8, pp. 1510–1514, 2018.

[113] Y.-H. Lou, Y.-X. Zhu, G.-F. Fan, W. Lei, W.-Z. Lu, and X.-C. Wang, "Design of Ku-band flat luneburg lens using ceramic 3-D printing," *IEEE Antennas Wireless Propag. Lett.*, vol. 20, no. 2, pp. 234–238, 2020.

[114] J.-H. Kim, Y. Lim, and S. Nam, "Efficiency bound of radiative wireless power transmission using practical antennas," *IEEE Trans. Antennas Propag.*, vol. 67, no. 8, pp. 5750–5755, 2019.

[115] D. Ahn and S. Hong, "A study on magnetic field repeater in wireless power transfer," *IEEE Trans. Industrial Electronics*, vol. 60, no. 1, pp. 360–371, 2012.

[116] E. S. G. Rodríguez, A. K. RamRakhyani, D. Schurig, and G. Lazzi, "Compact low-frequency metamaterial design for wireless power transfer efficiency enhancement," *IEEE Trans. Micro. Theory Techn.*, vol. 64, no. 5, pp. 1644–1654, 2016.

[117] J. Durnin, "Exact solutions for nondiffracting beams. i. the scalar theory," *JOSA A*, vol. 4, no. 4, pp. 651–654, 1987.

[118] J. Durnin, J. J. Miceli, and J. H. Eberly, "Diffraction-free beams," *Phys. Rev. Lett.*, vol. 58, pp. 1499–1501, Apr 1987. [Online]. Available: https://link.aps.org/doi/10.1103/PhysRevLett.58.1499

[119] P. Hannan, "Microwave antennas derived from the cassegrain telescope," *IRE Trans. Antennas Propag.*, vol. 9, no. 2, pp. 140–153, 1961.

[120] Z. Zhefu, “A method for designing high-power offset cassegrain antennas,” *IEEE Trans. Electromagn. Compat.*, vol. 39, no. 3, pp. 255–260, 1997.

[121] P. Zheng, G. Q. Zhao, S. H. Xu, F. Yang, and H. J. Sun, “Design of a W-band full-polarization monopulse cassegrain antenna,” *IEEE Antennas Wireless Propag. Lett.*, vol. 16, pp. 99–103, 2016.

[122] Y.-B. Jung, A. V. Shishlov, and S.-O. Park, “Cassegrain antenna with hybrid beam steering scheme for mobile satellite communications,” *IEEE Trans. Antennas Propag.*, vol. 57, no. 5, pp. 1367–1372, 2009.

[123] K. S. Rao, G. A. Morin, M. Q. Tang, S. Richard, and K. K. Chan, “Development of a 45 GHz multiple-beam antenna for military satellite communications,” *IEEE Trans. Antennas Propag.*, vol. 43, no. 10, pp. 1036–1047, 1995.

[124] S. K. Rao and M. Q. Tang, “Stepped-reflector antenna for dual-band multiple beam satellite communications payloads,” *IEEE Trans. Antennas Propag.*, vol. 54, no. 3, pp. 801–811, 2006.

[125] A. Rebollo, Á. F. Vaquero, M. Arrebola, and M. R. Pino, “3D-printed dual-reflector antenna with self-supported dielectric subreflector,” *IEEE Access*, vol. 8, pp. 209 091–209 100, 2020.

[126] Y. Bi, Y. Li, and J. Wang, “3-D printed wideband cassegrain antenna with a concave subreflector for 5G millimeter-wave 2-D multibeam applications,” *IEEE Trans. Antennas Propag.*, vol. 68, no. 6, pp. 4362–4371, 2020.

[127] C. Han, J. Huang, and K. Chang, “Cassegrain offset subreflector-fed X/Ka dual-band reflectarray with thin membranes,” *IEEE Trans. Antennas Propag.*, vol. 54, no. 10, pp. 2838–2844, 2006.

[128] H. Zhu, S. W. Cheung, and T. I. Yuk, “Enhancing antenna boresight gain using a small metasurface lens: Reduction in half-power beamwidth.” *IEEE Antennas and Propagation Magazine*, vol. 58, no. 1, pp. 35–44, 2016.

[129] Y. Fan, J. Wang, H. Ma, J. Zhang, D. Feng, M. Feng, and S. Qu, "In-plane feed antennas based on phase gradient metasurface," *IEEE Trans. Antennas Propag.*, vol. 64, no. 9, pp. 3760–3765, 2016.

[130] J. Zhao, H. Li, X. Yang, W. Mao, B. Hu, T. Li, H. Wang, Y. Zhou, and Q. Liu, "A compact Ka-band monopulse cassegrain antenna based on reflectarray elements," *IEEE Antennas Wireless Propag. Lett.*, vol. 17, no. 2, pp. 193–196, 2017.

[131] G.-B. Wu, S.-W. Qu, and S. Yang, "Low-profile transmitarray antenna with cassegrain reflectarray feed," *IEEE Trans. Antennas Propag.*, vol. 67, no. 5, pp. 3079–3088, 2019.

[132] T. J. Cui, M. Q. Qi, X. Wan, J. Zhao, and Q. Cheng, "Coding metamaterials, digital metamaterials and programmable metamaterials," *Light: science & applications*, vol. 3, no. 10, pp. e218–e218, 2014.

[133] L. Bao, Q. Ma, G. D. Bai, H. B. Jing, R. Y. Wu, X. Fu, C. Yang, J. Wu, and T. J. Cui, "Design of digital coding metasurfaces with independent controls of phase and amplitude responses," *Applied Physics Letters*, vol. 113, no. 6, p. 063502, 2018.

[134] L. Zhang, X. Q. Chen, S. Liu, Q. Zhang, J. Zhao, J. Y. Dai, G. D. Bai, X. Wan, Q. Cheng, G. Castaldi *et al.*, "Space-time-coding digital metasurfaces," *Nature communications*, vol. 9, no. 1, pp. 1–11, 2018.

[135] X. Yi, X. Chen, L. Zhou, S. Hao, B. Zhang, and X. Duan, "A microwave power transmission experiment based on the near-field focused transmitter," *IEEE Antennas Wireless Propag. Lett.*, vol. 18, no. 6, pp. 1105–1108, 2019.

[136] H. Zhao, Y. Shuang, M. Wei, T. J. Cui, P. d. Hougne, and L. Li, "Metasurface-assisted massive backscatter wireless communication with commodity Wi-Fi signals," *Nature communications*, vol. 11, no. 1, pp. 1–10, 2020.

[137] Y. Yuan, K. Zhang, B. Ratni, Q. Song, X. Ding, Q. Wu, S. N. Burokur, and P. Genevet, "Independent phase modulation for quadruplex polarization channels enabled by chirality-assisted geometric-phase metasurfaces," *Nature communications*, vol. 11, no. 1, pp. 1–9, 2020.

[138] M. R. Ahsan, M. T. Islam, Y. Yamada, and N. Misran, "Ray tracing technique for shaping a dual reflector antenna system," *Turkish Journal of Electrical Engineering and Computer Sciences*, vol. 24, no. 3, pp. 1223–1234, 2016.

[139] G.-P. Gao, C. Yang, B. Hu, S.-F. Wang, and R.-F. Zhang, "Design of a high-gain and low-profile quasi-cassegrain antenna based on metasurfaces," *IEEE Antennas Wireless Propag. Lett.*, vol. 17, no. 8, pp. 1435–1439, 2018.

[140] E. M. F. Fernandes, M. W. B. da Silva, L. da Silva Briggs, A. L. P. de Siqueira Campos, H. X. de Araújo, I. R. S. Casella, C. E. Capovilla, V. P. R. M. Souza, and L. J. de Matos, "2.4–5.8 GHz dual-band patch antenna with FSS reflector for radiation parameters enhancement," *AEU-Int J Electron Commun*, vol. 108, pp. 235–241, 2019.

[141] E. Najafnezhad, J. Nourinia, C. Ghobadi, M. Majidzadeh, and F. Mirzamohammadi, "A high gain dual-band printed antenna for LTE base stations with a corner reflector," *AEU-Int J Electron Commun*, vol. 87, pp. 173–179, 2018.

[142] T. Yue, Z. H. Jiang, and D. H. Werner, "Compact, wideband antennas enabled by interdigitated capacitor-loaded metasurfaces," *IEEE Trans. Antennas Propag.*, vol. 64, no. 5, pp. 1595–1606, 2016.

[143] J. Luo, L. Li, J. Su, R. Ma, G. Han, and W. Zhang, "Multibeam antenna based on partially reflecting defected metasurface," *IEEE Antennas Wireless Propag. Lett.*, vol. 20, no. 8, pp. 1582–1586, 2021.

[144] J. Zhang, L. Han, X. Chen, R. Yang, and W. Zhang, "Multi-beam patch antenna based on metasurface," *IEEE Access*, vol. 8, pp. 37 281–37 286, 2019.

[145] P. Deo, A. Mehta, D. Mirshekar-Syahkal, P. J. Massey, and H. Nakano, "Thickness reduction and performance enhancement of steerable square loop antenna using hybrid high impedance surface," *IEEE Trans. Antennas Propag.*, vol. 58, no. 5, pp. 1477–1485, 2010.

[146] P. K. Jaiswal, R. Bhattacharya, and A. Kumar, "A UWB antipodal vivaldi antenna with high gain using metasurface and notches," *AEU-Int J Electron Commun*, vol. 159, p. 154473, 2023.

[147] J.-G. Lee and J.-H. Lee, "Low-profile dual-band superstrate antenna using metasurface," *Progress in Electromagnetics Research C*, vol. 77, pp. 175–184, 2017.

[148] J. Wang, Y. Cheng, H. Luo, F. Chen, and L. Wu, "High-gain bidirectional radiative circularly polarized antenna based on focusing metasurface," *AEU-Int J Electron Commun*, vol. 151, p. 154222, 2022.

[149] S. Chaimool, K. L. Chung, and P. Akkaraekthalin, "Simultaneous gain and bandwidths enhancement of a single-feed circularly polarized microstrip patch antenna using a metamaterial reflective surface," *Progress in Electromagnetics Research B*, vol. 22, pp. 23–37, 2010.

[150] A. O. Bah, P.-Y. Qin, R. W. Ziolkowski, Q. Cheng, and Y. J. Guo, "Realization of an ultra-thin metasurface to facilitate wide bandwidth, wide angle beam scanning," *Scientific Reports*, vol. 8, no. 1, p. 4761, 2018.

[151] S. Tang, X. Yang, Q. Liu, C. Liu, B. Hou, and X. Zhou, "Broadbanding of low-scattering coding metasurface by combining wave absorption and anti-phase cancellation mechanisms," *AEU-Int J Electron Commun*, vol. 136, p. 153782, 2021.

[152] Y. Li, C. Zou, M. Berecibar, E. Nanini-Maury, J. C.-W. Chan, P. Van den Bossche, J. Van Mierlo, and N. Omar, "Random forest regression for online capacity estimation of lithium-ion batteries," *Applied Energy*, vol. 232, pp. 197–210, 2018.

[153] V. Rodriguez-Galiano, M. Sanchez-Castillo, M. Chica-Olmo, and M. Chica-Rivas, "Machine learning predictive models for mineral prospectivity: An evaluation of neural networks, random forest, regression trees and support vector machines," *Ore Geology Reviews*, vol. 71, pp. 804–818, 2015.

[154] L. Breiman, "Random forests," *Springer Machine Learning*, vol. 45, pp. 5–32, 2001.

[155] A. Lahouar and J. B. H. Slama, "Hour-ahead wind power forecast based on random forests," *Elsevier Renewable Energy*, vol. 109, pp. 529–541, 2017.

[156] A. Karampatea and K. Siakavara, “Hybrid rectennas of printed dipole type on double negative dielectric media for powering sensors via RF ambient energy harvesting,” *AEU-Int J Electron Commun*, vol. 108, pp. 242–250, 2019.

[157] F. A. A. d. Souza, A. L. P. d. S. Campos, A. Gomes Neto, A. J. R. Serres, and C. C. R. d. Albuquerque, “Higher order mode attenuation in microstrip patch antenna with DGS H filter specification from 5 to 10 GHz range,” *Journal of Microwaves, Optoelectronics and Electromagnetic Applications*, vol. 19, pp. 214–227, 2020.